LBNL-59130

# EXPLORATORY SIMULATION STUDIES OF CAPROCK ALTERATION INDUCED BY STORAGE OF $CO_2$ IN DEPLETED GAS RESERVOIRS

*Fabrizio Gherardi[1], Tianfu Xu[2] and Karsten Pruess[2]*

[1] Istituto di Geoscienze e Georisorse (IGG) – CNR, Pisa, Italy
[2] Earth Sciences Division, Lawrence Berkeley National Laboratory, Berkeley, CA 94720

November 2005

This work was supported by the Director, Office of Science, Office of Basic Energy Sciences of the U.S. Department of Energy under Contract No. DE-AC02-05CH11231, and by the Consiglio Nazionale delle Ricerche, Italy, under the SnamProgetti SpA contract No. 3000005218, in the framework of the ENI SpA "GreenHouse Gases" R&D project. Support by Stogit and EniTecnologie is warmly acknowledged.

## Abstract

This report presents numerical simulations of isothermal reactive flows which might be induced in the caprock of an Italian depleted gas reservoir by the geological sequestration of carbon dioxide. Our objective is to verify that $CO_2$ geological disposal activities already planned for the study area are safe and do not induce any undesired environmental impact.

Gas-water-rock interactions have been modelled under two different intial conditions, i.e. assuming that i) caprock is perfectly sealed, or ii) partially fractured. Field conditions are better approximated in terms of the "sealed caprock model". The fractured caprock model has been implemented because it permits to explore the geochemical beahvior of the system under particularly severe conditions which are not currently encountered in the field, and then to delineate a sort of hypothetical maximum risk scenario.

Major evidences supporting the assumption of a sealed caprock stem from the fact that no gas leakages have been detected during the exploitation phase, subsequent reservoir repressurization due to the ingression of a lateral aquifer, and during several cycles of gas storage in the latest life of reservoir management.

An extensive program of multidisciplinary laboratory tests on rock properties, geochemical and microseismic monitoring, and reservoir simulation studies is underway to better characterize the reservoir and cap-rock behavior before the performance of a planned $CO_2$ sequestration pilot test.

In our models, fluid flow and mineral alteration are induced in the caprock by penetration of high $CO_2$ concentrations from the underlying reservoir, i.e. it was assumed that large amounts of $CO_2$ have been already injected at depth. The main focus is on the potential effect of these geochemical transformations on the sealing efficiency of caprock formations. Batch and multi-dimensional 1D and 2D modeling has been used to investigate multicomponent geochemical processes. Our simulations account for fracture-matrix interactions, gas phase participation in multiphase fluid flow and geochemical reactions, and kinetics of fluid-rock interactions.

The main objectives of the modeling are to recognize the geochemical processes or parameters to which the advancement of high $CO_2$ concentrations in the caprock is most sensitive, and to describe the most relevant mineralogical transformations occurring in the caprock as a consequence of such $CO_2$ storage in the underlying reservoir. We also examine the feedback of these geochemical processes on physical properties such as porosity, and evaluate how the sealing capacity of the caprock evolves in time.

## Table of Contents

## 1. Introduction

Geologic sequestration has been recently considered by the technical community as an effective means to reduce the increase of atmospheric $CO_2$ content. Modeling studies have suggested that under favorable conditions $CO_2$ is likely to be confined for very long times (see, among others, Bachu et al, 1994, Weir et al, 1996a, 1996b, Hitchon, 1996, White et al., 2005). Despite the great potential benefits of geologic sequestration, mainly related to the fact that the $CO_2$ injected in the subsurface can be isolated from the atmosphere for long time periods, risks may nevertheless be present. In particular, $CO_2$ can leak from storage reservoirs and return to the atmosphere. This is because additional geochemical processes may take place as a consequence of dissolution of supercritical $CO_2$ into deep brines, which may affect the integrity of the carbon repository (e.g. Gunter et al., 2000). Leakage is expected to occur through fractures, faults or, more generally, caprock weaknesses which may act as preferential ascent routes for deep-seated gases.

To gain a better understanding of the fluid flow and geochemical processes that would accompany $CO_2$ migration from a storage reservoir towards shallow depths, it is crucial to explore and evaluate impacts of dissolution processes of caprock formations by acidic $CO_2$-rich fluids (Gaus et al., 2005). This report is focused on the study of these reactive mechanisms.

The investigated area is a depleted gas reservoir in Italy, in which prefeasibility studies have already identified favorable conditions for $CO_2$ injection and underground storage. The reservoir consists of a multilayered sandstone formation located at depths generally below 1400 m b.g.l. (below ground level); simulations address the uppermost layer of this reservoir, where $CO_2$ injection is currently planned.

Site-specific data are available for basic physical parameters (temperature, pressure, porosity, permeability), chemical composition of reservoir aqueous solution, and caprock and reservoir mineralogy. The chemical composition of the caprock pore water is unknown, and has been calculated here by batch modeling (see below).

Gas-water-rock interactions resulting from $CO_2$ migration into the caprock have been simulated under dominance of two alternative mass transport conditions: molecular diffusion in the aqueous phase, and gas and/or liquid advection. All simulations concern the geological disposal of an almost pure-$CO_2$ waste stream. The effects induced by the underground disposal of less pure waste streams, as expected for coal-fired power plants where $SO_x$, $NO_x$, and $H_2S$ gas species are usually present along with $CO_2$ (Knauss et al., 2005), are not accounted for.

The simulations focus on $CO_2$-driven fluid-rock interactions in sealed and fractured caprock.
Fluid-rock interactions in sealed caprock have been modeled through a series of simplified 1D models, consisting of 20 to 50 m long vertical sections of 1 $m^2$ cross-sectional area through the caprock. Fluid-rock interactions in fractured caprock have been modeled through a series of simplified 2D models, which consider idealized fractured rocks with single or multiple vertical fracture zones of variable aperture and spacing.

Zero-dimensional, long-term (up to 10,000 years) batch simulations were carried out to assess the compatibility of different water compositions with respect to initial mineral assemblages, define chemical initial conditions and explore the geochemical evolutionary mechanisms expected under “static” conditions.
Multidimensional (1D and 2D) short-term (10 to 100 years) simulations with fine spatial discretization were used to investigate on a centimeter-scale the chemical processes likely to occur in the system when chemistry is coupled with fluid transport. The information obtained in this phase has then been used to define “maximum risk conditions” under which medium-term (100 to 1,000 years) simulations have been carried out with a less detailed spatial discretization.

The gas-water-rock interactions occurring in the caprock are modeled under different reservoir gas saturation initial conditions. Low-gas initial conditions (i.e. $S_{g,RESERVOIR}$ typically between to 0 to 0.5 in our simulations) are representative of conditions likely occurring in the peripheral zones of the field, where depressurization has favored the inflow of local groundwaters, and liquid phase has only been partially displaced by the gas plume. In this part of the field, the most relevant mineralogical changes occur in the liquid phase, at the interface between reservoir and caprock formations.

High-gas initial conditions ($S_{g,RESERVOIR}$ typically between 0.7 to 0.9) are representative of conditions expected near the injection wells and in the inner parts of the $CO_2$ plume. In this case, major geochemical transformations occur at the advancing gas front.

All calculations were performed with the TOUGHREACT code, a comprehensive, publicly available reactive transport simulator for multiphase systems (Xu et al., 2004). The numerical model was developed by introducing reactive chemistry into the framework of the existing multiphase and heat flow simulator TOUGH2 (Pruess, 1991, Pruess et al., 1999). Space discretization is obtained by means of an integral finite difference approach (Narashimhan and Witherspoon, 1976). Flow, transport, and geochemical reaction equations are solved separately by means of a sequential iteration approach similar to Yeh and Tripathi (1991). Full details on numerical methods are given in Xu and Pruess (1998) and Xu et al. (2001).

## 2. Modeling approach

The modeling has been built up in stages of increasing complexity. Starting from chemically, hydrologically and geometrically simplified systems, the sensitivity of system behavior has been explored with respect to parameters like grid geometry, initial mineralogy and chemical composition of formation waters. Simulations have been carried out for a range of conditions, with mass transport dominated by molecular diffusion or advection.

Variable time and space discretizations have been applied as a function of specific duration and detail of the simulations. Maximum simulation times vary from 10 to 1,000 years for 1D and 2D simulations, whereas the lower limit of the spatial resolution spans the range 0.001 to 0.1 m. Time stepping was done in accordance with numerical stability criteria dictated by the dominant mass transport process for the different simulations. The applied criteria are summarized below.

For diffusion-dominated transport, when the advection term could be neglected, the maximum time step has been set according to the following relationship (valid for the one-dimensional problem):

$$\Delta t \leq (\Delta x)^2 / 2 D,$$

where $\Delta t$ and $\Delta x$ are the time and the space discretization, and D is the effective diffusivity. In contrast, when the advection term dominates, the stability criterion is shown to be:

$$\Delta t \leq \Delta x / v,$$

where v is the effective velocity of phase (liquid or gas) considered.

Calculations have been carried out under the local equilibrium assumption for aqueous complexation, acid-base, redox and gas dissolution/exolution reactions. Aqueous activity coefficients are computed using an extended Debye-Hückel equation, according to Helgeson et al. (1981) and Tanger and Helgeson (1988).
Fugacity coefficients are computed for $H_2O(g)$ and $CO_2(g)$ species by means of the virial equation of Spycher and Reed (1988).

Precipitation and dissolution of minerals are kinetically-controlled. The kinetic laws incorporated in the code are derived from transition state theory (Lasaga, 1984). Effective reaction rates can be expressed through the following general equation:

$$\text{rate} = A_m k_m \{1 - (Q/K)^{\mu}\}^{\eta},$$

where $A_m$ is the specific surface area, $k_m$ is the kinetic rate constant, Q is the ion activity product, K the equilibrium constant for the specific mineral-water reaction, $\mu$ and $\eta$ two constants which depend on experimental data; they are usually but not always taken equal to 1.

Kinetic rates may depend on pH and also on concentrations of non-basis species. The temperature dependence of the reaction rate constant is expressed via an Arrhenius equation:

$$k_m = k_{25} \exp [-Ea / R (1/T – 1/298.15)]$$

where $E_a$ is the activation energy, $k_{25}$ is the rate constant at 25 deg-C, R is the gas constant, and T is absolute temperature.

Porosity changes due to volume changes related to mineral precipitation/dissolution processes are accounted for by use of the following relationship:

$$\phi = 1 – \Sigma_{(m=1,nm)} fr_m - fr_u,$$

where "nm" is the number of minerals, and "$fr_m$" and "$fr_u$" are the volume fraction of mineral "m" in the rock and the volume fraction of nonreactive rock, respectively.

In our simulations the permeability changes associated with changes in porosity are calculated from the following simplified cubic law:

$$k = k_i (\phi/\phi_i)^3,$$

where "$k_i$" and "$\phi_i$" are the initial permeability and porosity, respectively. Because of the complexity of natural geologic media, a generally valid porosity-permeability relationship is not realistically attainable (Raffensperger, 1996), and different formulations may be preferable in some cases (Xu et al., 2004b).

Diffusion occurs only in the liquid phase and relevant parameters are as follows: specific diffusion coefficient ($D_e$) is a constant for all aqueous species set to $10^{-9}$ $m^2$/sec, and tortuosity is calculated according to the Millington and Quirk (1961) equation:

$$\tau_0 \tau_\beta = \phi^{1/3} S_\beta^{10/3}$$

where $\tau_0 \tau_\beta$ is the tortuosity which includes a porous medium dependent factor $\tau_0$ and a coefficient that depends on phase saturation $S_\beta$, $\tau_\beta = \tau_\beta (S_\beta)$ (Pruess et al., 1999).

Both reservoir and caprock domains are modeled as porous media. In the following chapters, details on the different physical and geochemical initialization parameters used for these two rock domains are given.

## 3. Initial mineralogy

Reservoir formations mainly consist of sandstones with a significant component of carbonate (calcite and dolomite, about 16% by volume) and clay minerals (muscovite, chlorite, kaolinite, illite, Na-smectite, about 31% by volume). Bulk mass is represented by non-clay silicates like quartz, K-feldspar and a plagioclase here assumed of albitic composition (53% by volume on average).

The caprock is composed of carbonate-rich shales, made up of 33% by volume of calcite+dolomite and 47% by volume of silicate clay minerals, represented in order of decreasing abundance by muscovite, Na-smectite, chlorite, kaolinite and illite. Non-clay silicates are represented by quartz, which amounts to 20% by volume.

Sensitivity studies were carried out with respect to initial mineralogical compositions spanning the range shown in Table 1.

For the sake of simplicity, average compositions have been identified for both caprock and reservoir domains, and unless differently stated, these compositions have been considered in all the simulations presented in the

following chapters to simulate a “prototypical reference scenario” (hereinafter called PRS). These reference, average compositions are given in Table 2.

*Table 1 – Reservoir and caprock mineralogy compositional range (volume fraction of solid).*

| Reservoir Primary minerals | solid volume fraction | Caprock Primary minerals | solid volume fraction |
|---|---|---|---|
| Calcite | .12 ± .04 | Calcite | .30 ± .10 |
| Dolomite | .04 ± .02 | Dolomite | .03 ± .02 |
| Quartz | .35 ± .02 | Quartz | .20 ± .05 |
| Illite | .03 ± .01 | Illite | .03 ± .01 |
| K-feldspar | .05 ± .02 | K-feldspar | .00 |
| Chlorite | .09 ± .03 | Chlorite | .06 ± .02 |
| Albite-low | .15 ± .03 | Albite-low | .00 |
| Kaolinite | .02 ± .01 | Kaolinite | .04 ± .02 |
| Na-smectite | .01 ± .01 | Na-smectite | .15 ± .05 |
| Muscovite | .15 ± .05 | Muscovite | .20 ± .05 |

*Table 2 – List of reservoir and caprock mineralogical compositions used for the “reference average case” (volume fraction of solid, average values).*

| Reservoir Primary minerals | solid volume fraction | Caprock Primary minerals | solid volume fraction |
|---|---|---|---|
| Calcite | .12 | Calcite | .29 |
| Dolomite | .04 | Dolomite | .04 |
| Quartz | .34 | Quartz | .20 |
| Illite | .02 | Illite | .02 |
| K-feldspar | .05 | K-feldspar | .0 |
| Chlorite | .09 | Chlorite | .06 |
| Albite-low | .14 | Albite-low | .0 |
| Kaolinite | .03 | Kaolinite | .05 |
| Na-smectite | .01 | Na-smectite | .15 |
| Muscovite | .16 | Muscovite | .19 |

## 4. Initial aqueous solutions

Analytical data were available only for the aqueous solution of the reservoir. The available sample refers to a brackish water, of intermediate salinity between brines (up to 100 g/L Cl-) generally occurring at depth within the system and dilute, superficial waters (few ppm Cl-), possibly entering the reservoir in marginal and more heavily depressurized areas. This water has been assumed to be representative of the fluids present in the shallowest layer of the reservoir, located immediately below the caprock. Full details on chemical composition are reported in Table 3. This reference chemical analysis has always been utilized in the model to initialize the aqueous composition in the reservoir domain.

No analytical data exists for the caprock pore waters. The initial aqueous solution for the caprock has been generated through an iterative batch modeling procedure, starting from data on mineralogy and fixing total salinity at similar values as the underlying reservoir waters (about 1.5m NaCl). More details are given in the following chapters.

*Table 3 – Chemical analysis of reservoir water (concentrations are in mol/kg H2O)*

| reservoir | | |
|---|---|---|
| T=23°C | | |
| pH=5.90 | | |
| Component | free species | Ctot |
| Ca+2 | 1.0000e-01 | 1.0916e-01 |
| Mg+2 | 1.0000e-01 | 1.0286e-01 |
| Na+ | 1.0000e+00 | 1.1541e+00 |
| K+ | 1.1000e-01 | 1.1085e-01 |
| Fe+2 | 2.0000e-05 | 2.3279e-05 |
| SiO2(aq) | 2.8000e-04 | 2.9226e-04 |
| AlO2- | 0.9000e-08 | 1.0000e-08 |
| Cl- | 1.7000e+00 | 1.7198e+00 |
| HCO3- | 2.6714e-03 | 2.8916e-03 |
| SO4-2 | 1.1000e-04 | 1.1452e-04 |
| Li+ | 2.0170e-04 | 2.0170e-04 |
| I- | 2.4428e-04 | 2.4428e-04 |
| Ba+2 | 8.0829e-04 | 8.0829e-04 |
| Br- | 3.0036e-03 | 3.0036e-03 |
| Sr+2 | 3.6065e-03 | 3.6065e-03 |
| Mn+2 | 6.6620e-05 | 6.6620e-05 |
| NH4+ | 5.1002e-03 | 5.1002e-03 |

## 5. Thermodynamic and kinetic parameters

The mineralogy of the system is described in terms of 10 primary minerals, and 12 secondary minerals, as shown in Tables 1, 2, and 4. The selected initial mineralogy reflects some conceptualization of the observed assemblage. This conceptualization is needed because the description of minerals is not always sufficiently specific to resolve the contribution of undifferentiated minerals like micas and clay minerals.

For example, in our database chlorite group minerals are represented by means of a single mineral which is marked “chlorite” ($Mg_{2.5}Fe_{2.5}Al_2Si_3O_{10}(OH)_8$), and is intermediate in chemical composition with respect to Mg- and Fe-enriched end-members daphnite-14Å ($Fe_5Al_2Si_3O_{10}(OH)_8$) and clinochlore-14Å ($Mg_5Al_2Si_3O_{10}(OH)_8$). Illite group minerals are represented by a single mineral (“illite”), characterized by the following chemical formula $K_{0.6}Mg_{0.25}Al_{1.8}(Al_{0.5}Si_{3.5}O_{10})(OH)_2$. Na- and Ca-smectite are assumed to have the following chemical formulas: $Na_{0.29}Mg_{0.26}Al_{1.77}Si_{3.97}O_{10}(OH)_2$ and $Ca_{0.145}Mg_{0.26}Al_{1.77}Si_{3.97}O_{10}(OH)_2$, whereas unspecified plagioclase is assumed to consist of albite only. The existence of possible solid solutions has not been taken into account.

Thermodynamic data for minerals, gases and aqueous species are mostly taken from the EQ3/6 V7.2b database of Wolery (1992). Some substitutions and changes have been incorporated to account for recent published revisions in thermodynamic properties of rock forming minerals and aqueous species. Details on data sources and the list of chemical species for which thermodynamic parameters have been updated, are given in Xu et al (2005).

Some of the most relevant kinetic parameters are summarized in Table 4. They are taken from Xu et al. (2004), Xu et al. (2005), Palandri and Kharaka (2004), and references cited therein. Reactive surface area for each mineral is calculated from the specific reactive area and the quantity of each mineral, assuming that the reactive surface is proportional to specific surface. Due to the large natural variability and uncertainty in the measurement of specific reactive areas of minerals, no sensitivity analysis has been performed with respect to this parameter. Initial values have been set according to literature data, in order to account for the larger intrinsic surface areas of clay minerals with respect to other minerals.

Sensitivity analysis has shown that the use of different kinetic rate laws and activation energies taken from the cited references has no appreciable effect on numerical results of the simulations. For this reason, this aspect will not be further discussed in the present report.

*Table 4 – Summary of minerals taken into consideration during the simulation and their kinetic constants, activation energies and specific reactive areas.*

| Primary mineral | $k_n$,25 (mol/m^2/sec) | Ea (kJ/mol) | specific reactive area (cm^2/gr) |
|---|---|---|---|
| Calcite | 1.6e-06 | 23.50 | 100.0e-1 |
| Dolomite | 3.0e-13 | 52.20 | 100.0e-1 |
| Quartz | 1.0e-14 | 87.70 | 100.0e-1 |
| Illite | 1.7e-13 | 35.00 | 1520.0e-1 |
| K-feldspar | 3.9e-13 | 38.00 | 100.0e-1 |
| Chlorite | 3.0e-13 | 88.00 | 200.0e-1 |
| Albite-low | 2.8e-13 | 69.80 | 100.0e-1 |
| Kaolinite | 6.9e-14 | 22.20 | 230.0e-1 |
| Na-smectite | 1.7e-13 | 35.00 | 1520.0e-1 |
| Muscovite | 3.0e-13 | 88.00 | 1520.0e-1 |
| **Secondary mineral** | **$k_n$,25 (mol*m^2/sec)** | **Ea (kJ/mol)** | **specific reactive area (cm^2/gr)** |
| Pyrite | 4.0e-11 | 62.76 | 130.0e-1 |
| Ankerite | 1.3e-09 | 62.80 | 100.0e-1 |
| Oligoclase | 1.4e-12 | 69.80 | 100.0e-1 |
| Hematite | 2.5e-15 | 66.20 | 130.0e-1 |
| Magnetite | 1.7e-11 | 18.60 | 130.0e-1 |
| Magnesite | 4.6e-10 | 23.50 | 100.0e-1 |
| Siderite | 1.3e-09 | 62.80 | 100.0e-1 |
| Dawsonite | 1.3e-09 | 62.80 | 100.0e-1 |
| Ca-smectite | 1.7e-13 | 35.00 | 1520.0e-1 |
| Anhydrite | 6.5e-04 | 14.30 | 100.0e-1 |
| Halite | 6.2e-01 | 7.40 | 100.0e-1 |
| Anorthite | 7.6e-10 | 17.80 | 100.0e-1 |

## 6. Initial physical parameters

Simulations were carried out for isothermal conditions of 45 deg-C, and 105 bar total pressure, which corresponds to the values currently measured at the top of the reservoir. Physical data utilized in the simulations are summarized in Table 5. Due to the lack of reliable data for the caprock domain, capillary pressure and relative permeability parameters, and functional dependences on pressure and phase saturations have been taken from the literature (Pruess et al, 1999; Xu et al, 2004). In particular, capillary pressure behavior is described through the Van Genutchen (1980) relationship, which likely overestimate gas-phase transfer from reservoir to caprock. This is because the Van Genutchen function does not provide any “gas entry-pressure” value, which implies that gas-phase migrates into the caprock only when the pressure gradient established between the reservoir and the caprock overcomes the gas entry pressure.
In contrast, permeability, porosity and grain density have been set to average values reasonably representative of the system under study. Sensitivity analysis were performed with respect to caprock initial porosity (between 0.05 to 0.15) and permeability (0.01e-15 to 0.1e-15 $m^2$).

*Table 5 - Initial values for selected physical parameters*

| Rock domain | rock grain density ($kg/m^3$) | porosity | abs.permeability (isotropic, $m^2$) |
|---|---|---|---|
| Reservoir | 2720. | .325 | 400.e-15 |
| Caprock | 2830. | .150 | 0.1e-15 |

| Capillary pressure function from Van Genuchten (1980) | | | | | |
|---|---|---|---|---|---|
| Rock domain | lambda | $S_{lr}$ | $S_{ls}$ | Pmax | $1/P_0$ |
| Reservoir | .457 | .00 | .999 | 1.e7 | 5.1e-5 |

| | | | | | |
|---|---|---|---|---|---|
| Caprock | .457 | .00 | .999 | 1.e8 | 1.6e-7 |

Liquid relative permeability function from Van Genutchen (1980)

| Rock domain | lambda | $S_{lr}$ | $S_{ls}$ | $S_{gr}$ |
|---|---|---|---|---|
| Reservoir | .457 | .30 | 1.0 | .05 |
| Caprock | .457 | .30 | 1.0 | .05 |

## 7. Results

## 7.1. Zero-dimensional batch simulations

### 7.1.1. Reservoir

In order to evaluate the geochemical effects induced by the presence of a high-pressure $CO_2$ gas phase in the reservoir, several different runs were carried out for different initial gas saturations. The idea was to estimate on a representative volume of the geochemical system the effects of variably $P_{CO2}$ up to very high values likely encountered in geological $CO_2$ sequestration scenarios. Three of these simulations are discussed in some detail below, for the following initial conditions:

**i)** $S_L = 1.0$; $P_{CO2}$ at background levels (aqueous solution as specified in Table 3), according to thermodynamic relationships governing the equilibria within the carbonate system; T = 45°C; $P_{TOT} = 105$ bar;

**ii)** $S_L = 0.7$; $P_{CO2} \approx P_{TOT} = 105$ bar; T = 45°C;

**iii)** $S_L = 0.1$; $P_{CO2} \approx P_{TOT} = 105$ bar; T = 45°C.

In all cases the simulations were performed for a time period of 10,000 years.

**Case i)** The geochemical evolution of an initially fully liquid saturated reservoir ($S_L = 1$) is characterized by the tendency of albite, illite and calcite to dissolve, and of Na-smectite, K-feldspar, dolomite and muscovite to precipitate. These changes in mineralogy do not lead to significant changes in porosity, which only slightly decreases from the initial value of 32.5% to the final value of 32.45% over 10,000 years of simulation time (Figure 1). No secondary minerals precipitate. The changes in volume fraction of primary minerals are summarized below in Table 6.

*Table 6 – Mineral abundances at the beginning and at the end of reservoir $S_L$=1 run*

| mineral | abundance (solid volume fraction) | | |
|---|---|---|---|
| | *initial* | *end of run* | *difference* |
| *calcite* | 0.115 | 0.113 | -0.0024 |
| *dolomite* | 0.043 | 0.046 | 0.0029 |
| *quartz* | 0.344 | 0.344 | -0.0004 |
| *illite* | 0.015 | 0.005 | -0.0095 |
| *k-feldspar* | 0.053 | 0.061 | 0.0081 |
| *chlorite* | 0.095 | 0.095 | -0.0001 |
| *albite-low* | 0.140 | 0.127 | -0.013 |
| *kaolinite* | 0.026 | 0.026 | -0.0003 |
| *smectite-na* | 0.010 | 0.022 | 0.012 |
| *muscovite* | 0.159 | 0.161 | 0.0026 |

Primary minerals show different behavior in time. Calcite is characterized by a complex pattern, with an initial sharp reduction in volume fraction, followed by a slight increase (Figure 1). Dolomite, instead, is characterized by an initial relatively sharp increase in volume fraction, followed by a plateau (Figure 1).

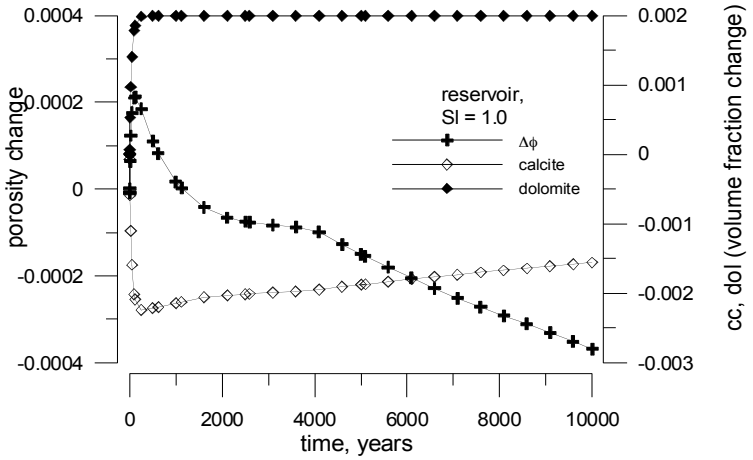


*Figure 1 – Change of calcite and dolomite abundance (in volume fraction total medium) vs. time for reservoir batch simulation at $S_L$=1.0. The porosity change pattern is also shown.*

The patterns of other relevant minerals, K-feldspar, Na-smectite, albite, quartz, muscovite, kaolinite, and illite are shown in Figures 2 and 3, respectively. Most of these minerals are characterized by almost continuous trends with time, which indicate that the system is not completely equilibrated at the end of the run. However, the smoothness of the observed patterns and the small variations reported in Table 6 indicate the attainment of conditions that are reasonably close to steady state.

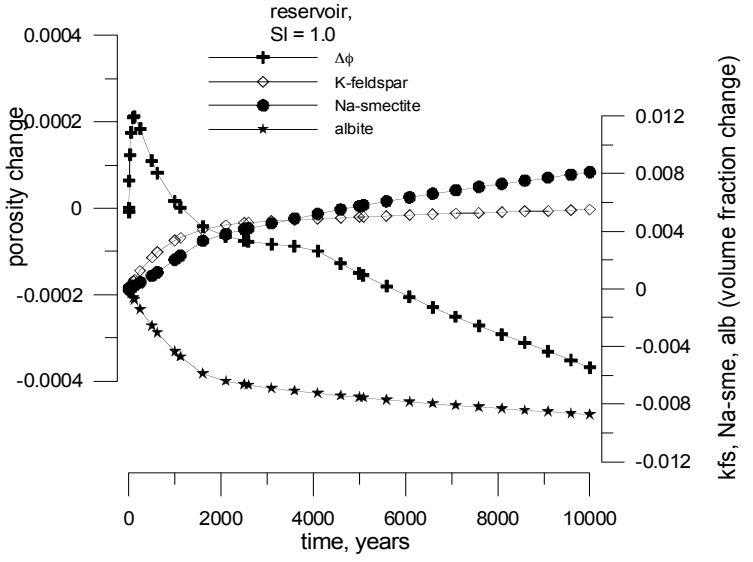


*Figure 2 – Change of K-feldspar, Na-smectite and albite abundance (in volume fraction total medium) vs. time for reservoir batch simulation at $S_L$=1.0. The porosity change pattern is also shown.*

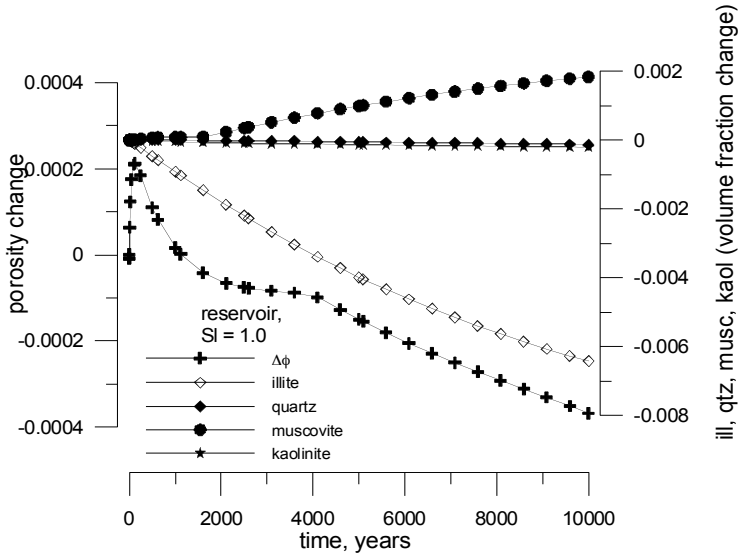


*Figure 3 – Change of illite, quartz, muscovite and kaolinite abundance (in volume fraction total medium) vs. time for reservoir batch simulation at $S_L$=1.0. The porosity change pattern is also shown.*

The chemical composition of the associated aqueous solution is characterized by the achievement of quasi-steady conditions after about 3-4000 years for most of the basis species involved (see Figures 4, 5 and 6). Details on final concentrations are as follows: $H^+$ (pH = 7.3), $Ca^{+2}$ (1.5e-1 mol/kg $H_2O$), $Na^+$ (1.2 mol/kg $H_2O$), $Cl^-$ (1.54 mol/kg $H_2O$), $HCO_3$ (1.1e-4 mol/kg $H_2O$), $SiO_2$,aq (2.e-4 mol/kg $H_2O$), $K^+$ (1.6 e-3 mol/kg $H_2O$) and $AlO_2^-$ (1.7e-8 mol/kg $H_2O$).

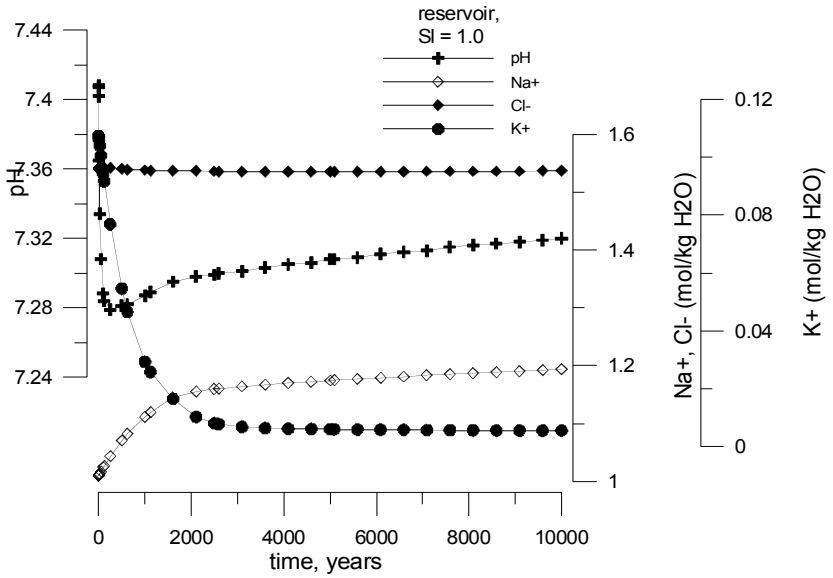


*Figure 4 – Change of $Na^+$, $Cl^-$ and $K^+$ aqueous concentration (mol/kg H2O) vs. time for reservoir batch simulation at $S_L$=1.0. The pH pattern is also shown.*

$Mg^{+2}$ component (Figure 5) shows the more significant variations (5.8e-6 mol/kg $H_2O$ after 10,000 years), and an overall prolonged tendency to decrease in concentration, likely due to progressive precipitation of Na-smectite, which fixes some of the $Mg^{+2}$ initially present in the aqueous solution. Finally, $SO_4^{-2}$ concentrations (Figure 6) tend to decrease at the end of the run after a prolonged plateau at 4.e-5 mol/kg $H_2O$, reflecting the concomitant precipitation of some pyrite and the decrease in redox potential.

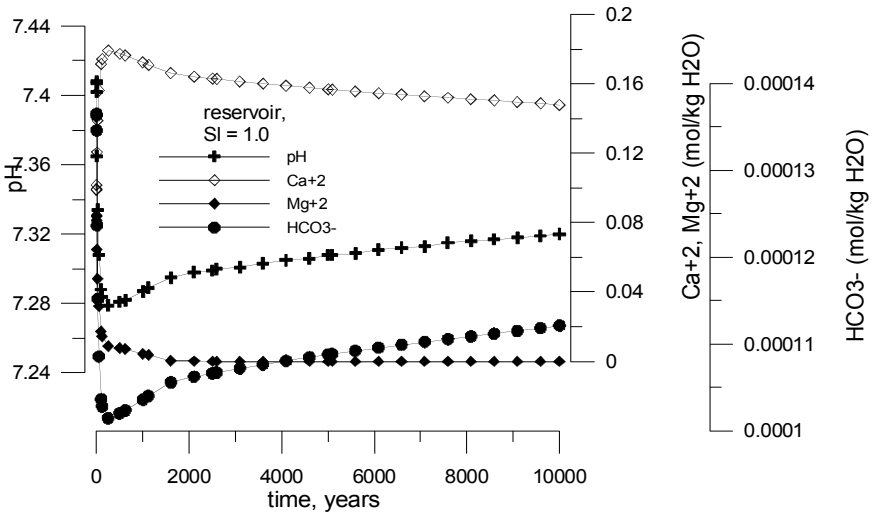


*Figure 5 – Change of $Ca^{+2}$, $Mg^{+2}$ and $HCO_3^-$ aqueous concentration (mol/kg H2O) vs. time for reservoir batch simulation at $S_L$=1.0. The pH pattern is also shown.*

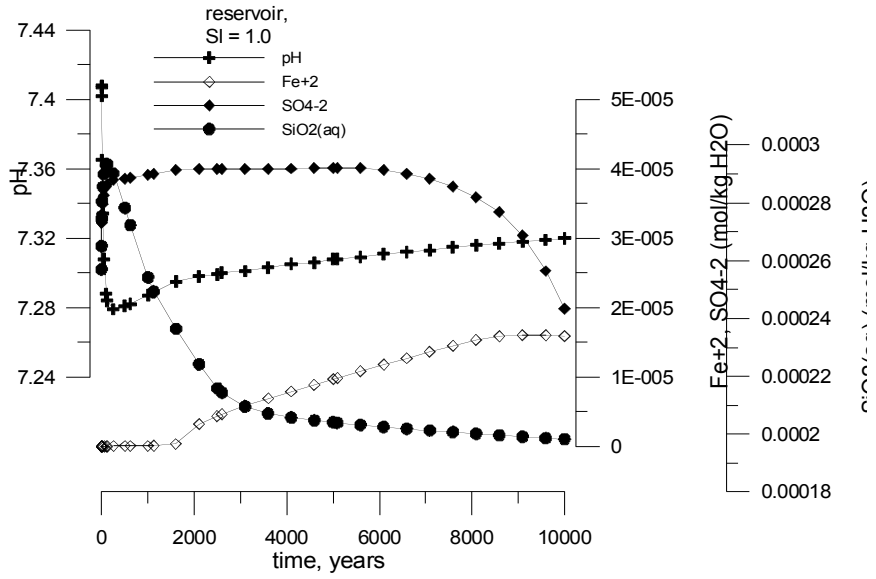


*Figure 6 – Change of $Fe^{+2}$, $SO_4^{-2}$ and $SiO_2$(aq) aqueous concentration (mol/kg H2O) vs. time for reservoir batch simulation at $S_L$=1.0. The pH pattern is also shown.*

**Case ii)** The presence of a $CO_2$-rich gas phase ($P_{CO2}$ = 105 bar) induces significant changes in the geochemical conditions of the reservoir, due to the lowering of pH to a value of about 4.7, well below the value of about 7.3 that is typical of $S_L$ = 1.0 and low-$P_{CO2}$ conditions (see Figure 7). In Figure 7 the pH pattern for simulations carried out under different initial gas saturations are also shown. The comparison between the different curves suggests that at higher gas saturations the overall reactivity of the system tends to decrease, so that pH is stabilized at near the same values (about 4.7) after longer times and following slightly different patterns.

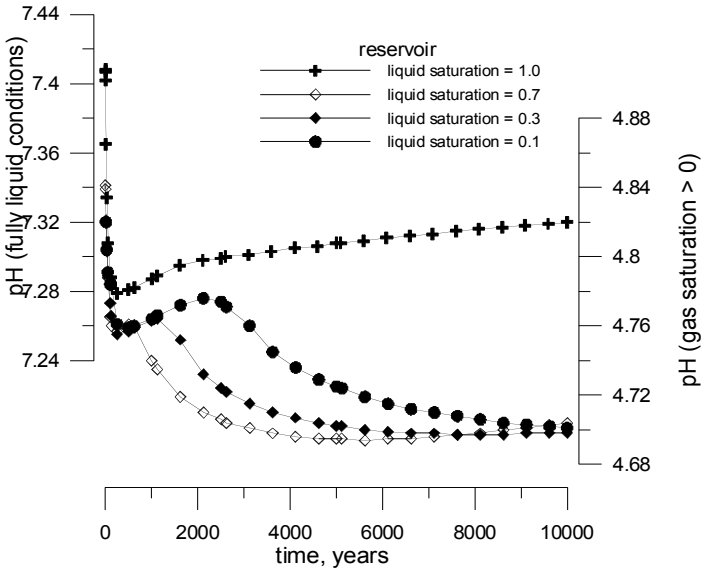


*Figure 7 – pH evolution vs. time in the reservoir under different initial liquid saturation conditions.*

One of the most important features of the $S_L$ = 0.7 run is the reversal of some mineral patterns with respect to those previously described in single-phase liquid conditions (Figs. 8-10).
In particular, muscovite now dissolves, whereas quartz and kaolinite tend to precipitate. Other trends are induced by the acidity produced within the reservoir, leading to more effective precipitation of dolomite, K-feldspar and Na-smectite, and dissolution of chlorite, illite and albite. Enhanced acidity also affects the behavior of calcite, which now clearly dissolves.
New minerals also appear, mainly represented by carbonate phases such as siderite (Fig. 9) and ankerite, that incorporate in their structure bivalent cations ($Fe^{+2}$, $Mg^{+2}$) made available to the aqueous solution through chlorite and illite dissolution. In addition we obtain carbonate-silicate minerals like dawsonite (see Figure 9), which probably also benefits from dissolution of muscovite.

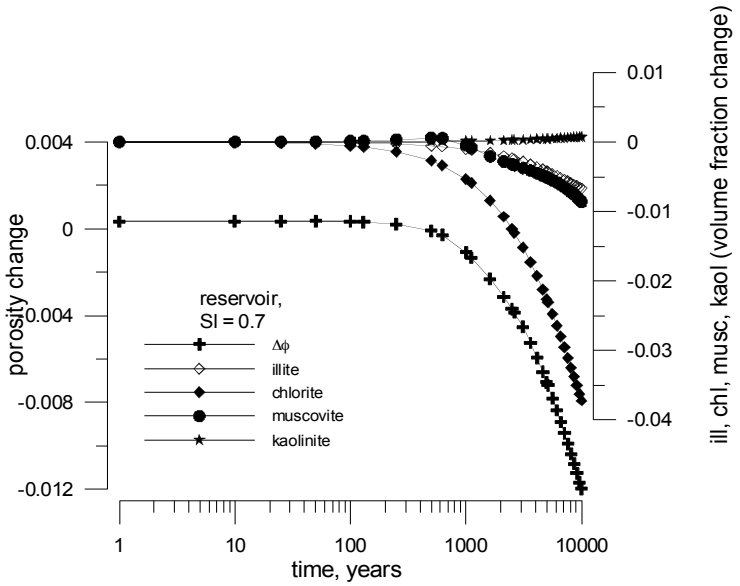


*Figure 8 – Change of illite, chlorite, muscovite, kaolinite and quartz abundance (in volume fraction total medium) vs. time for reservoir batch simulation at $S_L$=0.7*

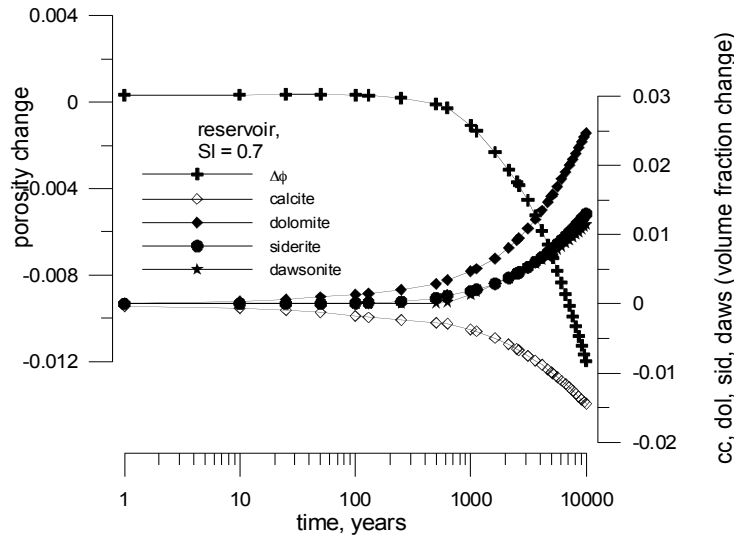


*Figure 9 – Change of calcite, dolomite, siderite and dawsonite abundance (in volume fraction total medium) vs. time for reservoir batch simulation at $S_L$=0.7*

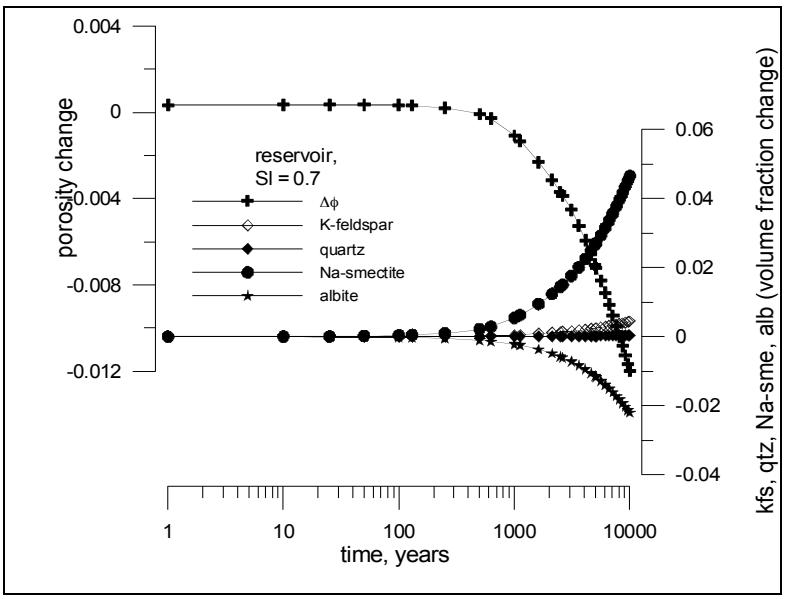


*Figure 10 – Change of K-feldspar, quartz, Na-smectite and albite abundance (in volume fraction total medium) vs. time for reservoir batch simulation at $S_L$=0.7*

The variations in porosity are now more significant, with an overall decrease of about 1.2% at the end of the run (from 32.5% to 31.3%). Detailed results for the volume fraction variations of minerals are given in Table 7.

*Table 7 – Inventory of mineral abundances at the beginning and at the end of reservoir $S_L$=0.7 run*

| mineral | abundance (solid volume fraction) | | |
|---|---|---|---|
| | *initial* | *end of run* | *difference* |
| *Calcite* | 0.115 | 0.092 | -0.0231 |
| *Dolomite* | 0.043 | 0.078 | 0.0352 |
| *Quartz* | 0.344 | 0.339 | -0.0055 |
| *Illite* | 0.015 | 0.005 | -0.010 |
| *K-feldspar* | 0.053 | 0.059 | 0.0056 |
| *Chlorite* | 0.095 | 0.039 | -0.0558 |
| *Albite-low* | 0.140 | 0.106 | -0.0346 |
| *Kaolinite* | 0.026 | 0.027 | 0.0006 |
| *Na-smectite* | 0.010 | 0.077 | 0.0675 |
| *Muscovite* | 0.159 | 0.143 | -0.0153 |
| *Siderite* | 0 | 0.019 | 0.0189 |
| *Dawsonite* | 0 | 0.017 | 0.0166 |

The chemical composition of the aqueous solution appears well stabilized after 2,000 years, but changes were quite limited also during the initial transient phase. A summary of the final aqueous compositions for the "$S_L$ = 1.0" and "$S_L$ = 0.7" runs is provided in Table 8.

*Table 8 – Chemical composition of aqueous solutions (mol/kg $H_2O$) after 10,000 years*

Final aqueous composition – run $S_L$=1.0

T=45°C
pH=7.32

| Component | free species | Ctot |
|---|---|---|
| Ca+2 | 0.1479e+00 | 0.1621e+00 |
| Mg+2 | 0.5779e-05 | 0.7064e-05 |
| Na+ | 0.1194e+01 | 0.1361e+01 |
| K+ | 0.5516e-02 | 0.5693e-02 |
| Fe+2 | 0.1588e-04 | 0.1976e-04 |
| SiO2(aq) | 0.1983e-03 | 0.2214e-03 |
| AlO2- | 0.1842e-07 | 0.2163e-07 |
| Cl- | 0.1536e+01 | 0.1724e+01 |
| HCO3- | 0.1121e-03 | 0.2163e-03 |
| SO4-2 | 0.1979e-04 | 0.5639e-04 |
| O2(aq) | 0.2012e-66 | -0.1217e-07 |
| Li+ | 0.2022e-03 | 0.2022e-03 |
| I- | 0.2449e-03 | 0.2449e-03 |
| Ba+2 | 0.8102e-03 | 0.8102e-03 |
| Br- | 0.3011e-02 | 0.3011e-02 |
| Sr+2 | 0.3615e-02 | 0.3615e-02 |
| Mn+2 | 0.6678e-04 | 0.6678e-04 |
| NH4+ | 0.5112e-02 | 0.5112e-02 |

Final aqueous composition – run $S_L$=0.7

T=45°C
pH=4.70

| Component | free species | Ctot |
|---|---|---|
| Ca+2 | 0.2334e+00 | 0.2708e+00 |
| Mg+2 | 0.1601e-01 | 0.2083e-01 |
| Na+ | 0.7393e+00 | 0.8590e+00 |
| K+ | 0.3140e+00 | 0.3245e+00 |
| Fe+2 | 0.1595e-02 | 0.2565e-02 |
| SiO2(aq) | 0.5655e-03 | 0.5657e-03 |
| AlO2- | 0.2969e-10 | 0.1969e-06 |
| Cl- | 0.1592e+01 | 0.1751e+01 |
| HCO3- | 0.2945e-01 | 0.5835e+00 |
| SO4-2 | 0.3676e-04 | 0.1166e-03 |
| O2(aq) | 0.1142e-60 | 0.1767e-16 |
| Li+ | 0.2053e-03 | 0.2053e-03 |
| I- | 0.2486e-03 | 0.2486e-03 |
| Ba+2 | 0.8227e-03 | 0.8227e-03 |
| Br- | 0.3057e-02 | 0.3057e-02 |
| Sr+2 | 0.3671e-02 | 0.3671e-02 |
| Mn+2 | 0.6781e-04 | 0.6781e-04 |
| NH4+ | 0.5191e-02 | 0.5191e-02 |

**Case iii)** As expected, a further increase in gas saturation to $S_g$ = 0.9 (corresponding to $S_L$ = 0.1) reduces the reactivity of the system in comparison to the $S_g$ = 0.3 case. The same mineralogical transformations described for the **case ii)** are observed also in this simulation (Figures 11, 12 and 13), but in this case the observed geochemical patterns are milder then before, and the overall change in mineralogical composition observed at the end of the run is less significant than in $S_L$ = 0.7 conditions. In particular, porosity decreases by only about 0.2% after 10 kyrs. A summary of volume fraction variations is given in Table 9 for the most relevant minerals.

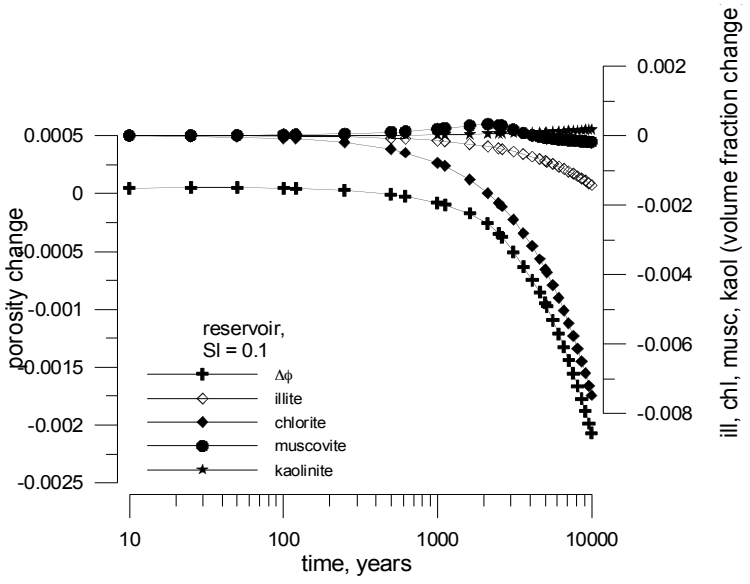


*Figure 11 – Change of illite, chlorite, muscovite, kaolinite and quartz abundance (in volume fraction total medium) vs. time for reservoir batch simulation at $S_L$=0.1.*

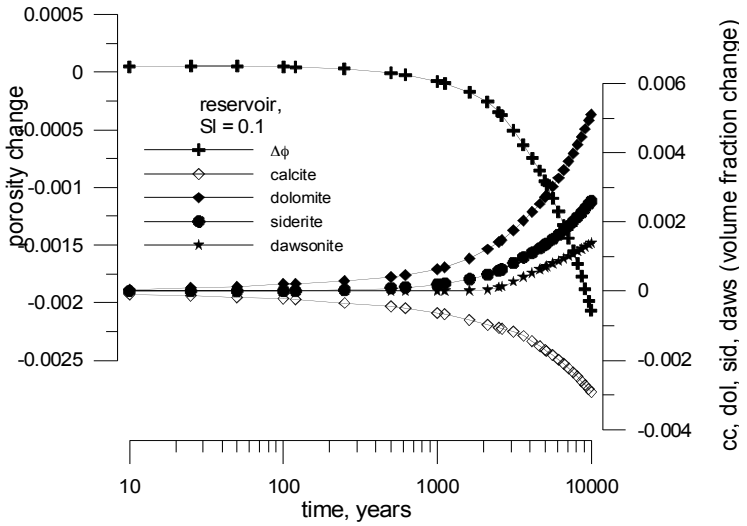


*Figure 12 – Change of calcite, dolomite, siderite and dawsonite abundance (in volume fraction total medium) vs. time for reservoir batch simulation at $S_L$=0.1.*

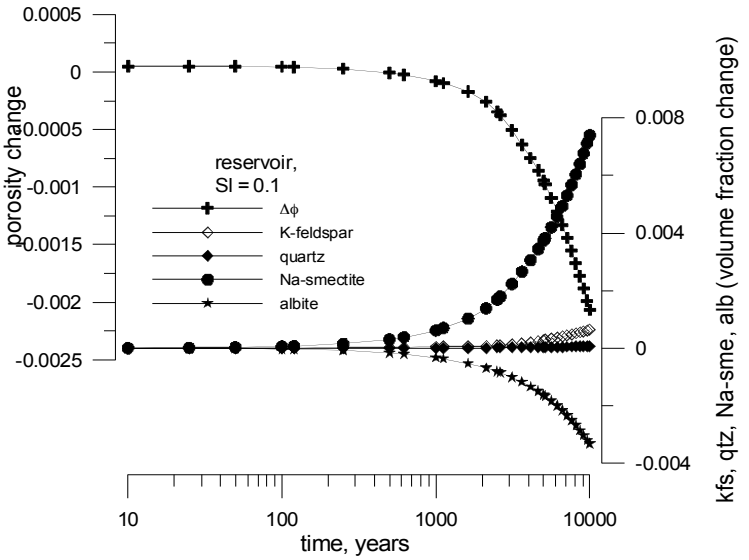


*Figure 13 – Change of K-feldspar, quartz, Na-smectite and albite abundance (in volume fraction total medium) vs. time for reservoir batch simulation at $S_L$=0.1.*

*Table 9 – Inventory of mineral abundances at the beginning and at the end of reservoir $S_L$=0.1 run*

| mineral | abundance (solid volume fraction) | | |
|---|---|---|---|
| | *initial* | *end of run* | *difference* |
| *Calcite* | 0.115 | 0.111 | -0.0047 |
| *Dolomite* | 0.043 | 0.050 | 0.0074 |
| *Quartz* | 0.344 | 0.343 | -0.0010 |
| *Illite* | 0.015 | 0.013 | -0.0021 |
| *K-feldspar* | 0.053 | 0.054 | 0.0008 |
| *Chlorite* | 0.095 | 0.083 | -0.0113 |
| *Albite-low* | 0.140 | 0.135 | -0.0053 |
| *Kaolinite* | 0.026 | 0.026 | 0.0002 |
| *Na-smectite* | 0.010 | 0.021 | 0.0109 |
| *Muscovite* | 0.159 | 0.158 | -0.0008 |
| *Siderite* | 0 | 0.004 | 0.0039 |
| *Dawsonite* | 0 | 0.002 | 0.0021 |

## 7.1.2. Caprock

For the caprock several batch simulations were carried out in order to "reconstruct" a synthetic chemical composition reasonably representative of the unknown water composition likely present in the caprock.

The suite of primary and secondary minerals, temperature (45°C) and pressure (105 bar) were the same as in the case of reservoir batch simulations.

Different initial trial solutions were utilized in order to obtain a reasonably stable water composition consistent with the local geochemical setting, i.e. an aqueous solution nearly saturated with respect to relevant primary caprock minerals, having roughly the same NaCl salinity as the adjacent reservoir. The search for such a "best fitting water" has been carried out iteratively, following a trial and error procedure.

Full details on the chemistry of the final water obtained are given in Table 10, together with saturation indices of mineral components.

*Table 10 – Caprock aqueous concentrations (mol/kg H2O) and saturation index values of minerals*

Caprock water

Temp=45°C
pH=7.48

| Component | free species | Ctot |
|---|---|---|
| Ca+2 | 0.6923e-01 | 0.7583e-01 |
| Mg+2 | 0.2017e-01 | 0.2458e-01 |
| Na+ | 0.1053e+01 | 0.1197e+01 |
| K+ | 0.4976e-01 | 0.5133e-01 |
| Fe+2 | 0.2471e-08 | 0.3066e-08 |
| SiO2(aq) | 0.1197e-03 | 0.1377e-03 |
| AlO2- | 0.1917e-07 | 0.2189e-07 |
| Cl- | 0.1540e+01 | 0.1700e+01 |
| HCO3- | 0.1651e-03 | 0.3631e-03 |
| SO4-2 | 0.5147e-11 | 0.9988e-06 |
| O2(aq) | 0.6841e-71 | -0.1585e-03 |
| Li+ | 0.9998e-06 | 0.9998e-06 |
| I- | 0.9998e-06 | 0.9998e-06 |

```
Ba+2            0.9998e-06    0.9998e-06
Br-             0.9998e-06    0.9998e-06
Sr+2            0.9998e-06    0.9998e-06
Mn+2            0.9998e-06    0.9998e-06
NH4+            0.9998e-06    0.9998e-06
```

| Primary minerals | log(Q/K) |
|---|---|
| Calcite | 0.000 |
| Dolomite | 0.779 |
| Quartz | -0.413 |
| Illite | -1.317 |
| Chlorite | 0.000 |
| Kaolinite | -0.873 |
| Na-smectite | 0.045 |

| Secondary minerals | log(Q/K) |
|---|---|
| K-feldspar | 0.399 |
| Pyrite | -1.488 |
| Albite-low | -0.712 |
| Ankerite | -3.644 |
| Oligoclase | -12.366 |
| Hematite | -8.256 |
| Magnetite | -12.102 |
| Magnesite | -0.738 |
| Siderite | -5.291 |
| Dawsonite | -2.091 |
| Ca-smectite | -0.139 |
| Anhydrite | -9.521 |
| Muscovite | 0.004 |
| Halite | -1.744 |
| Anorthite | -6.954 |

In order to check the thermodynamic and kinetic stability of the system formed by this water and the initial caprock mineralogy, another simulation has been carried out by allowing them to react together for 1,000 years. As seen from the results presented in Tables 11 and 12, the caprock system is approximately at a stationary-state, as both volumetric abundances of minerals and chemical concentrations of aqueous components remain almost constant with time.

*Table 11 – Inventory of mineral abundances of caprock at the beginning and after 1,000 years of simulation*

| mineral | abundance (solid volume fraction) | | |
|---|---|---|---|
| | *initial* | *end of run* | *difference* |
| *Calcite* | 0.285 | 0.285 | -0.0002 |
| *Dolomite* | 0.037 | 0.037 | 0.0002 |
| *Quartz* | 0.205 | 0.205 | 0 |
| *Illite* | 0.020 | 0.020 | -0.0001 |
| *K-feldspar* | 0 | 0 | 0 |
| *Chlorite* | 0.062 | 0.062 | 0 |
| *Kaolinite* | 0.051 | 0.051 | 0 |
| *Na-smectite* | 0.151 | 0.151 | 0.0001 |
| *Muscovite* | 0.190 | 0.190 | 0.0001 |

*Table 12 – Water chemistry (mol/kg $H_2O$) at the beginning and after 1,000 years of simulation*

Caprock water – initial guess composition

Temp=45°C
pH=7.57

| Component | free species | Ctot |
|---|---|---|
| Ca+2 | 0.4575e-01 | 0.5011e-01 |
| Mg+2 | 0.4105e-01 | 0.5000e-01 |
| Na+ | 0.1055e+01 | 0.1200e+01 |
| K+ | 0.4848e-01 | 0.5000e-01 |
| Fe+2 | 0.6286e-09 | 0.7802e-09 |
| SiO2(aq) | 0.8641e-04 | 0.1025e-03 |
| AlO2- | 0.3114e-07 | 0.3540e-07 |
| Cl- | 0.1539e+01 | 0.1700e+01 |
| HCO3- | 0.2031e-03 | 0.4283e+03 |
| SO4-2 | 0.6438e-11 | 0.1000e+05 |
| O2(aq) | 0.6845e-71 | -0.1586e-03 |
| Li+ | 0.1000e-05 | 0.1000e-05 |
| I- | 0.1000e-05 | 0.1000e-05 |
| Ba+2 | 0.1000e-05 | 0.1000e-05 |
| Br- | 0.1000e-05 | 0.1000e-05 |
| Sr+2 | 0.1000e-05 | 0.1000e-05 |
| Mn+2 | 0.1000e-05 | 0.1000e-05 |
| NH4+ | 0.1000e-05 | 0.1000e-05 |

Caprock water –composition after 1000 years

Temp=45°C
pH=7.52

| Component | free species | Ctot |
|---|---|---|
| Ca+2 | 0.5719e-01 | 0.6264e-01 |
| Mg+2 | 0.3083e-01 | 0.3756e-01 |
| Na+ | 0.1055e+01 | 0.1199e+01 |
| K+ | 0.4890e-01 | 0.5043e-01 |
| Fe+2 | 0.1156e-08 | 0.1435e-08 |
| SiO2(aq) | 0.1123e-03 | 0.1309e-03 |
| AlO2- | 0.2193e-07 | 0.2498e-07 |
| Cl- | 0.1539e+01 | 0.1700e+01 |
| HCO3- | 0.1816e-03 | 0.3914e-03 |
| SO4-2 | 0.5711e-11 | 0.9999e-06 |
| O2(aq) | 0.6843e-71 | -0.1586e-03 |
| Li+ | 0.9999e-06 | 0.9999e-06 |
| I- | 0.9999e-06 | 0.9999e-06 |
| Ba+2 | 0.9999e-06 | 0.9999e-06 |
| Br- | 0.9999e-06 | 0.9999e-06 |
| Sr+2 | 0.9999e-06 | 0.9999e-06 |
| Mn+2 | 0.9999e-06 | 0.9999e-06 |
| NH4+ | 0.9999e-06 | 0.9999e-06 |

## 7.2. Sealed caprock: 1D simulations

### 7.2.1. Short-term behavior

Several attempts have been made to simulate the geochemical evolution of a simplified 1D system, consisting of a vertical section of 1 $m^2$ cross-sectional area through the caprock, which is bounded at the bottom by time-independent conditions corresponding to a $CO_2$ storage reservoir. The predominant mass transport active in the system is molecular diffusion in the caprock. Sensitivity with respect to parameters such as grid geometry,

mineralogical composition of reservoir and caprock, initial chemical composition of caprock water and thermodynamic parameters has been investigated.
In contrast, parameters like temperature, pressure, and chemical composition of reservoir water, have been maintained constant during the simulations. Representative values used for these parameters are constrained by field and laboratory data. Due to the large variability of "real" measured parameters, only selected average values have been implemented in the numerical model to simulate a "prototypical reference scenario" (hereinafter called PRS).

Below the results of some of these simulations are presented, which provide insight into natural processes that are likely to occur at the interface between reservoir and a caprock physically and mineralogically homogeneous, still maintaining its original sealing efficiency. When relevant, results are also compared with other simulations with different initial conditions to check the sensitivity of the model.

One-dimensional diffusion through the caprock induced by chemicals in the reservoir has been simulated by specifying a grid block in reservoir conditions at the bottom of a 10.093 m long column. The volume of the reservoir block is 10 $m^3$, while the caprock has been discretized using small grid spacing of the order of a few mm near the bottom, with thickness increasing towards the top of the column. The model grid is finer near the interface with the reservoir to better resolve chemical concentrations in the low-permeability caprock. The calculation (nodal) point for the reservoir block has been set in close proximity to the interface. Full details on grid geometry are given in Table 13.

*Table 13 – Grid specifications – order is from top to the bottom*

| Rock domain | n.of elements | thickness (m) | name of the element |
|---|---|---|---|
| caprock layer 8 | 9 | 1.000 | CAP 8 to CAP16 |
| caprock layer 7 | 1 | 0.729 | CAP 7 |
| caprock layer 6 | 1 | 0.243 | CAP 6 |
| caprock layer 5 | 1 | 0.081 | CAP 5 |
| caprock layer 4 | 1 | 0.027 | CAP 4 |
| caprock layer 3 | 1 | 0.009 | CAP 3 |
| caprock layer 2 | 1 | 0.003 | CAP 2 |
| caprock layer 1 | 1 | 0.001 | CAP 1 |
| reservoir | 1 | 10.000 | RES 1 |

Both reservoir and caprock were assumed to behave as porous media. The reservoir is initialized as a two-phase block with initial $CO_2$ gas saturation $S_g = 0.3$, whereas the caprock is assumed to be fully liquid-saturated ($S_L = 1.0$). Sensitivity with respect to initial reservoir gas saturation has been explored, and simulations were done for initial reservoir gas saturations varying from 0.1 to 0.9. Initial mineralogical compositions are from Table 2, whereas initial chemical composition of reservoir and caprock waters are from Table 3 and Table 10, respectively.

Temperature (T = 45°C) and total pressure ($P_{TOT}$ = 105 bar) are fixed throughout the column. The effect of gravity has not been taken into consideration in the PRS simulation, because gravity has a negligible effect on the geochemical calculations under the specified conditions.

The duration of the simulation is 100 years.

Under the initial conditions outlined above, transport occurs in the caprock exclusively by molecular diffusion only when capillary effects are neglected in the two-phase reservoir (**case ii**). In contrast, when capillary effects are accounted for (**case i**), the general behavior of the system is not purely diffusion-controlled, as capillary effects induce advective flows at the reservoir-caprock interface which overwhelm the diffusively-driven behavior. In particular, the first caprock block makes a transition to two-phase conditions because of advective removal of water from the first block of the caprock, due to capillary suction from the reservoir block in two-phase conditions.

The two different cases are discussed in some detail below.

**Case i) mixed diffusive-advective transport.** The capability of this simulation to predict the effective advancement of the reactive front into the caprock strictly depends on the reliability of physical parameters used in the model. This is because capillary suction is the main process controlling in the short-term the mass transport at the reservoir-caprock boundary.

Due to gas ingression into the caprock, the system under investigation is characterized by a strong reactivity. As a consequence, massive dissolution/precipitation reactions occur, and the porosity declines to near zero in the second element of the caprock after only 6.6 years (Figure 14). The calculation point of this element is located at 2.5 mm from the interface with the reservoir. The time of sealing depends on the maximum time step, $\Delta$t_max, set in the input file. More stringent time step controls lead to earlier sealing. For instance, by setting $\Delta$t_max = 5.e+3 s, the plugging of void spaces from mineral precipitation occurs after only 2 years (Figure 15).

In contrast, porosity is not significantly affected by water-rock interactions within the reservoir block and the caprock element with calculation point at 1.59 m from the interface (CAP 8). During the first 10 years of the simulation this element can be considered representative of “non diffusion-perturbed conditions”, and is plotted in the following diagrams to provide a baseline against which effects of diffusion-driven processes in other grid blocks may be evaluated.

The graph of Figure 14 also shows that porosity is significantly enhanced in the first element of the caprock, whereas above the interface between the first and second element of the caprock a reversal of this pattern occurs, with a marked reduction in pore spaces in the second and, to a lesser extent, in the third element of the caprock. When more stringent $\Delta$t_max conditions are set, the processes of dissolution and precipitation of minerals, and the related enhancement/reduction in porosity, tend to be concentrated in the first and in the second element of the caprock, leading to smoother patterns in the third element of the caprock (CAP 3), with calculation point at 8.5 mm from interface.

The contrasting behavior between elements 1 and 2 of the caprock is strictly correlated with the propagation of the “free-gas front”. In fact, two-phase conditions develop only in the first element of the caprock (Sg = 0.01), where high $P_{CO2}$ conditions and low pH values in the aqueous solution are maintained. That increases the chemical reactivity of the system.

Porosity rapidly declines in second block due to massive precipitation of calcite, induced by (1) aqueous $Ca^{2+}$ increasing strongly in the first block, (2) strong diffusion of aqueous $Ca^{2+}$ into the second block, and (3) buffering of pH in the second block.

Based on pH values distribution, a kind of “geochemical divide” should then be recognized within the column. Such bipartitioning of the system is almost instantaneous and occurs at the interface between the first and the second element of the caprock.
According to this general picture, quite acid conditions (pH = 4.8, Figure 16) stabilize at the beginning of the reaction path within the reservoir and the first element of the caprock, whereas in the upper part of the column pH is buffered at some higher value, around 7.0.

The same behavior is also observed for the short-term simulation carried out with more stringent $\Delta$t_max conditions. The only significant difference in this case is a less effective propagation of the diffusive front in the third element of the caprock (lower value of maximum concentration of tracer) and a steeper decrease in concentration after the beginning of massive precipitation and pore occlusion.

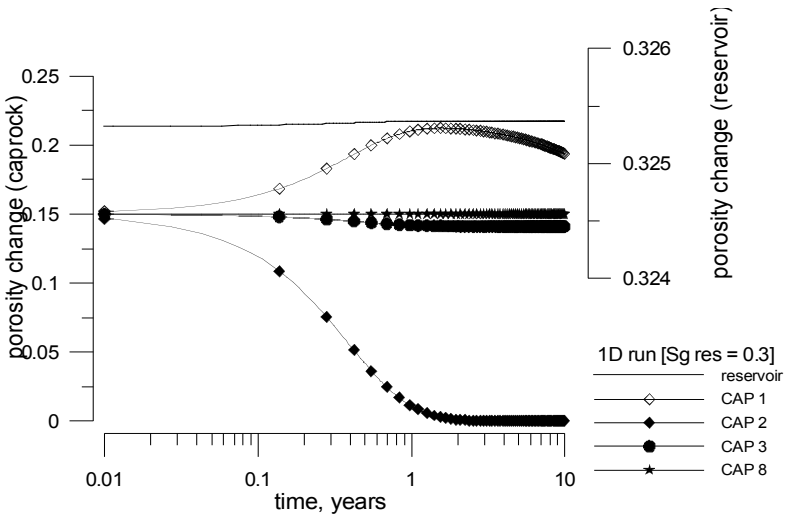


*Figure 14 – Evolution of porosity vs. time for selected grid blocks (detail of first 10 years simulation; maximum time step, $\Delta t\_max$ = 3.16e+4 s; simulation time = 100 yrs). Sealing in the second element of the caprock occurs after 6.6 years.*

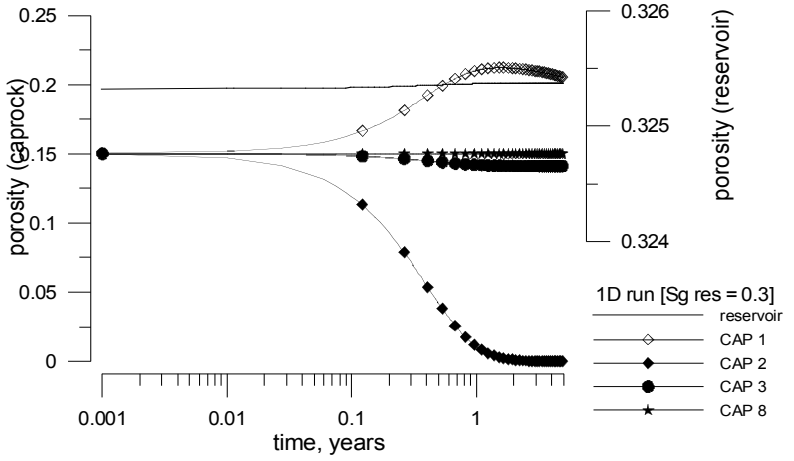


*Figure 15 – Evolution of porosity vs. time for selected grid blocks (detail of first 5 years simulation; maximum time step, $\Delta t\_max$ = 5.e+3 s; simulation time = 10 yrs). Sealing in the second element of the caprock occurs after about 2 years.*

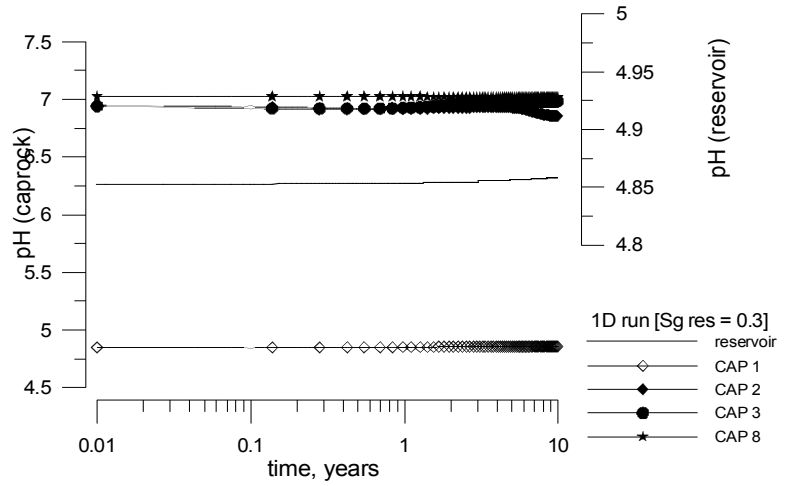


*Figure 16 – Evolution of pH vs. time for selected grid blocks (detail of first 10 years simulation; maximum time step, $\Delta t\_max$ = 3.16e+4 s; simulation time = 100 yrs)*

Inspection of the main aqueous species total concentration variations indicates that $SiO_2(aq)$, $Fe^{+2}$, $AlO_2^-$ and, to a lesser extent, $SO_4^{-2}$ show the most significant variations with time in the caprock, whereas pH, $Ca^{+2}$, $Cl^-$, $Na^+$, $HCO_3^-$, $Mg^{+2}$ and $K^+$ remain almost constant (Figures 17 to 21).

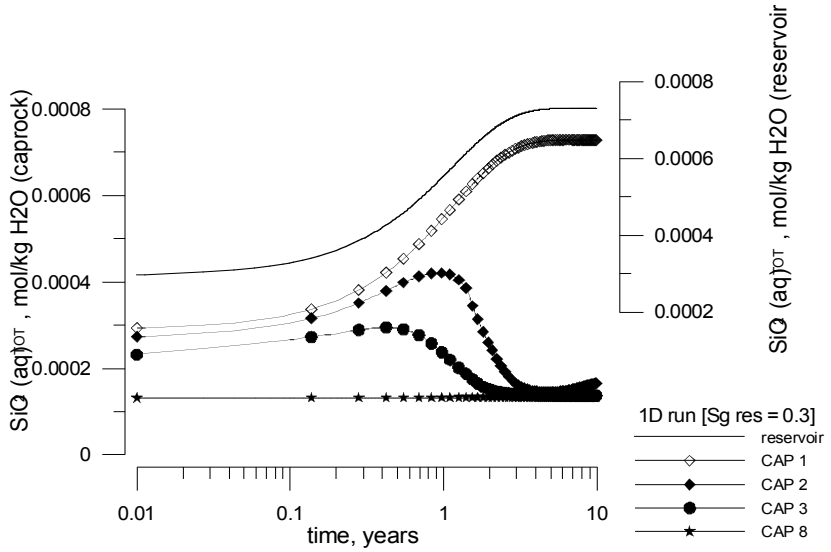


*Figure 17 – $SiO_2(aq)$ aqueous total concentration vs. time for selected grid blocks. (detail of first 10 years simulation; maximum time step $\Delta t\_max$ = 3.16e+4 s; simulation time = 100 yrs).*

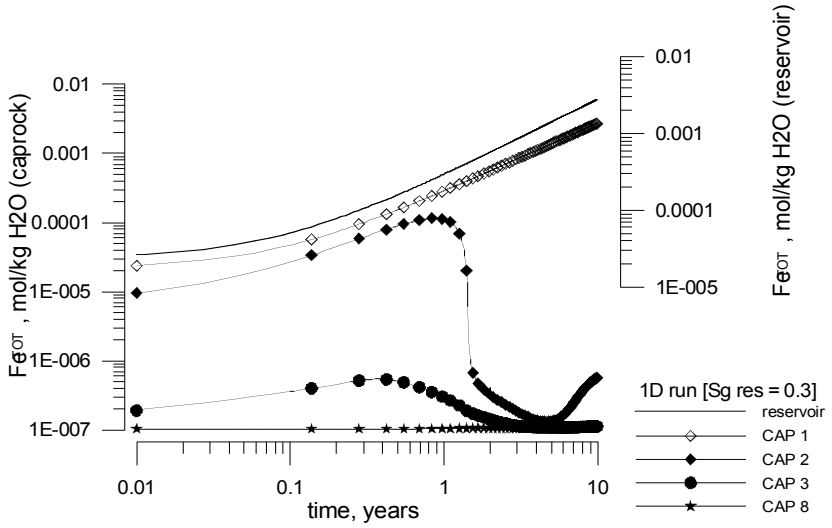


*Figure 18 – $Fe^{+2}$ aqueous total concentration vs. time for selected grid blocks (detail of first 10 years simulation; maximum time step $\Delta t\_max$ = 3.16e+4 s; simulation time = 100 yrs).*

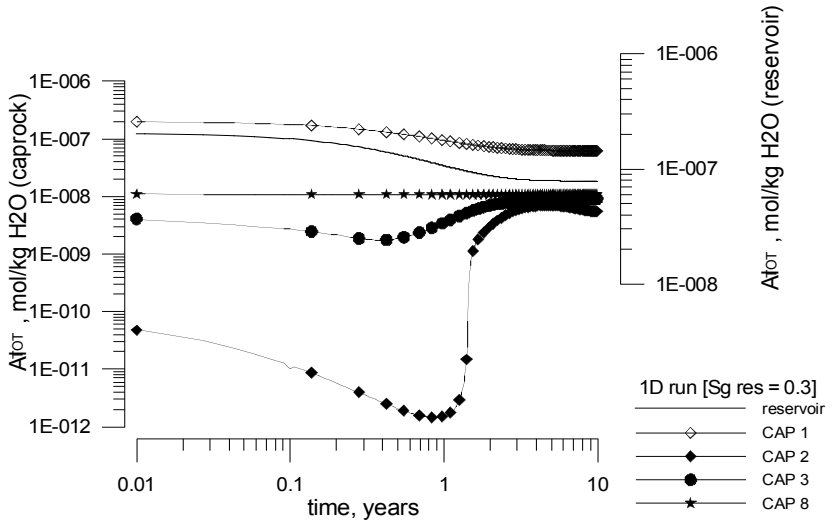


*Figure 19 – $AlO_2^-$ aqueous total concentration vs. time for selected grid blocks (detail of first 10 years simulation; maximum time step $\Delta t\_max$ = 3.16e+4 s; simulation time = 100 yrs).*

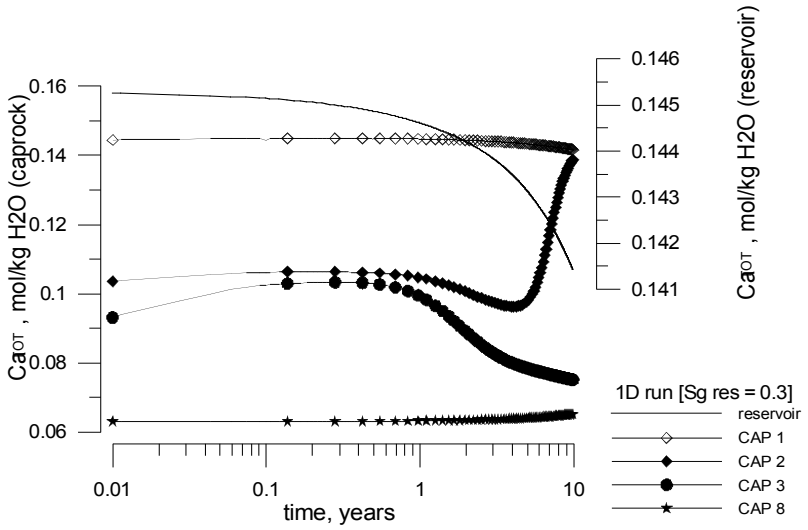


*Figure 20 – $Ca^{+2}$ aqueous total concentration vs. time for selected grid blocks (detail of first 10 years simulation; maximum time step $\Delta t\_max$ = 3.16e+4 s; simulation time = 100 yrs).*

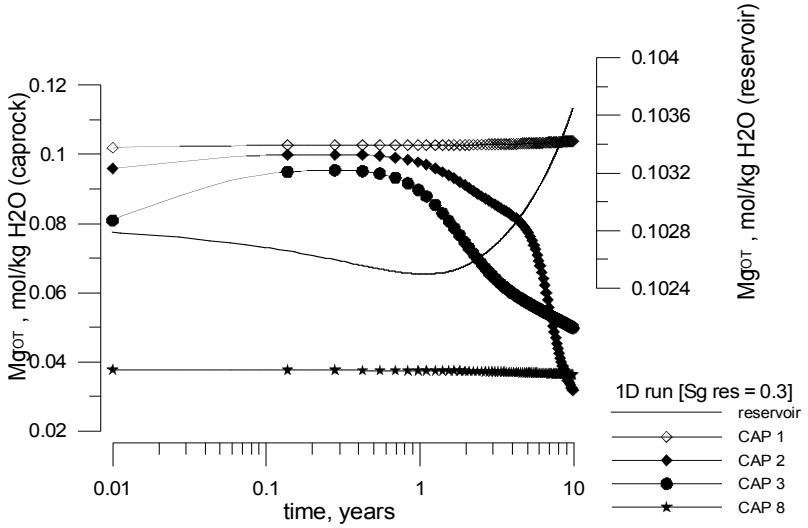


*Figure 21 – $Mg^{+2}$ aqueous total concentration vs. time for selected grid blocks (detail of first 10 years simulation; maximum time step $\Delta t\_max$ = 3.16e+4 s; simulation time = 100 yrs).*

Patterns of aqueous solution components are better interpreted when coupled with changes in mineralogical composition. Figures 22 to 28 show that the most important process controlling the chemical evolution of the system is the dissolution/precipitation of calcite. In particular, calcite tends to dissolve within the reservoir and the first element of the caprock, whereas it precipitates in the upper part of the column, particularly in the second element of the caprock. This behavior is clearly shown in Figure 23, where the changes in volume fraction (with respect to total medium) of calcite and porosity after 5 years simulation are shown for the reservoir and the first 100 cm of the caprock. By inspection of these patterns, a clear inverse correlation between calcite precipitation/dissolution and porosity decrease/increase near the reservoir-caprock interface is recognized.

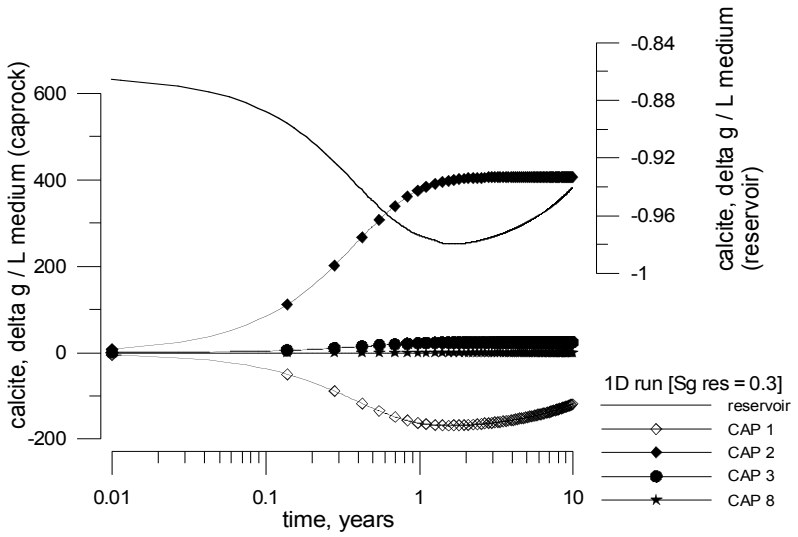


*Figure 22 – Change of calcite concentration (delta gram mineral per liter of medium) vs. time for selected grid blocks (detail of first 10 years simulation; maximum time step ∆t_max = 3.16e+4 s; simulation time = 100 yrs).*

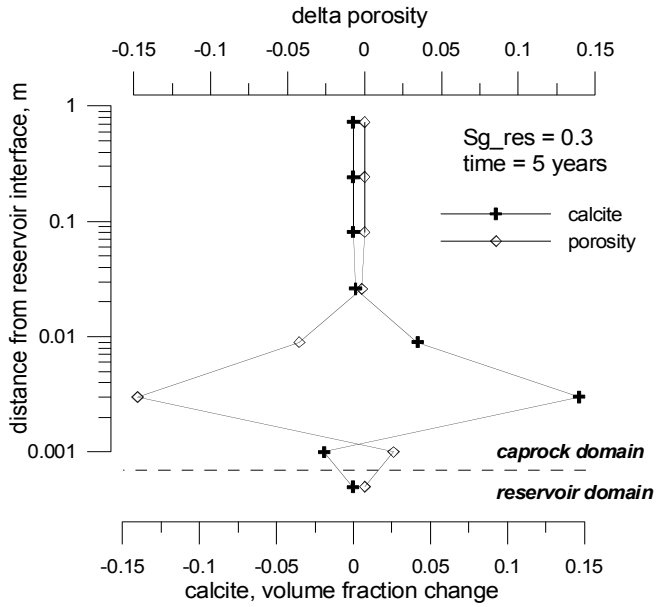


*Figure 23 – Change in calcite volume fraction and porosity in the reservoir and along the column (detail of first 100 cm) after 5 years simulation.*

Dissolution of calcite in the reservoir and first element of the caprock is driven by acid pH conditions induced by high $P_{CO2}$ values. Calcite dissolution makes available further $Ca_{TOT}$ and $HCO_{3,TOT}$ to the aqueous solution. High $P_{CO2}$ values also imply high $CO_{2,aq}$ activities. $Ca_{TOT}$ and $HCO_{3,TOT}$ diffuse into the caprock, as lower concentrations of these species are present in the upper part of the caprock. The concentration gradient between reservoir and first element of the caprock on the one hand, and the upper part of the caprock column

on the other, is large and induces an upward, nearly constant flux of these (and other) species through the column (see Figure 24).
Diffusive flux of $Ca_{TOT}$ and $HCO_{3,TOT}$ leads to calcite precipitation and sealing of void spaces in the second element of the caprock, where fully liquid ($S_L$ = 1.0) and near neutral (pH ≈ 7.0) conditions still persist. This process is predominant over the competing $H^+$ diffusion process induced by acidification of the reservoir. In the idealized conditions of the proposed model, the mineralogical composition of the system acts as an effective buffer which impedes further propagation of the acid front created by high $P_{CO2}$(g) conditions in the reservoir. Sealing occurs rapidly due to very fast kinetics of calcite precipitation.

This overall behavior can be easily traced in terms of calcite saturation index, as shown by the vertical profile of Figure 24. Data after 5 years simulation indicate that calcite is slightly undersaturated in the RES 1 and CAP 1 grid blocks, and slightly oversaturated in the second element of the caprock (SI = +0.0012). Such a small degree of oversaturation, maintained by the almost constant ($[Ca^{+2}] + [HCO_3^-]$) / $[H^+]$ ratio of the diffusing fluids, provides the thermodynamic driving force which induces the efficient calcite precipitation predicted by the code (3.3e-6, 3.0e-6 and 9.2e-7 mol/sec after 0.1, 1 and 5 years, respectively).

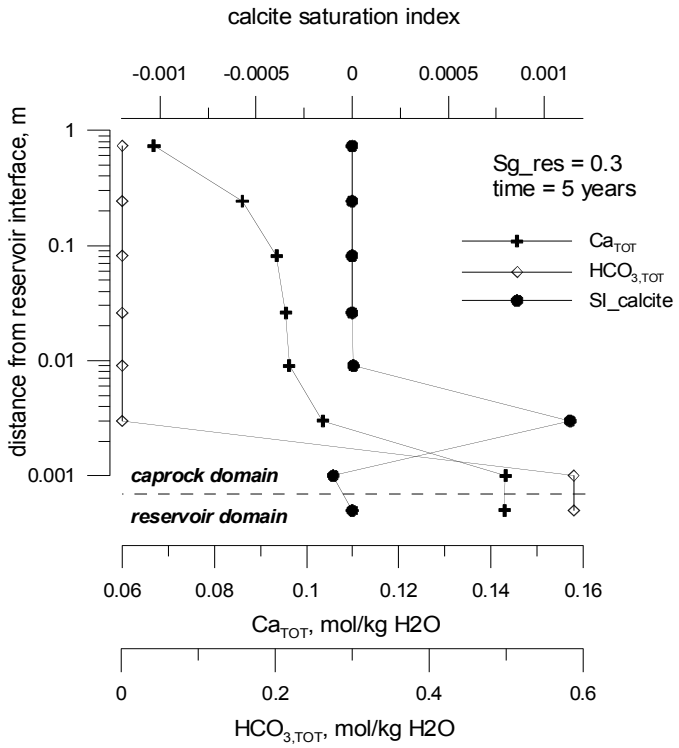


*Figure 24 – Change in $Ca_{TOT}$ and $HCO_{3,TOT}$ aqueous concentration and calcite saturation index in the reservoir and along the column (detail of first 100 cm) after 5 years simulation.*

In agreement with different pH conditions developing along the column, the mineralogy evolves following quite different trends on the opposite sides of the one-to-two-phases interface. Precipitation/dissolution processes involving minerals other than calcite are not significant for the control of porosity during the first 10 years of simulation, but in some cases they play a significant role in terms of control of the chemical composition of the aqueous solution. The most relevant processes are those involving dolomite, illite, chlorite and Na-smectite.

Dolomite (Figure 25) and illite (Figure 26) tend to precipitate and dissolve, respectively, within both reservoir and caprock domains. In contrast, chlorite (Figure 27) and Na-smectite (Figure 28) show a more complicated and opposite behavior: chlorite precipitates in elements 2 and 3 of the caprock (with calculation points at 2.5 and 8.5

mm from interface) and dissolves within the reservoir and first element of the caprock, whereas the opposite occurs for Na-smectite.

These reactions control most of the aqueous chemistry, and particularly $Mg^{+2}$ aqueous concentrations, as this element is present in all these minerals. Dissolution of illite in the caprock makes available in solution also significant amounts of $Fe^{+2}$, which then diffuses through the caprock leading to precipitation of minor secondary ankerite and siderite throughout the system, reservoir included.
$K^+$ amounts derived from dissolution of illite are partly fixed within the reservoir as muscovite and K-feldspar, and partly diffuse through the caprock where they mostly remain in aqueous solution. The resulting pattern in the reservoir is of progressive $K^+$ depletion.

$Na^+$ concentrations change according to the chemical gradient present in the system, i.e. they tend to back-diffuse from caprock to reservoir. This “reverse” chemical gradient is partly due to the slightly different initial free $Na^+$ concentrations in the two domains (more $Na^+$ in the caprock), and in part is also enhanced by the dissolution of Na-smectite occurring in the caprock. Na-smectite and dawsonite precipitation in the reservoir only partially buffer $Na^+$ concentrations, due to the relatively slow kinetics of these minerals (in particular Na-smectite), and due to the continuous supply of this ion deriving from the concomitant dissolution of albite. The net effect of all these processes is a smoothed increase in $Na^+$ concentration within the reservoir.

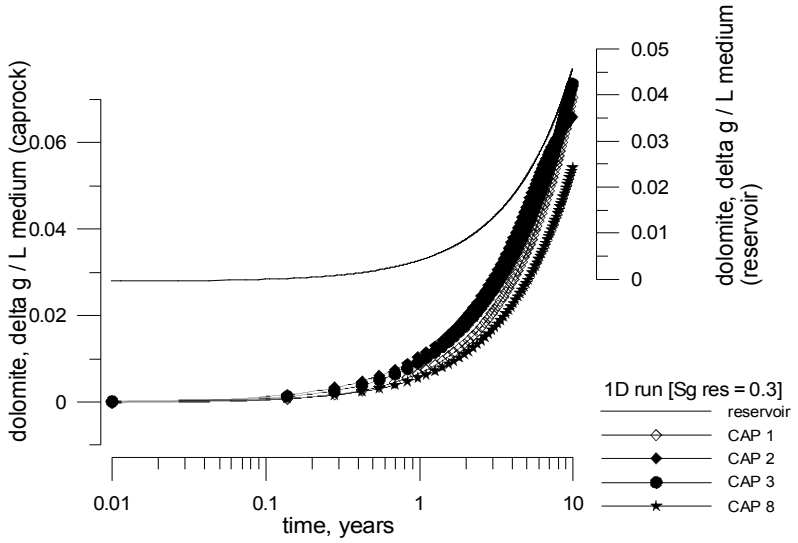


*Figure 25 – Change of dolomite concentration (delta gram mineral per liter of medium) vs. time for selected grid blocks (detail of first 10 years simulation; maximum time step $\Delta t\_max$ = 3.16e+4 s; simulation time = 100 yrs).*

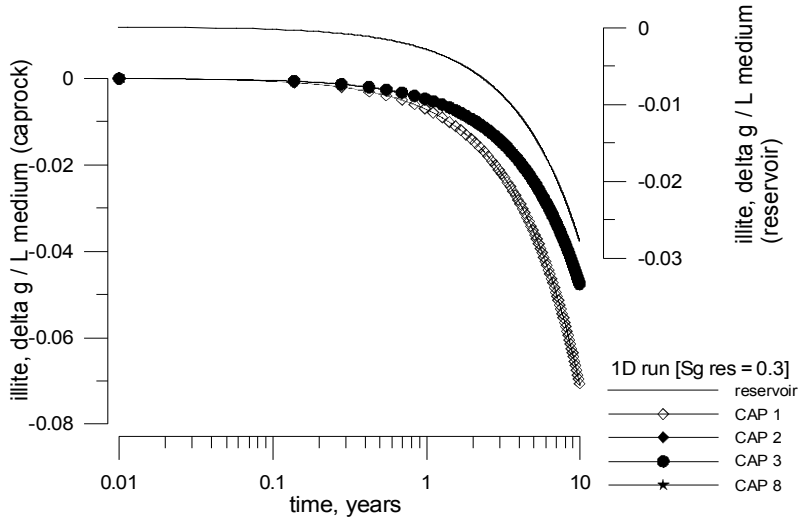


*Figure 26 – Change of illite concentration (delta gram mineral per liter of medium) vs. time for selected grid blocks (detail of first 10 years simulation; maximum time step ∆t_max = 3.16e+4 s; simulation time = 100 yrs).*

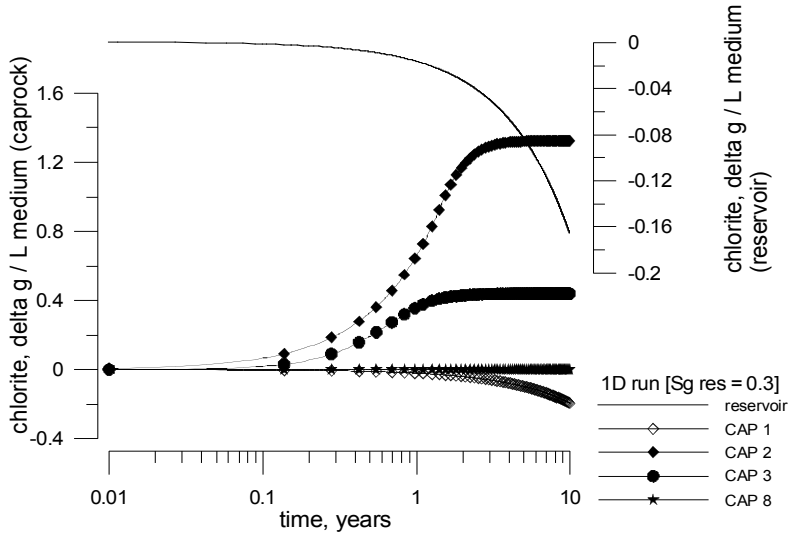


*Figure 27 – Change of chlorite concentration (delta gram mineral per liter of medium) vs. time for selected grid blocks (detail of first 10 years simulation; maximum time step ∆t_max = 3.16e+4 s; simulation time = 100 yrs).*

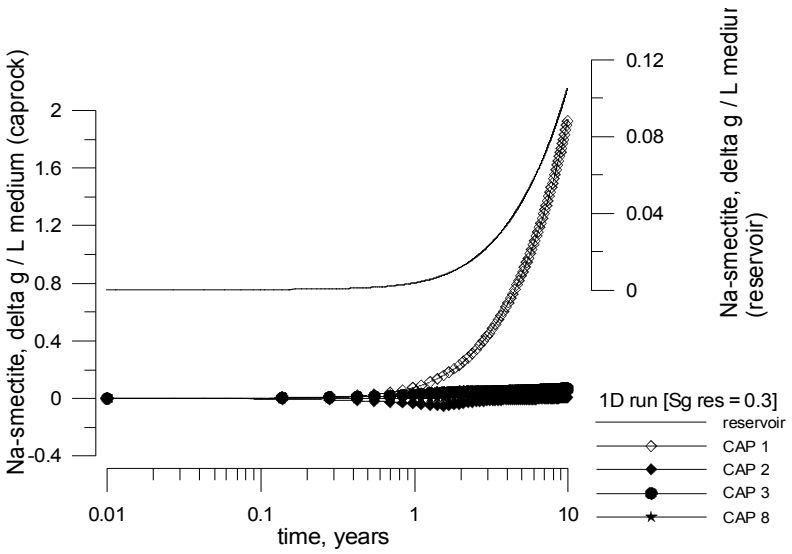


*Figure 28 – Change of Na-smectite concentration (delta gram mineral per liter of medium) vs. time for selected grid blocks (detail of first 10 years simulation; maximum time step ∆t_max = 3.16e+4 s; simulation time = 100 yrs).*

Total silica and $Al_{TOT}$ concentration patterns reflect the interplay of almost all of the process previously described, as both of these species are involved in the precipitation/dissolution reactions of all the silicates and Al-silicates taken into consideration in the simulation. In particular, $SiO_2(aq)_{TOT}$ concentrations increase by a factor greater than two in the reservoir, due to a net positive balance between source terms, represented by illite, chlorite and albite dissolution, and sink terms, represented by quartz, kaolinite, K-feldspar, muscovite, Na- and Ca-smectite precipitation.

$Al_{TOT}$ shows a complex pattern, characterized by an increase in the grid blocks where two-phase conditions develop (reservoir and first element of the caprock), due to a local predominance of Al-silicate dissolution over precipitation reactions, and an initial decrease in the adjacent elements of the caprock (CAP 2 and CAP 3), due to a reversal of this unbalanced condition.

The chemical composition of the aqueous solution and mineralogical composition of rocks remain almost constant with time in the grid block at 1.59 m from the reservoir interface. This further confirms the absence of diffusion-induced perturbations at this level of the column.

**Case ii) purely diffusion-controlled transport.** In the absence of capillary forces acting within the reservoir, all the elements of the caprock remain in liquid conditions and no advective flow occurs. Under these conditions the geochemical effects driven by molecular diffusion in the aqueous phase can be easily investigated.
As no gas front advancement is observed, pH remains buffered at some near-neutral values (between 6.92 and 7.04, depending on time) also in the first element of the caprock (Figure 29), due to calcite precipitation (Figure 30). Calcite precipitation occurs almost instantaneously in the first element of the caprock (Figure 31) with an increase of about 400 g/L medium in less than 1 year. As expected (see section on zero-dimensional simulations), calcite initially slightly dissolves in the reservoir (up to -0.95 g/L medium after about 1 year), and then precipitates (+0.02 g/L medium in the time range between 1 and 5 years). Initial calcite dissolution in the reservoir makes available further $Ca_{TOT}$ and $HCO_{3,TOT}$ in aqueous solution, which diffuse into the caprock where lower initial concentrations occur. Due to the high initial difference in concentration between the reservoir and caprock domains, $Ca^{+2}$ supply from reservoir (Figure 32) remains almost constant in time until the pores clog (porosity declining to zero in the first element of the caprock after only 1 year, see Figure 33). In contrast, $HCO_3^-$

increases in the caprock only at early times (see 0.01 and 0.1 years patterns in Figure 34), because it is then efficiently removed by calcite precipitation (see 0.5 and 1 year patterns). Diffusively-controlled behavior of the system is appropriately described in Figure 35 by plotting the concentration of an inert tracer.

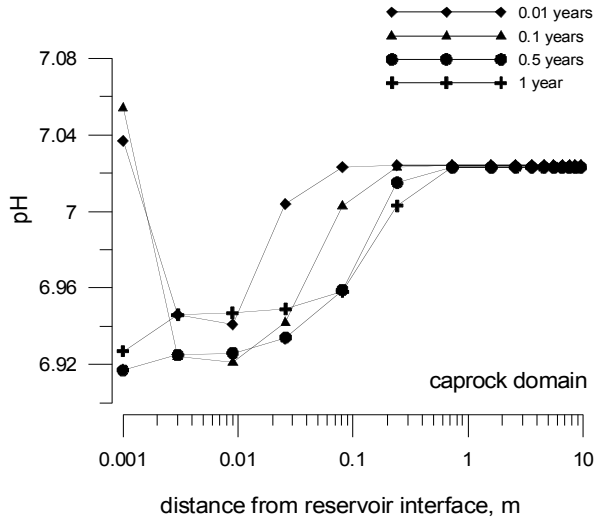


*Figure 29 – Caprock pH at four selected times before pores clogging in the first element (1D simulation, reservoir $S_L$=0.7)*

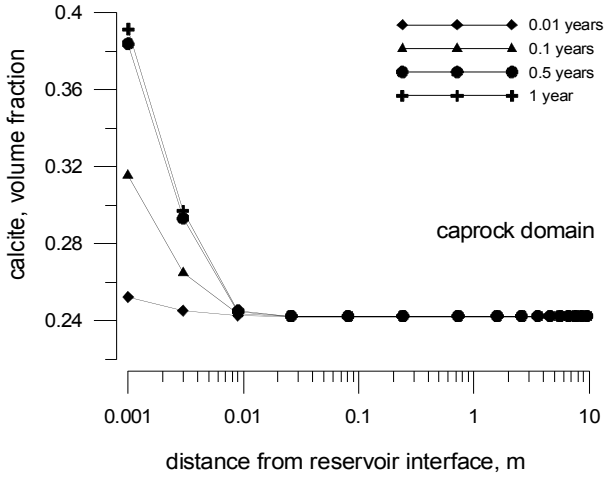


*Figure 30 – Calcite volume fraction in the caprock at four selected times before pores clogging in the first element (1D simulation, reservoir $S_L$=0.7)*

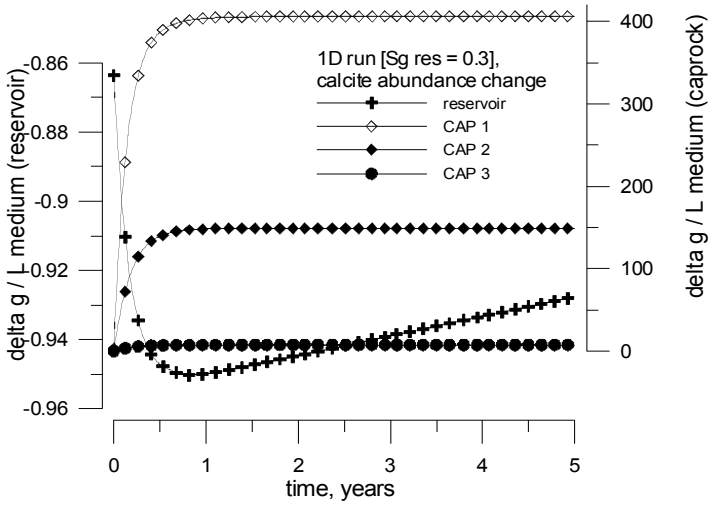


*Figure 31 – Calcite abundance variation (g/L medium) for reservoir domain and first three elements of the caprock in the first 5 years simulation (1D simulation, reservoir $S_L$=0.7)*

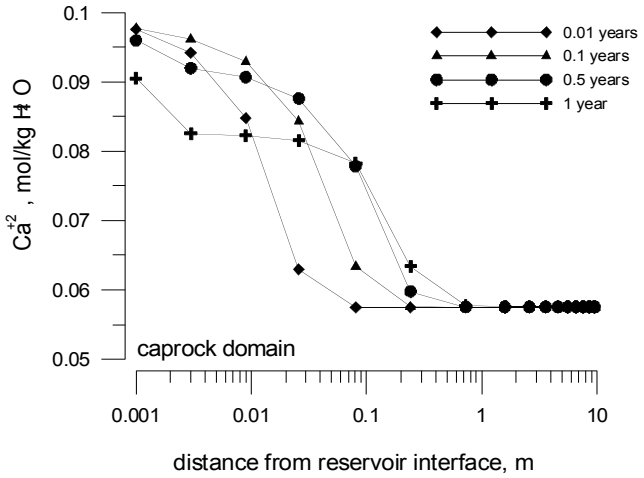


*Figure 32 – Caprock $Ca^{+2}$ profile at four selected times before pores clogging in the first element (1D simulation, reservoir $S_L$=0.7)*

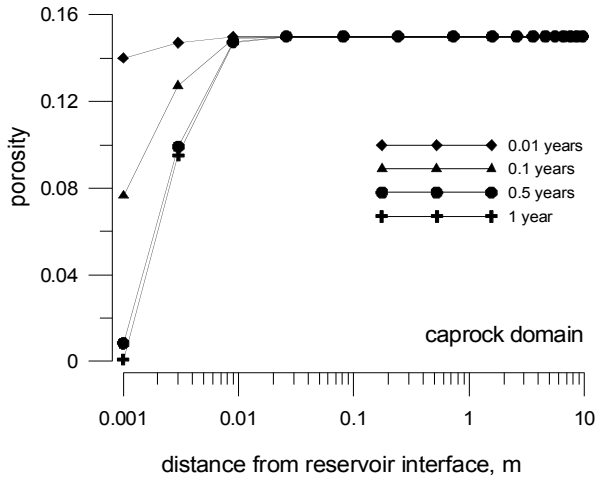


*Figure 33 – Variation of caprock porosity at four selected times before pores clogging in the first element (1D simulation, reservoir $S_L$=0.7)*

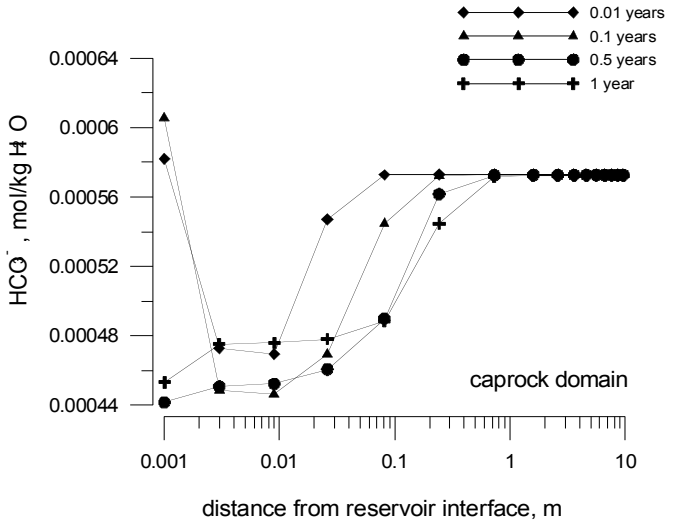


*Figure 34 – Caprock $HCO_3^-$ profile at four selected times before pores clogging in the first element (1D simulation, reservoir $S_L$=0.7)*

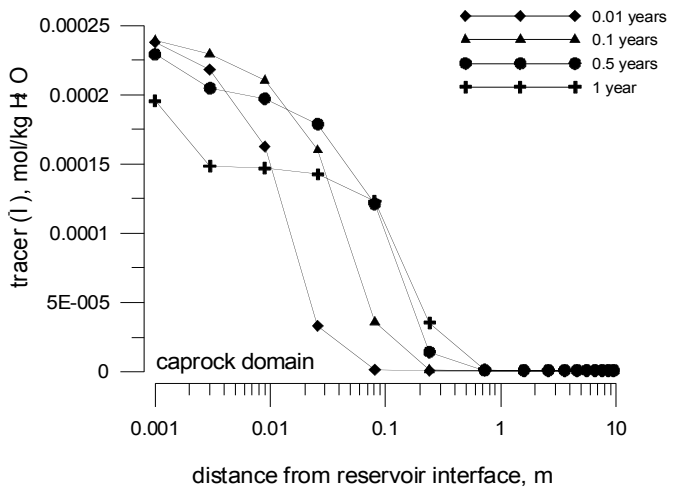


*Figure 35 – Propagation of the diffusive front in the caprock as shown by tracer concentration change (1D simulation, reservoir $S_L$=0.7)*

Grid geometry effects have been investigated in some detail to explore the "critical dimension" of the first element of the caprock that controls how chemicals diffusing from the reservoir are buffered by initial caprock mineralogy and water composition. Sensitivity of calcite precipitation has been checked by varying the thickness and internodal distance of the first element of the caprock.

Inspection of Figure 36 reveals that pore clogging of the first element of the caprock is prevented by increasing to 0.025 m the distance between the first nodal point of the caprock and the reservoir-caprock interface. This is because the corresponding increase in the volume (now equal to 0.05 $m^3$) allows the $Ca_{TOT}$ and $HCO_{3,TOT}$-rich fluids diffusing from the reservoir to mix with a larger amount of caprock initial aqueous solution, making less oversaturated the solution of the first element of the caprock (Figure 37). This effect can be also monitored in terms of less sharp Ca gradients between reservoir and caprock (Figure 38), and, most importantly, in less effective calcite precipitation in first element of the caprock (Figure 39).

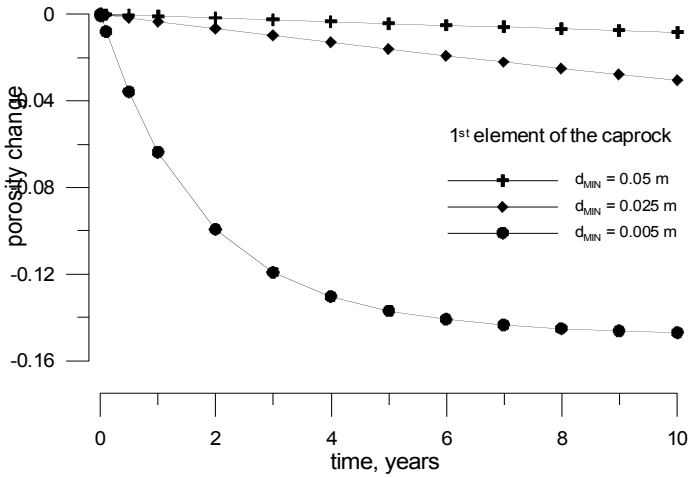


*Figure 36 – Change of porosity in the first element of the caprock as a function of different initial grid specifications (1D simulation, reservoir $S_L$=0.7)*

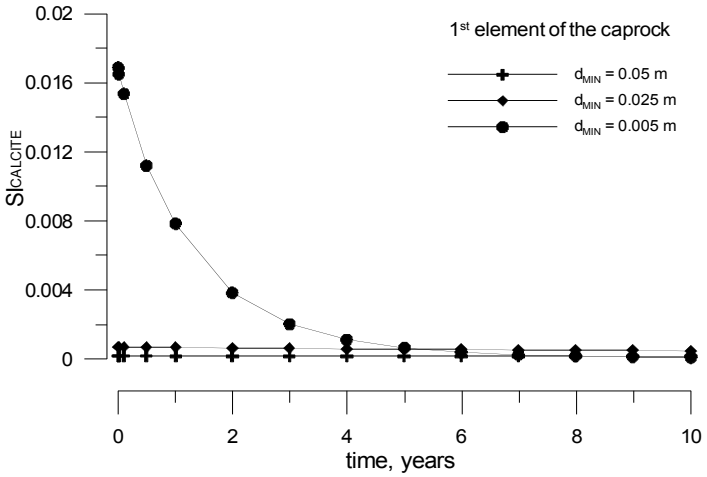


*Figure 37 – Variation of calcite saturation index in the first element of the caprock as a function of different initial grid specifications (1D simulation, reservoir $S_L$=0.7)*

Finally, a further simulation has been carried out under intermediate conditions, i.e. with a minimum internodal distance of 0.01 m, and a caprock first element volume of 0.02 $m^3$, to trace the asymptotic pores clogging tendency of the system when the complex interplay between diffusive fluxes from reservoir and kinetic rates of calcite is somewhat balanced. In particular, the patterns shown in Figure 40 reveal that with the grid specifications listed above, a progressive calcite precipitation is induced which causes the porosity to reach a minimum of about 1.7e-3 after 50 years.

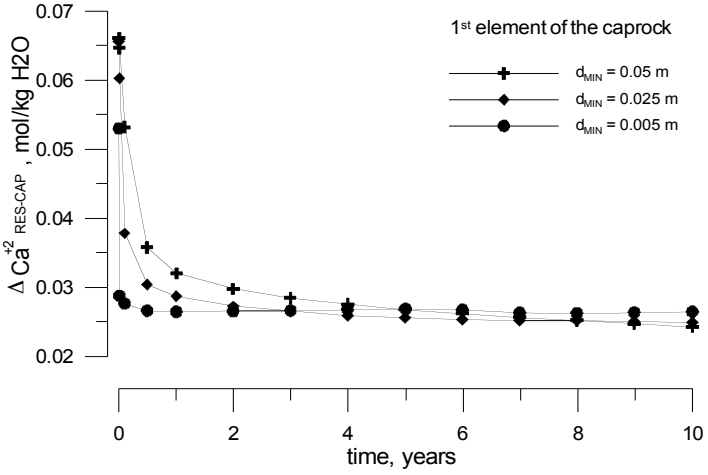


*Figure 38 – Attenuation of reservoir-caprock $Ca^{+2}$ gradient as a function of different initial grid specifications (1D simulation, reservoir $S_L$=0.7)*

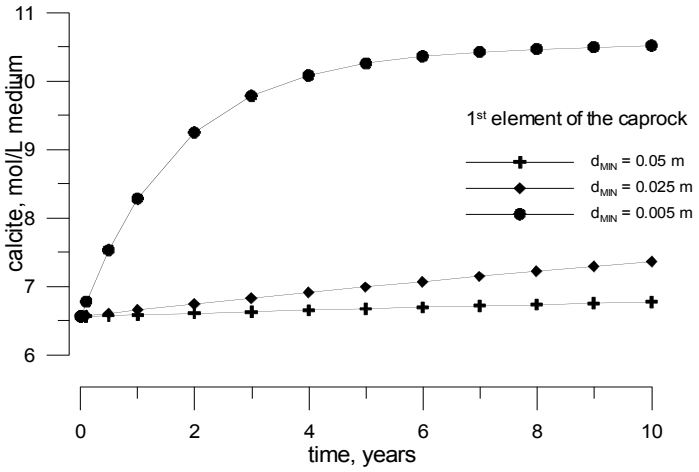


*Figure 39 – Calcite precipitation in the first element of the caprock as a function of different initial grid specifications (1D simulation, reservoir $S_L$=0.7)*

In order to better understand the natural mechanisms reproduced by the simulation and check the sensitivity of the model, another simulation has been carried out by assuming that diffusion process is driven from a large volume reservoir element maintained at full liquid conditions ($S_L$ = 1.0). All the other chemical and physical parameters are the same as in the previous simulations, grid geometry and time stepping specifications included.

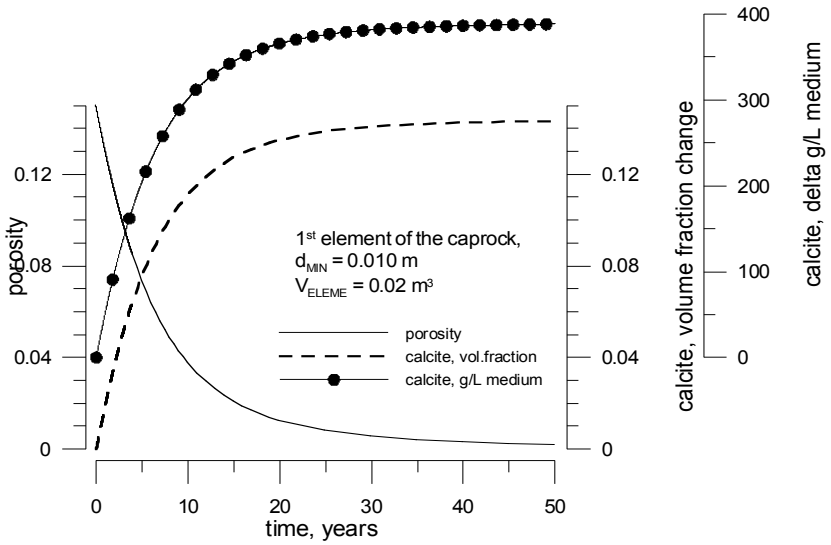


*Figure 40 – Porosity and calcite abundance (as volume fraction and g/L medium) variation in the first element of the caprock vs. time for $d_{MIN}$ = 0.01 m (1D simulation, reservoir $S_L$=0.7)*

The most relevant characteristics of this run could be monitored in terms of porosity, pH and calcite behavior, as shown in Figures 41, 42 and 43. The main observation is that, under these conditions, the sealing of the first element of the caprock, with calculation point at 0.5 mm from the reservoir, still occurs very early (i.e. after only about 1 year) due to calcite precipitation.

This general behavior reflects the important role played by the gas front propagation in the control of the chemical evolution of the system: where two phase conditions develop, low pH values occur and calcite dissolves leading to an enhancement of porosity. In contrast, where fully liquid conditions persist, $Ca_{TOT}$ and $C_{TOT}$ diffusion predominates, leading to fast calcite precipitation, and then, sealing of the caprock.

Our simulations demonstrate that precipitation behavior is strongly dependent on grid resolution, which of course is a modeling artifact. The grid sensitivity suggests that porosity changes due to $CO_2$-induced rock-fluid interactions in actual field conditions will be strongly affected by hydrologic and chemical heterogeneity.

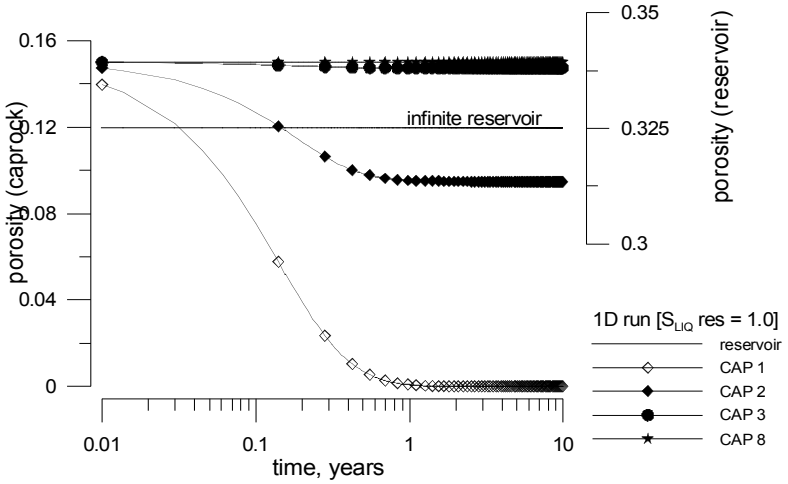


*Figure 41 – Evolution of porosity vs. time for selected grid blocks (maximum time step, $\Delta t\_max$ = 5.e+3 s; simulation time = 10 yrs). In this case, the reservoir has been modeled as a large volume of fixed chemical and mineralogical composition at full liquid conditions ($S_L$=1.0), at the same P,T conditions of previous runs: sealing occurs in the first element of the caprock after only about 1 year)*

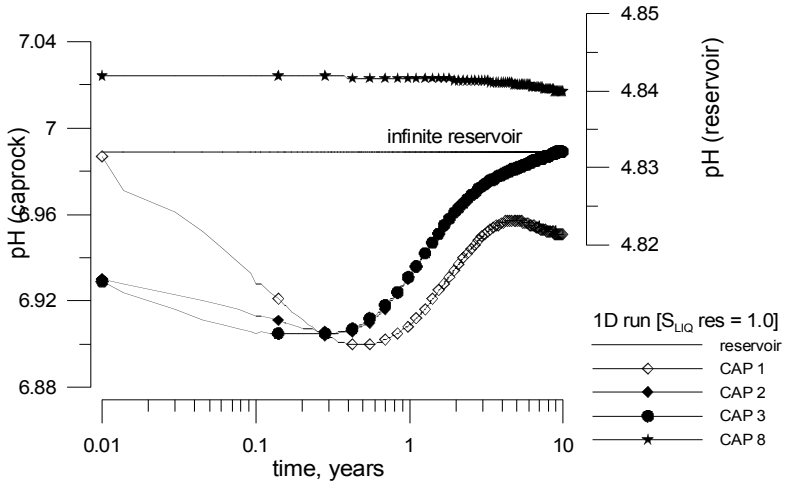


*Figure 42 – Evolution of pH vs. time for selected grid blocks (maximum time step, $\Delta t\_max$ = 5.e+3 s; simulation time = 10 yrs). In this case, the reservoir has been modeled as a large volume of fixed chemical and mineralogical composition at full liquid conditions ($S_L$=1.0), at the same P,T conditions of previous runs: sealing occurs in the first element of the caprock after only about 1 year)*

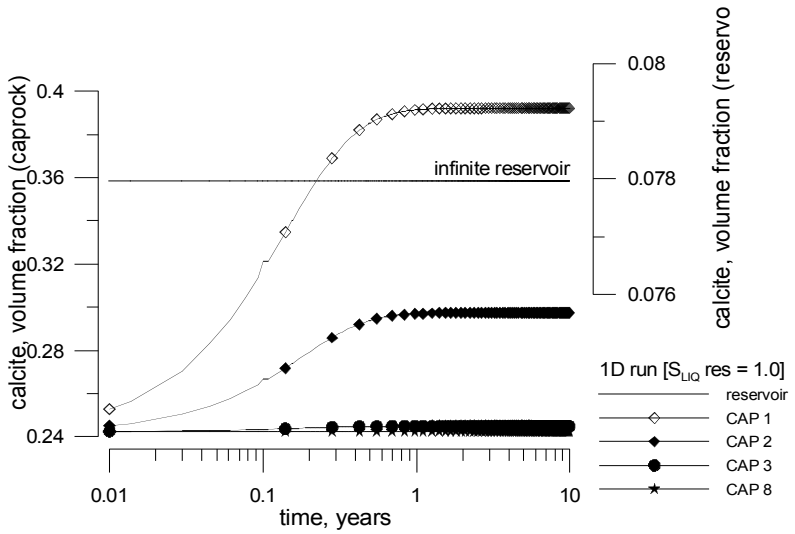


*Figure 43 – Change in volume fraction of calcite vs. time for selected grid blocks (maximum time step, $\Delta t\_max$ = 5.e+3 s; simulation time = 10 yrs). In this case, the reservoir has been modeled as a large volume of fixed chemical and mineralogical composition at full liquid conditions ($S_L$=1.0), at the same P,T conditions of previous runs: sealing occurs in the first element of the caprock after only about 1 year)*

## 7.2.2. Medium-term and maximum risk scenario

On the basis of data from previous simulations, a “maximum risk” scenario has been delineated in which caprock water-rock interactions occur in presence of a predominant $CO_2$-rich gas phase. To reproduce these conditions, two models have been defined in which $CO_2$ is made to directly penetrate into the caprock without any significant “chemical modulation”. This scenario should be reasonably representative of conditions occurring in the inner part of the $CO_2$ plume, near the injection wells, after the injected $CO_2$ has completely displaced the brines initially present in the reservoir. An outline of the two models is given below.

In the first group of simulations (**case i**), a large, variably overpressurized reservoir almost completely filled with $CO_2$ (Sg = 0.99), is set below the caprock column with the aim to force the gas to move upwards. At the same time, aqueous solution from the caprock is not allowed to move downwards into the reservoir, to avoid spurious advective flows through the column.
In the second group of simulations (**case ii**), $CO_2$ has been directly injected into the bottom element of the caprock by means of an external source term, in a manner that completely excludes the reservoir domain from the simulation.

Both models may describe more realistically than the previous simulations the geochemical effects induced by $CO_2$ propagation through the caprock, and may provide relevant information on time evolution of caprock sealing capacity under boundary conditions less favorable than previously utilized.

In the first model, the extent of reservoir overpressure is the critical parameter that determines the propagation velocity of the gas front; in the second model, this role is played by the $CO_2$ injection rate. As no reliable field data are currently available to constrain these parameters, a sensitivity analysis was performed. Reservoir overpressure has been varied in our simulations between +1 to +20 bar (the maximum overpressure expected in the reservoir due to $CO_2$ injection), and injection rates of (anhydrous) $CO_2$ have been varied between 0.1 to 10 kg $CO_2$ per year.

Here, the results for the injection case (**case ii**) are discussed in some detail, because under these conditions, the calculations allow to characterize the geochemical effects induced by $CO_2$ front advancement in the caprock, without any contribution from reservoir water molecular diffusion.

With respect to previous 1D simulations, in this run the initial porosity (now set to 0.1) and the absolute permeability (now $10^{-17}$ $m^2$) have been changed. In addition, due to the larger maximum simulation time (500 years), the grid spacing ($\Delta z_{MIN}$ = 0.1 m) and the maximum length of the column ($z_{MAX}$ = 50.4 m) have been also increased.

More details on grid discretization are given in Table 14.

*Table 14 – 1D model grid specifications –500 years simulation – order is from top to the bottom*

| Rock domain | number of elements | thickness (m) | name of the element |
|---|---|---|---|
| caprock layer 10 | 15 | 2.0 | ELE26 to ELE40 |
| caprock layer 9 | 17 | 1.0 | ELE 9 to ELE25 |
| caprock layer 8 | 1 | 0.9 | ELE 8 |
| caprock layer 7 | 1 | 0.8 | ELE 7 |
| caprock layer 6 | 1 | 0.7 | ELE 6 |
| caprock layer 5 | 1 | 0.6 | ELE 5 |
| caprock layer 4 | 1 | 0.5 | ELE 4 |
| caprock layer 3 | 1 | 0.4 | ELE 3 |
| caprock layer 2 | 1 | 0.3 | ELE 2 |
| caprock layer 1 | 1 | 0.2 | ELE 1 |
| reservoir | 1 | large volume (10e+30 m3) | RES 1 |

The advancement of a $CO_2$-rich gas phase induces a significant pH lowering in the caprock (Figure 44). After 50 years of simulation, pH is between 4.9 and 5 in the first 5 m of the caprock. After about 100 years, acidification reaches the fifteenth element of the caprock, at 10.90 m from the injection point. The low-pH front is at 15.90 m from the injection point after 200 years, and at 19.90 m, 22.40 m, 30.4 m and 36.4 m after 250, 300, 400 and 500 years, respectively. After about 150 years, the pH is stable at 4.8 - 4.9 in the first 12 m of the caprock.

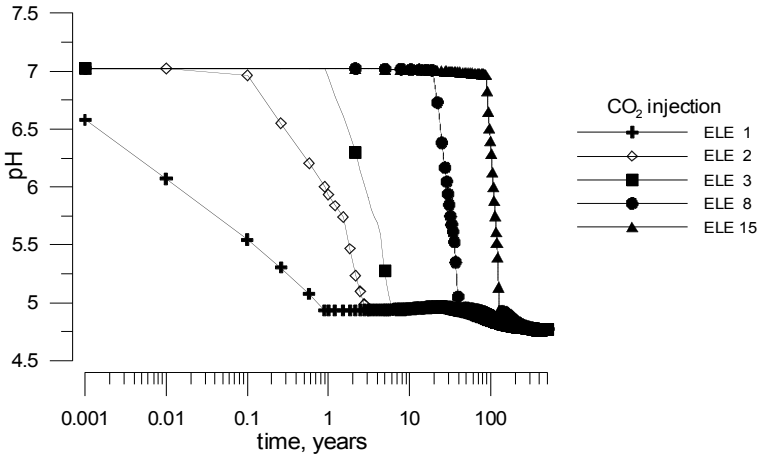


*Figure 44 – pH pattern vs. time for selected grid blocks (1D model, 500 years simulation).*

A supercritical free gas phase develops in the first element of the caprock after only one year, whereas 3 and about 6.2 years are needed for free gas to evolve in the second and third element, respectively (Figure 45). After 500 years the maximum gas saturation level is about 0.22 in first few meters of the caprock, and about 0.2 at 10.90 m from the injection point (ELE15).

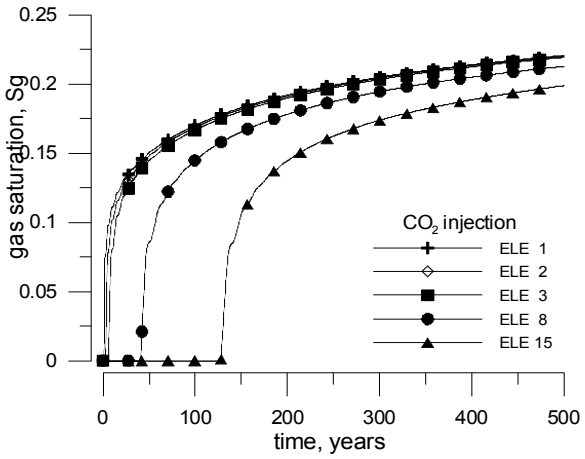


*Figure 45 – Gas saturation pattern vs. time for selected grid blocks (1D model, 500 years simulation).*

After an initial slow increase due to the fast kinetics of calcite dissolution, porosity progressively decreases in the caprock due to the low-pH gas-driven front propagation, which induces some mineralogical modifications in the

clay and carbonate mineral fractions. After 500 years the delta porosity value predicted by the code is less than -0.2% between 35 to 100 cm (ELE 2 to ELE15) from the injection point, and even less (-0.14%) in the first element of the caprock (Figure 46).

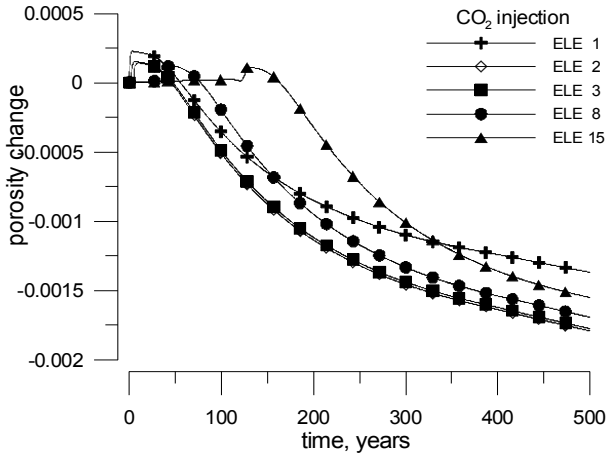


*Figure 46 – Change in porosity vs. time for selected grid blocks (1D model, 500 years simulation).*

Similar results are obtained also when higher injection rates (10 kg $CO_2$ $yr^{-1}$) are applied for longer simulation times (1,000 yrs). As shown in Figure 47, under these conditions the system responds more rapidly, and no appreciable differences in porosity behavior are observed in the first 1,000 years of simulation between elements located at a distance of less than 12 meters from the injection point. The maximum delta value is -0.0022 in the first grid block ELE 1 after 1,000 yrs.

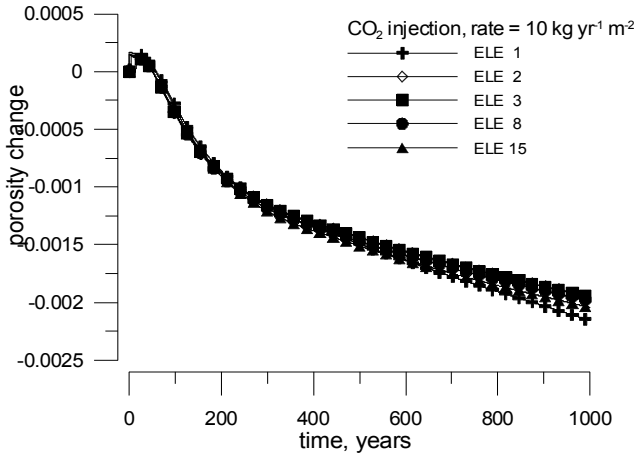


*Figure 47 – Change in porosity vs. time for selected grid blocks (1D model, 1000 years simulation).*

As shown in Table 15, the mineralogical composition of the caprock changes only slightly in response to $CO_2$ injection. Inspection of major mineralogical transformations reveals that porosity behavior results from the interplay of different precipitation/dissolution reactions, which can be summarized as follows:

1) calcite (Figure 48) progressively decreases, with a maximum overall variation between -40 (distal point at 10.90m) and -65 (first element, at 10 cm) moles/$m^3$ medium;

2) carbonate minerals such as dawsonite (Figure 49) and ankerite (Figure 50) tend to form in the caprock; their maximum changes are between +40 and +50 moles/$m^3$ medium after 500 years;

3) dolomite (Figure 51) also steadily increases throughout the caprock, showing positive delta values between +7 to +8 moles/$m^3$ medium after 500 years;

4) reactions involving Al-silicate minerals lead to the dissolution of chlorite (Figure 52) and illite (Figure 53), and precipitation of Na-smectite (Figure 54); maximum concentration changes for these minerals are observed after 500 years, and correspond to about -12, -8 and +30 moles/$m^3$ medium, respectively;

5) muscovite (Figure 55) has a more complex pattern, with an initial dissolution stage (up to -22 moles/$m^3$ medium after about 350 years), and a final precipitation stage which leads to the formation of about 2 moles mineral per $m^3$ medium between 350 and 500 years;

5) minor kaolinite precipitation (less than 1 moles/$m^3$ medium after 500 years, Figure 56) is predicted;

6) finally, quartz shows a non-uniform behavior throughout the column; it tends to precipitate near the injection point, and to dissolve at larger distances (Figure 57); $CO_2$-rich gas front arrival has then the net effect to induce some minor quartz precipitation (up to a maximum of less then 0.25 moles/$m^3$ medium after 500 years).

*Table 15 – Inventory of mineral abundances at the beginning and at the end of $CO_2$-injection run*

***initial conditions, REV volume fraction***

| ELEMENT | porosity | cal | dol | qtz | ill | chl | ank | kaol | Na-sme | daws | musc |
|---|---|---|---|---|---|---|---|---|---|---|---|
| all | 0.1 | 0.257 | 0.033 | 0.184 | 0.018 | 0.055 | 0.000 | 0.046 | 0.136 | 0.000 | 0.171 |

***time = 500 years, REV volume fraction***

| ELEMENT | porosity | cal | dol | qtz | ill | chl | ank | kaol | Na-sme | daws | musc |
|---|---|---|---|---|---|---|---|---|---|---|---|
| ELE 1 | 0.099 | 0.254 | 0.033 | 0.184 | 0.017 | 0.053 | 0.003 | 0.046 | 0.140 | 0.003 | 0.168 |
| ELE 2 | 0.098 | 0.255 | 0.033 | 0.184 | 0.017 | 0.053 | 0.003 | 0.046 | 0.140 | 0.003 | 0.168 |
| ELE 3 | 0.098 | 0.255 | 0.033 | 0.184 | 0.017 | 0.053 | 0.003 | 0.046 | 0.140 | 0.003 | 0.168 |
| ELE 8 | 0.098 | 0.255 | 0.034 | 0.184 | 0.017 | 0.053 | 0.003 | 0.046 | 0.139 | 0.003 | 0.168 |
| ELE15 | 0.098 | 0.255 | 0.034 | 0.184 | 0.017 | 0.053 | 0.002 | 0.046 | 0.139 | 0.002 | 0.168 |

***delta values, REV volume fraction***

| ELEMENT | porosity | cal | dol | qtz | ill | chl | ank | kaol | Na-sme | daws | musc |
|---|---|---|---|---|---|---|---|---|---|---|---|
| ELE 1 | -0.001 | -0.254% | 0.048% | 0.001% | -0.111% | -0.270% | 0.298% | 0.009% | 0.423% | 0.285% | -0.292% |
| ELE 2 | -0.002 | -0.208% | 0.048% | 0.000% | -0.111% | -0.270% | 0.299% | 0.009% | 0.417% | 0.279% | -0.283% |
| ELE 3 | -0.002 | -0.207% | 0.049% | 0.000% | -0.111% | -0.270% | 0.298% | 0.009% | 0.411% | 0.273% | -0.275% |
| ELE 8 | -0.002 | -0.201% | 0.050% | 0.000% | -0.111% | -0.258% | 0.286% | 0.008% | 0.393% | 0.259% | -0.258% |
| ELE15 | -0.002 | -0.171% | 0.051% | 0.000% | -0.109% | -0.218% | 0.225% | 0.007% | 0.370% | 0.247% | -0.252% |

Abbreviations and acronyms are as follows: cal=calcite; dol=dolomite; qtz=quartz; ill=illite; chl=chlorite; ank=ankerite; kaol=kaolinite; Na-sme=Na-smectite; daws=dawsonite; musc=muscovite; REV=representative elementary volume (1 m3 porous medium)

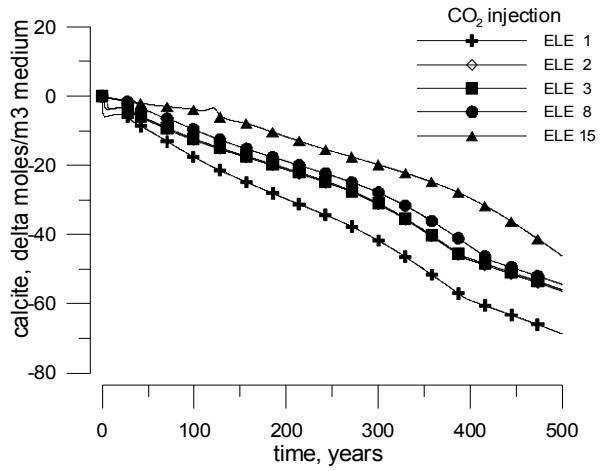


*Figure 48 – Variation of calcite abundance (delta moles per m3 medium) vs. time for selected grid blocks (1D model, 500 years simulation).*

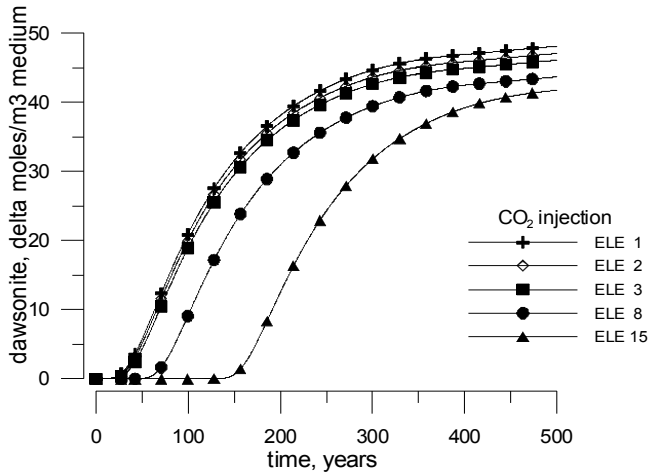


*Figure 49 – Variation of dawsonite abundance (delta moles per m3 medium) vs. time for selected grid blocks (1D model, 500 years simulation).*

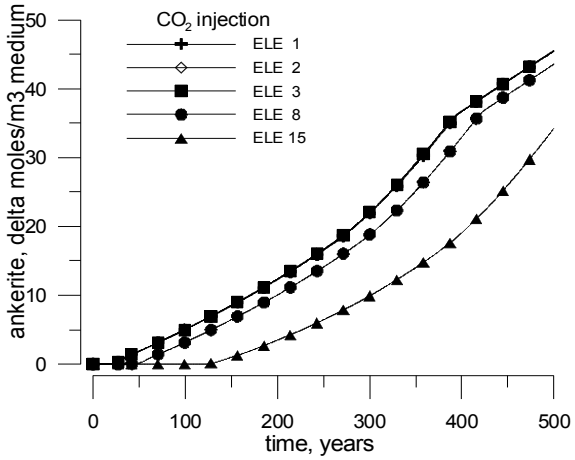


*Figure 50 – Variation of ankerite abundance (delta moles per m3 medium) vs. time for selected grid blocks (1D model, 500 years simulation).*

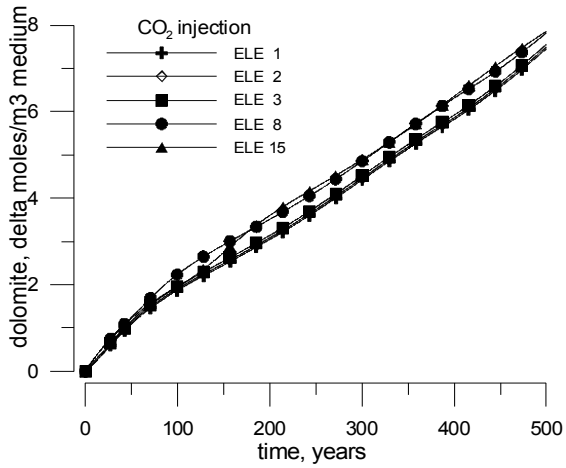


*Figure 51 – Variation of dolomite abundance (delta moles per m3 medium) vs. time for selected grid blocks (1D model, 500 years simulation).*

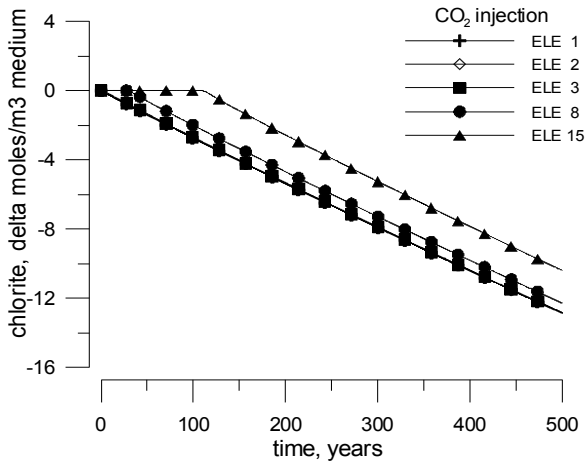


*Figure 52 – Variation of chlorite abundance (delta moles per m3 medium) vs. time for selected grid blocks (1D model, 500 years simulation).*

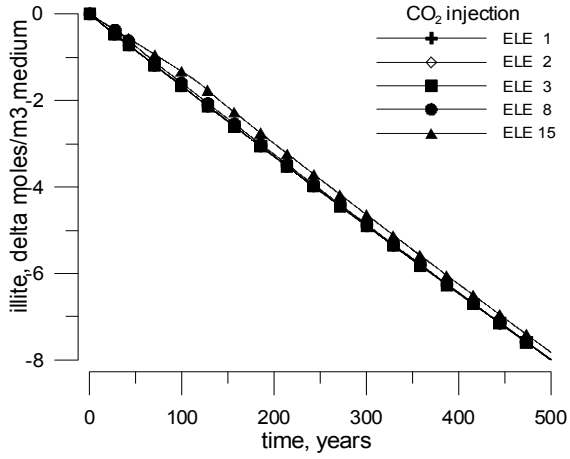


*Figure 53 – Variation of illite abundance (delta moles per m3 medium) vs. time for selected grid blocks (1D model, 500 years simulation).*

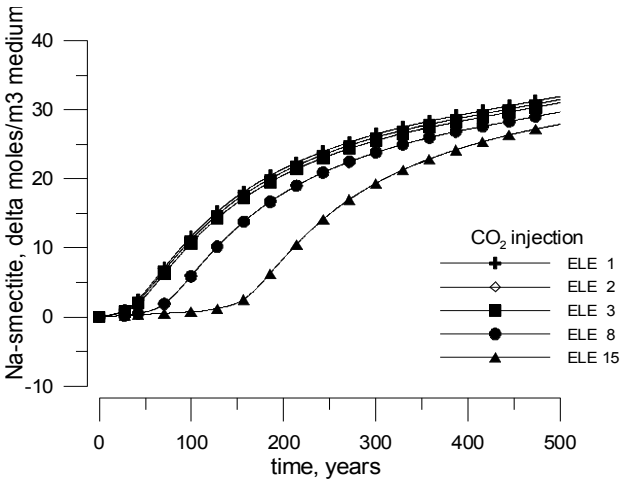


*Figure 54 – Variation of Na-smectite abundance (delta moles per m3 medium) vs. time for selected grid blocks (1D model, 500 years simulation).*

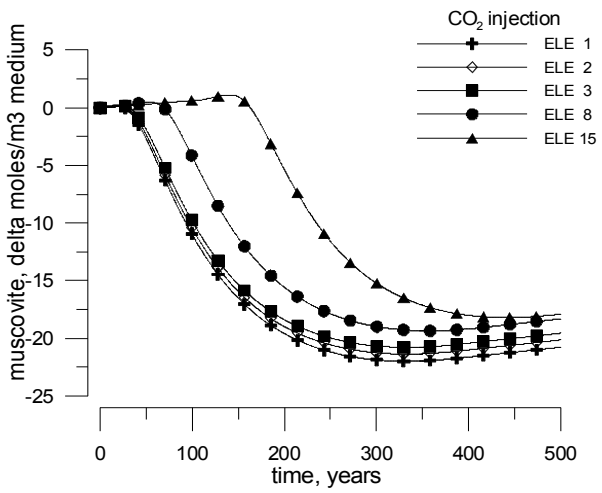


*Figure 55 – Variation of muscovite abundance (delta moles per m3 medium) vs. time for selected grid blocks (1D model, 500 years simulation).*

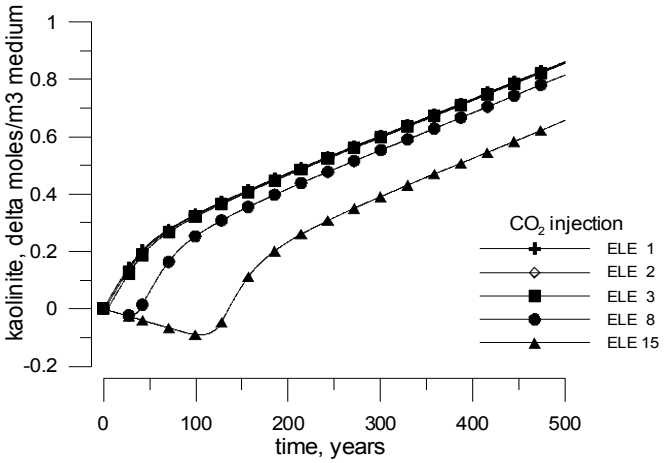


*Figure 56 – Variation of kaolinite abundance (delta moles per m3 medium) vs. time for selected grid blocks (1D model, 500 years simulation).*

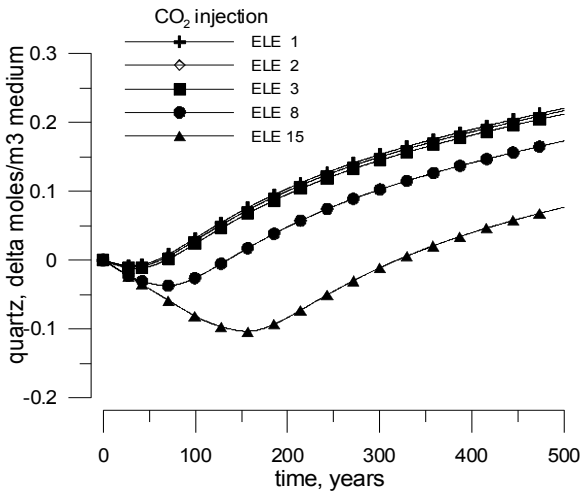


*Figure 57 – Variation of quartz abundance (delta moles per m3 medium) vs. time for selected grid blocks (1D model, 500 years simulation).*

On the basis of the medium-term 1D simulation results, a chemical characterization of the reactive mechanisms induced by $CO_2$ penetration in the caprock is obtained. The following overall reactions, which account for the major concentration changes occurring in both the aqueous and solid phases, can be tentatively written:

Muscovite + 0.4784 Calcite + 0.08529 Chlorite + 1.454 $CO_2(g)$ + 1.198 $H_2O$ + 1.957 $Na^+$ →
0.8201 Na-Smectite + 1.719 Dawsonite + 0.2132 Siderite + $K^+$ + 0.4784 $Ca^{+2}$ [1.a]

Muscovite + 2.309 Calcite + 9.455 Illite + 6.345 $CO_2(g)$ + 7.291 $H_2O$ + 11.29 $Na^+$ →
9.091 Na-Smectite + 8.655 Dawsonite + 6.673 $K^+$ + 2.309 $Ca^{+2}$ [1.b]

Illite + 0.55 Calcite + 0.55 $CO_2(g)$ + 1.3 $H_2O$ + 3 $Fe^{+2}$ →
0.1214 Dolomite + 1.2 Quartz + 1.15 Kaolinite + 0.4286 Ankerite + 0.6 $K^+$ [1.c]

Even if not stoichiometrically representative of processes effectively occurring within the caprock, these equations have the main advantage to completely represent the main mineralogical transformations. They explain the progressive increase of $Ca_{TOT}$ (Figure 58) and $K_{TOT}$ (Figure 59) aqueous concentrations observed at the end of the simulation, and also the eventual decline of the maximum $Fe_{TOT}$ amounts originally derived from chlorite and illite dissolution (Figure 60). Accordingly, such reactions are proposed here to synthesize in a compact form the complex multicomponent and multiphase reactive processes effectively occurring in the caprock due to $CO_2(g)$ injection. Their validity is supported by inspection of thermodynamic concentrations, which indicate the energetic feasibility of the processes where high $P_{CO2}$-values occur.

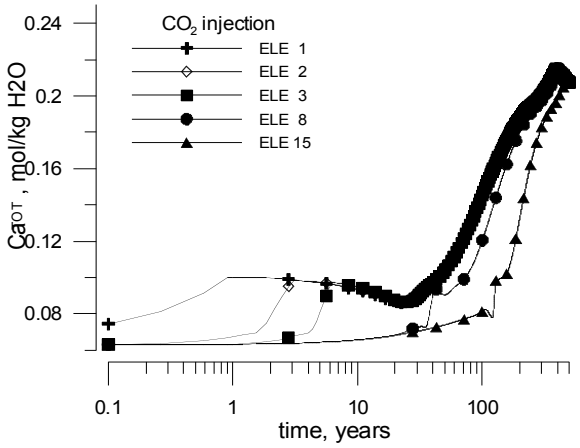


*Figure 58 – Variation of $Ca_{TOT}$ concentration (delta moles per m3 medium) vs. time for selected grid blocks (1D model, 500 years simulation).*

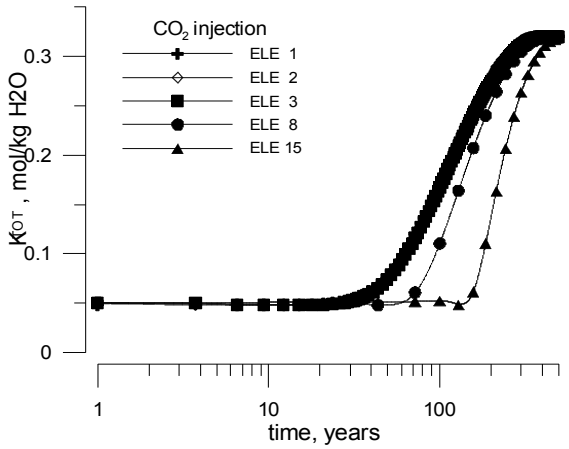


*Figure 59 – Variation of $K_{TOT}$ concentration (delta moles per m3 medium) vs. time for selected grid blocks (1D model, 500 years simulation).*

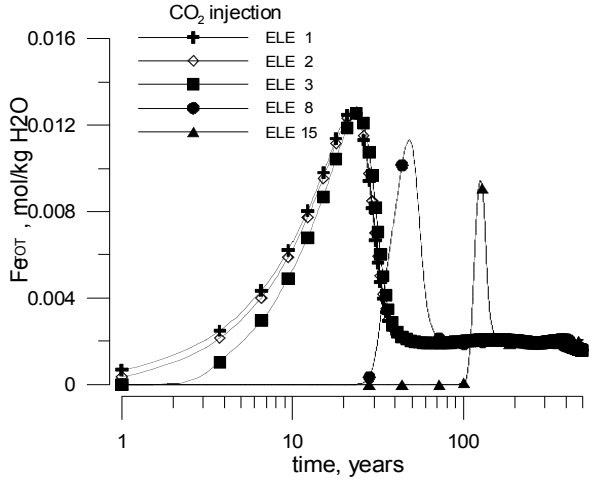


*Figure 60 – Variation of $Fe_{TOT}$ concentration (delta moles per m3 medium) vs. time for selected grid blocks (1D model, 500 years simulation).*

## 7.3. Fractured caprock: 2D simulations

### 7.3.1. Short-term behavior

With the aim of evaluating the effect of $CO_2$ leakage from the reservoir on the mineralogical stability of a fractured caprock, a 2D model has been set up which accounts for gas phase participation in reaction and transport, and chemical interactions between fractures and matrix.

The model considers an idealized fractured rock with a set of plane, parallel vertical fracture zones (faults or, more generally, zones of increased permeability and porosity) of equal aperture (0.1 m) and spacing (3.86 m). Because of symmetry of this fractured rock, only part of the matrix needs to be modeled (Figure 61).

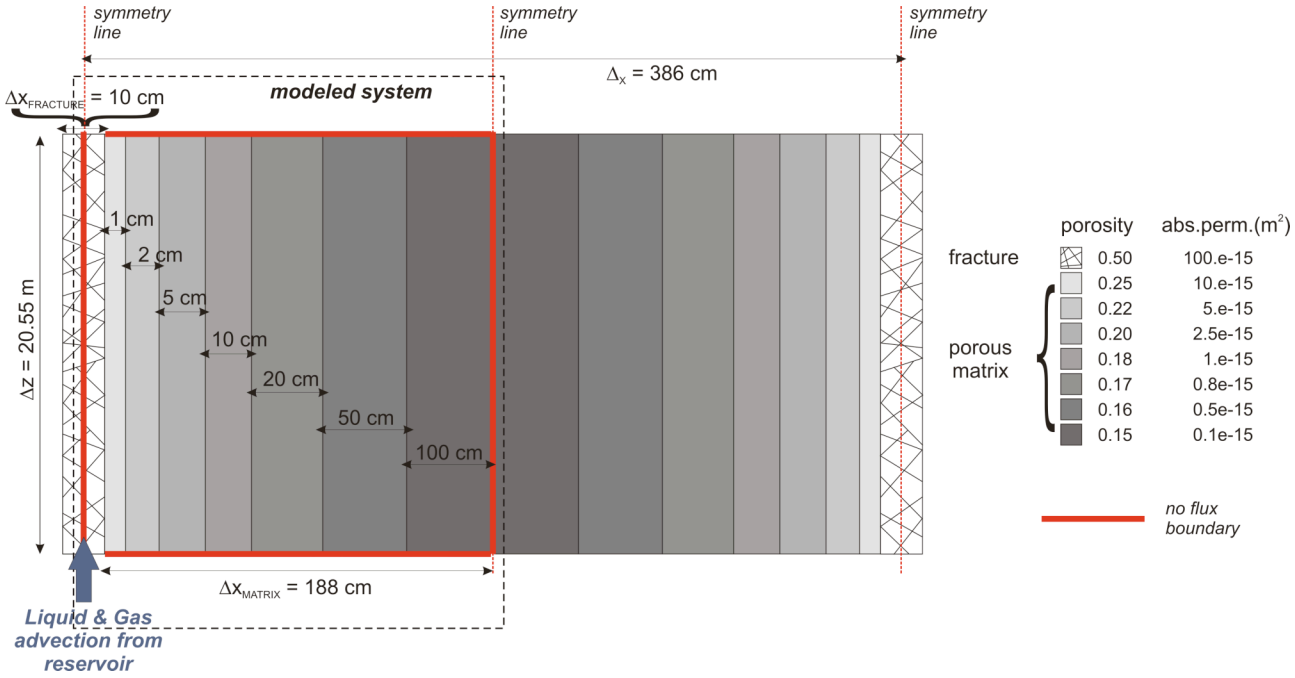


*Figure 61 – Vertical 2D section model for $CO_2$ leakage into a fractured caprock. Details on porosity and permeability distribution are also given.*

The model simulates a vertical fracture 20.6 m long extending from the top of the reservoir into the caprock matrix. The rock matrix is further discretized laterally into 7 zones with porosity and permeability decreasing away from the fracture.

More details on grid geometry and other parameters used in the simulation are given in Table 16. Fine gridding specifications were chosen in order to investigate the detail of chemical processes occurring within and in proximity to the fracture domain.

Isothermal conditions were assumed and the temperature is fixed at 45°C in all rock domains. Vertical distribution of the pressure in the fracture and matrix domains follows a hydrostatic gradient calculated by constraining the pressure at the bottom of the column to 105 bar.

The reservoir is modeled as a large volume containing a two-phase mixture of water (70 % by volume) and $CO_2$ (30 % by volume), that is connected to the fracture domain. The simulation has been carried out with reservoir pressure fixed at 107 bar. The resulting 2 bar overpressure in the reservoir induces significant advection into the overlying elements of the fracture domain (the darcian liquid velocity at the bottom of the column is initially equal to 1.39e-5 m/sec = 439 m/yr), so that chemical transport and reaction are controlled by advection in the fracture, and by a complex interplay between advection and molecular diffusion at the interface between fracture and matrix, and within the matrix.

*Table 16 – Grid specifications and other parameters used for 2D problem*

| Parameters | lateral spacing (m) | permeability ($m^2$) (isotropic) | porosity |
|---|---|---|---|
| Rock domain: caprock | | | |
| Fracture | 0.05 | 100.e-15 | 0.500 |
| Matrix A | 0.01 | 10.e-15 | 0.250 |
| Matrix B | 0.02 | 5.e-15 | 0.220 |
| Matrix C | 0.05 | 2.5e-15 | 0.200 |
| Matrix D | 0.10 | 1.e-15 | 0.180 |
| Matrix E | 0.20 | 0.8e-15 | 0.170 |
| Matrix F | 0.50 | 0.5e-15 | 0.160 |
| Matrix G | 1.00 | 0.1e-15 | 0.150 |

| Parameters | volume ($m^3$) | permeability ($m^2$) | porosity |
|---|---|---|---|
| Rock domain: reservoir | | | |
| Reservoir | 1.e+30 | 400.e-15 | 0.325 |

| Parameters | vertical spacing (m) (from top to the bottom) | number of layers |
|---|---|---|
| Rock domain: caprock | | |
| Layer 7 | 2.00 | 9 |
| Layer 6 | 1.00 | 1 |
| Layer 5 | 0.75 | 1 |
| Layer 4 | 0.50 | 1 |
| Layer 3 | 0.20 | 1 |
| Layer 2 | 0.10 | 1 |
| Layer 1 | 0.05 | 1 |

A large grid block was specified at the top of the fracture domain in order to maintain constant pressure there and allow the flow to escape through the upper interface of the fracture domain. In this way, any physical boundary effect possibly interfering with the geochemical calculations in this part of the system has been avoided.

The fine grid utilized in the simulation requires a large computational effort. As the main objective of this first simulation was obtaining accurate results, maximum simulation time was limited to 10 years to obtain reasonable computing times.

Some of the most important results are described in the following Figures 62 and 63, where contour plots for gas saturation, pH, porosity and calcite volume fraction change are given after 10 years simulation.

The main observations are as follows:

1) high gas saturation values preferentially develop along the fracture, where higher porosity and permeability also occur; the propagation of the gas phase into the matrix primarily occurs along a direction perpendicular to the fracture axis, according to the porosity-permeability gradient of the matrix;

2) major changes in porosity occur in the fracture and in the matrix elements adjacent to the fracture;

3) the acid front propagates quite rapidly into the matrix, and after 10 years of simulation, the isoactivity line at pH = 5 is more than 1.5 m away from the fracture near the bottom of the matrix; at this time, the pH of the aqueous solution is lower than 5 all along the fracture;

4) calcite behavior is quite complex, and the changes in abundance of this mineral are inversely correlated to the porosity variations already described; this pattern is discussed below.

The complex pattern of calcite can be explained as follows. A sharp increase of volume fraction is observed in the first, small element of the fracture domain. Again, as in the case of 1D simulations previously discussed, the $Ca_{TOT}$ and $HCO_{3,TOT}$ mass transport occurring (in this case predominantly by advection) from the reservoir into the caprock, controls the geochemical evolution at the reservoir-caprock interface, inducing significant precipitation of calcite in the first element of the caprock. The contrasting effect of increasing acidity is overwhelmed by a stronger increase in $[Ca^{+2}]$ and $[HCO_3^-]$, which moves to the right the equilibrium of the following reaction:

$Ca^{+2} + HCO_3^- \rightarrow$ Calcite + $H^+$.

Due to calcite precipitation, porosity decreases up to -5% near the reservoir–caprock interface.

A reversal of this pattern is observed in the upper part of the fracture domain, where calcite becomes undersaturated and starts to dissolve, due to the less effective transport of reactive $Ca_{TOT}$ and $HCO_{3,TOT}$ components (already removed from the upwards migrating aqueous solution by calcite precipitation) with respect to $[H^+]$ (pH < 5 in the entire fracture). The related porosity enhancement is about +4%.

Finally, the presence of a zone of calcite precipitation (and porosity decrease) throughout the matrix, along a direction parallel to the fracture and at about 20-30 cm from its axis, reveals that a complex interplay between molecular diffusion in aqueous phase and mass flow advection controls the chemical beahvior of the matrix near the fracture. In particular, high $Ca_{TOT}$ and $HCO_{3,TOT}$ concentrations related to both the advancement of reservoir fluids into the fracture, and to the dissolution of calcite in upper part of the fracture, move away from the fracture and give rise to a reactive front which propagates through the matrix. This reactive front is primarily characterized by calcite precipitation.

To further confirm this dynamics, a detailed inspection of capillary pressure and spatial distribution of liquid velocity (Figure 64) reveals that liquid flow mainly occurs in a vertical direction and mostly in the fracture, according to initial pressure gradient and porosity-permeability distribution.
Liquid (darcian) velocities are generally more than one order of magnitude smaller in the matrix than in the fracture. Some lateral advection is seen to occur near the bottom and the top of the matrix.

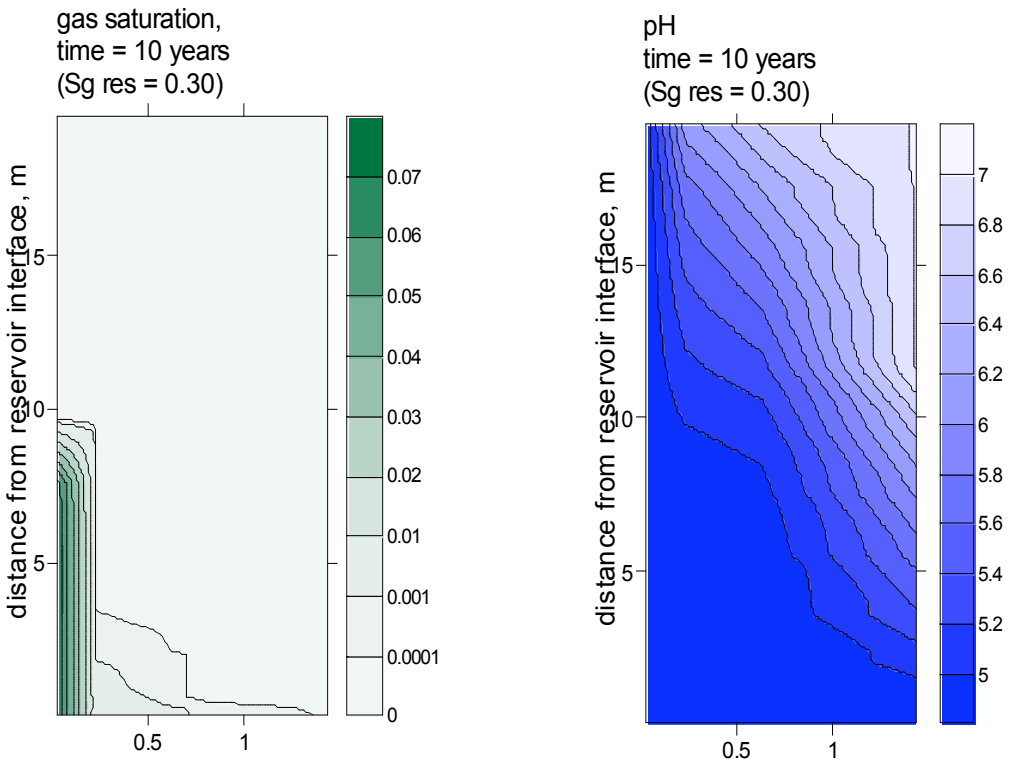


*Figure 62 – Contour plot showing gas saturation (Sg) distribution and pH spatial variation after 10 years simulation (initial reservoir gas saturation, Sg = 0.3)*

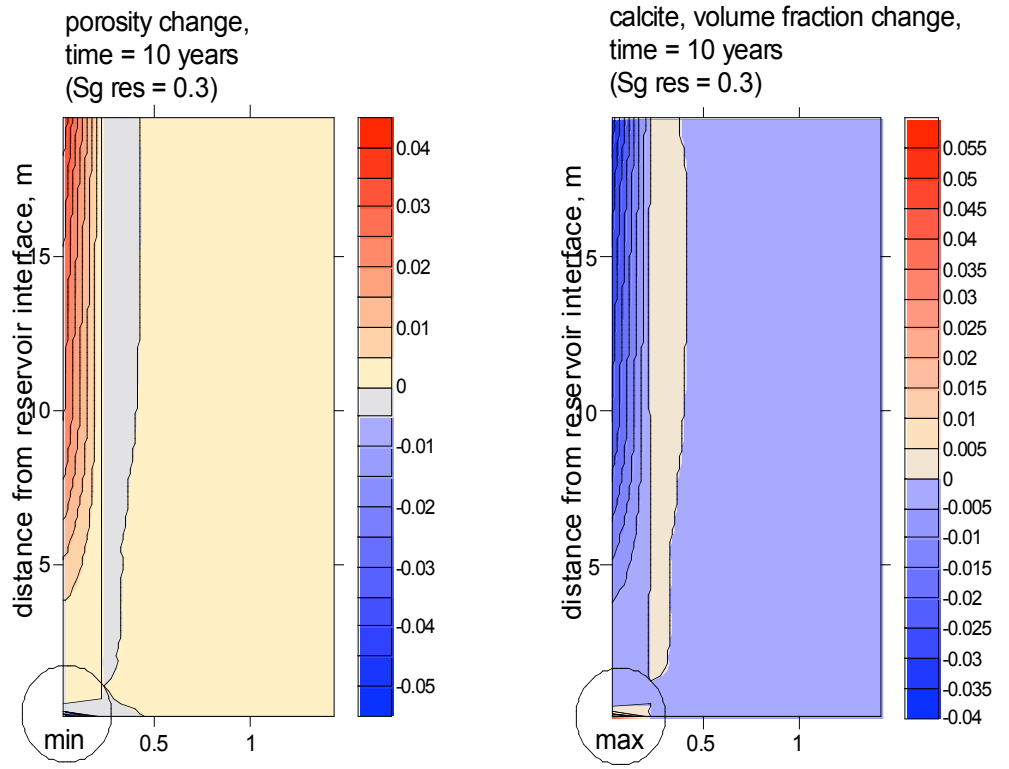


*Figure 63 – Contour plot showing porosity and calcite volume fraction change after 10 years simulation (initial reservoir gas saturation, Sg = 0.3)*

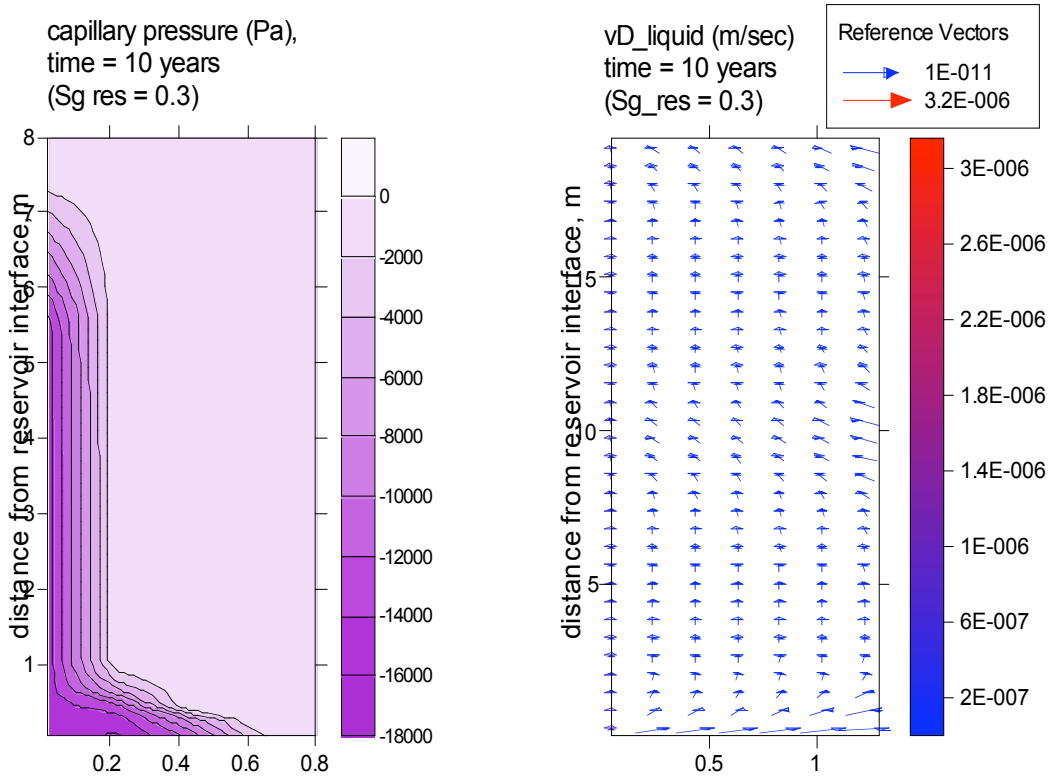


*Figure 64 – Contour plot showing capillary pressure (in Pa) distribution and darcian liquid velocity field (m/sec) after 10 years simulation (initial reservoir gas saturation, Sg = 0.3)*

The geochemical evolution of the entire fracture-matrix system is then governed by two concomitant processes: advection in the fracture on the one hand, and related diffusion plus minor advection into the matrix on the other.

Further insight into fracture-matrix interactions can be gained by inspection of the spatial distribution of aqueous component concentrations and changes in volume fractions of minerals. The patterns of some of the most relevant species are shown in Figures 65 to 71. All these graphs refer to 10 years simulation time.

The main observations are:

1) apart from calcite dissolution, no other major mineralogical transformations occur within the system; the changes in abundance of other minerals are small and are of interest only with respect to the description of the reaction mechanisms;

2) with this premise in mind, the most significant dissolution/precipitation reactions could be considered those involving muscovite, chlorite and illite; contour plots for these minerals indicate that flow through the fracture induces chlorite, illite and muscovite dissolution near the reservoir-caprock interface, where two-phase conditions and high-$P_{CO2}$ values occur; in contrast with illite, which dissolves throughout the system; muscovite and chlorite show a more complex pattern, because they tend to precipitate within the matrix as well as near the top boundary, in proximity to the fracture;

3) kaolinite participates in multiphase reactions, precipitating where $CO_2$(gas) is present, and dissolving in the inner part of the matrix, where muscovite and chlorite are stable;

4) clay minerals are reactive as seen by the precipitation of Na-smectite (in relatively significant amounts) and Ca-smectite (negligible amounts), which exclusively occurs at the bottom of the matrix and in proximity to the fracture;

5) dolomite, and to a lesser extent dawsonite, ankerite, siderite and pyrite are by-products of $CO_2$-rich front advancement into the matrix, and of migration of aqueous species like $Mg^{+2}$, $SO_4^{-2}$ and $Fe^{+2}$ other than $C_{TOT}$ in the matrix;

6) quartz tends to precipitate in close proximity to the reservoir-fracture interface, and dissolves in the matrix;

7) inspection of aqueous species behavior reveals that the propagation of the (prevalently) diffusive front into the matrix can be efficiently traced by plotting the concentration of non-reactive tracers like $I^-$ or He(aq); species like $Ca^{+2}$, $K^+$ and $SO_4^{-2}$ show similar patterns as the non-reactive tracers: they are mainly controlled by diffusive transport, and are only partially affected by source/sink effects tied to mineral precipitation/dissolution; in contrast, the $HCO_3^-$ profile is directly correlated with the advancement of the gas front, which is traced by the value of the gas saturation parameter; the spatial distribution of $Na^+$ concentration reflects the occurrence of a sort of “back-diffusion” process from matrix towards fracture, this process being induced by the higher $Na^+$ initial concentration in the caprock with respect to the reservoir;

8) finally, the contour lines of $Fe^{+2}$ indicate that the concentration of this species is not governed by transport processes in the aqueous phase, but is primarily determined by sink/source effects related to the dissolution of minerals like chlorite and the precipitation of ankerite, siderite and pyrite.

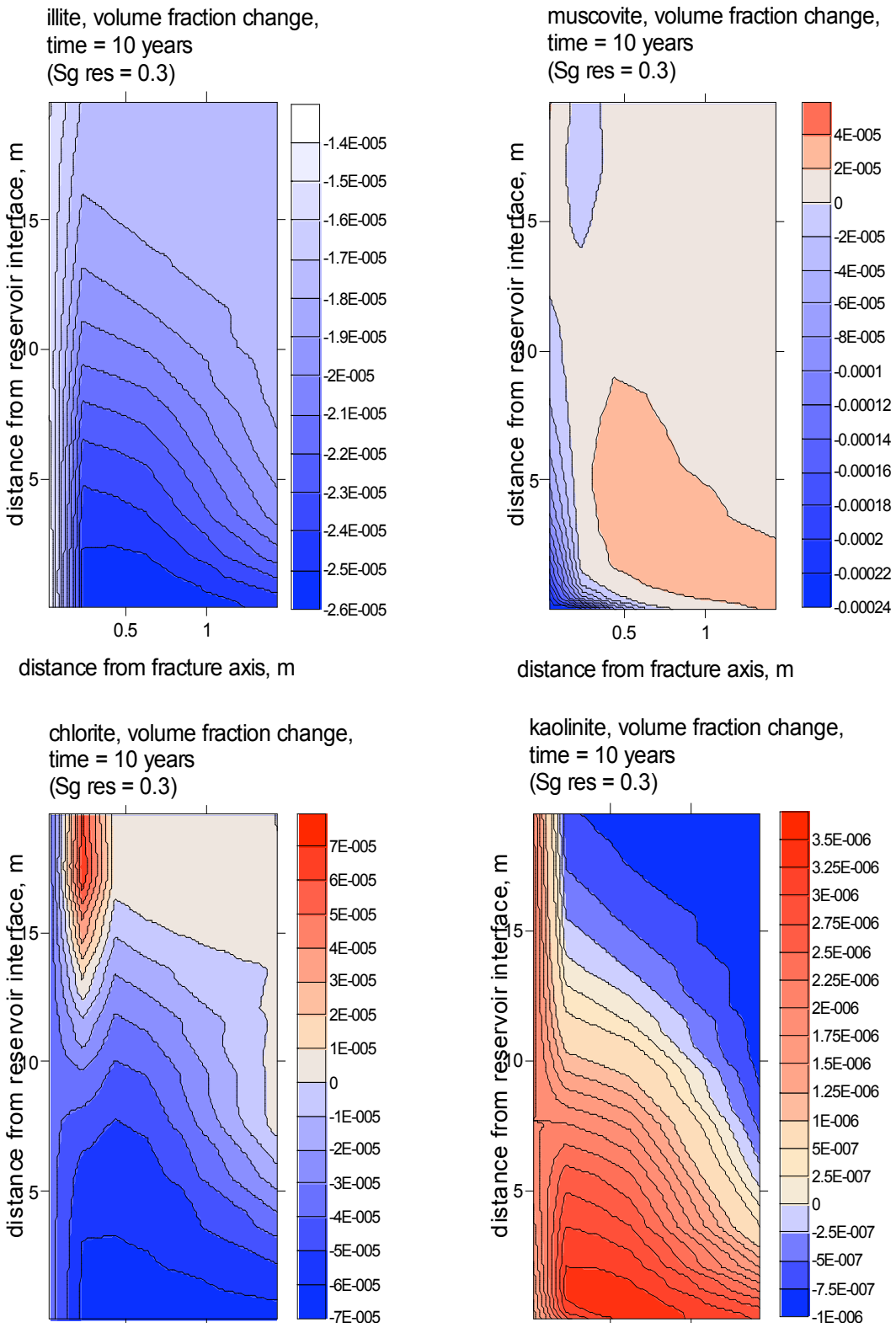


*Figure 65 – Contour plot showing the spatial volume fraction changes of illite, muscovite, chlorite and kaolinite after 10 years simulation*

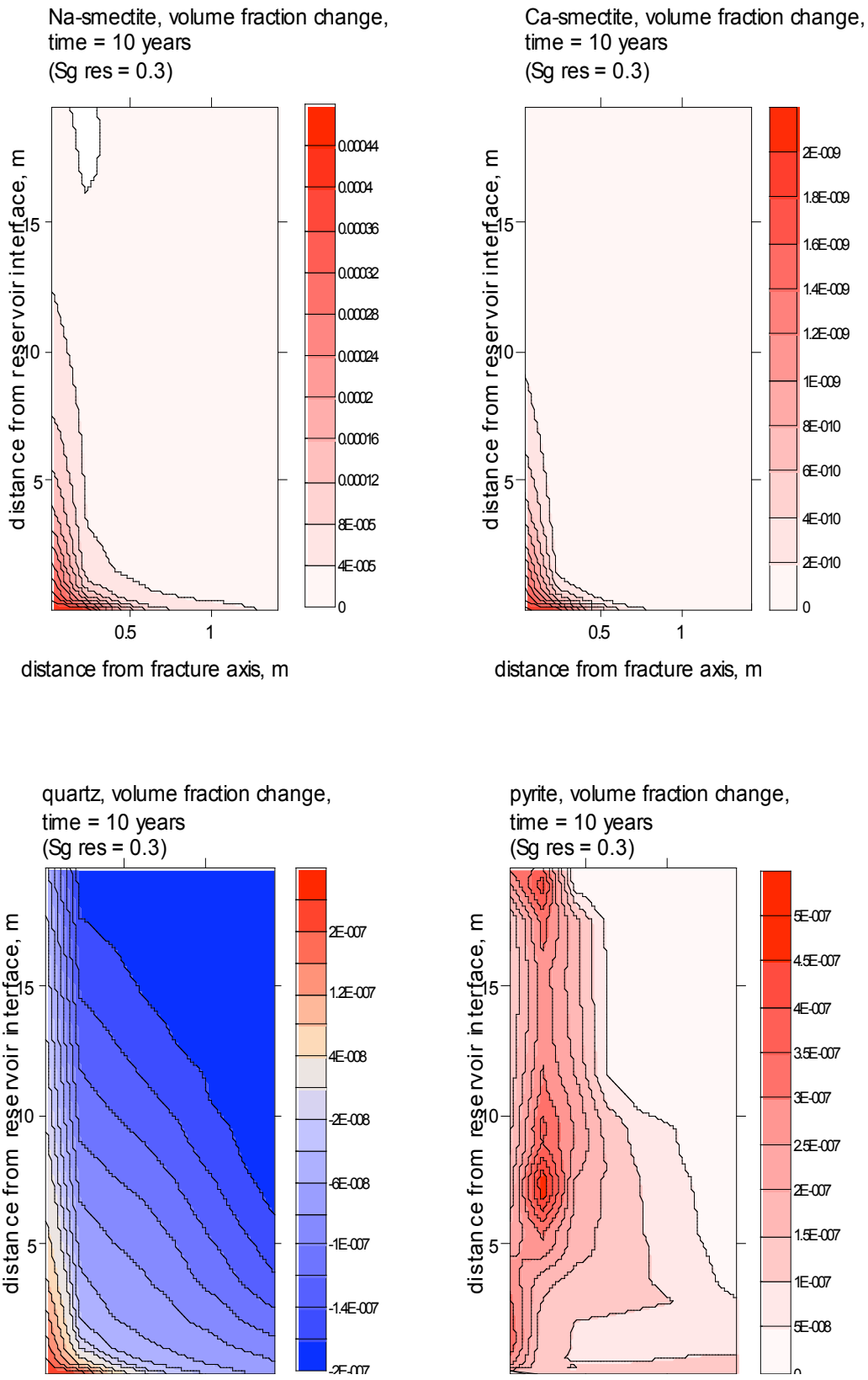


*Figure 66 – Contour plot showing the spatial volume fraction changes of Na-smectite, Ca-smectite, quartz and pyrite after 10 years simulation*

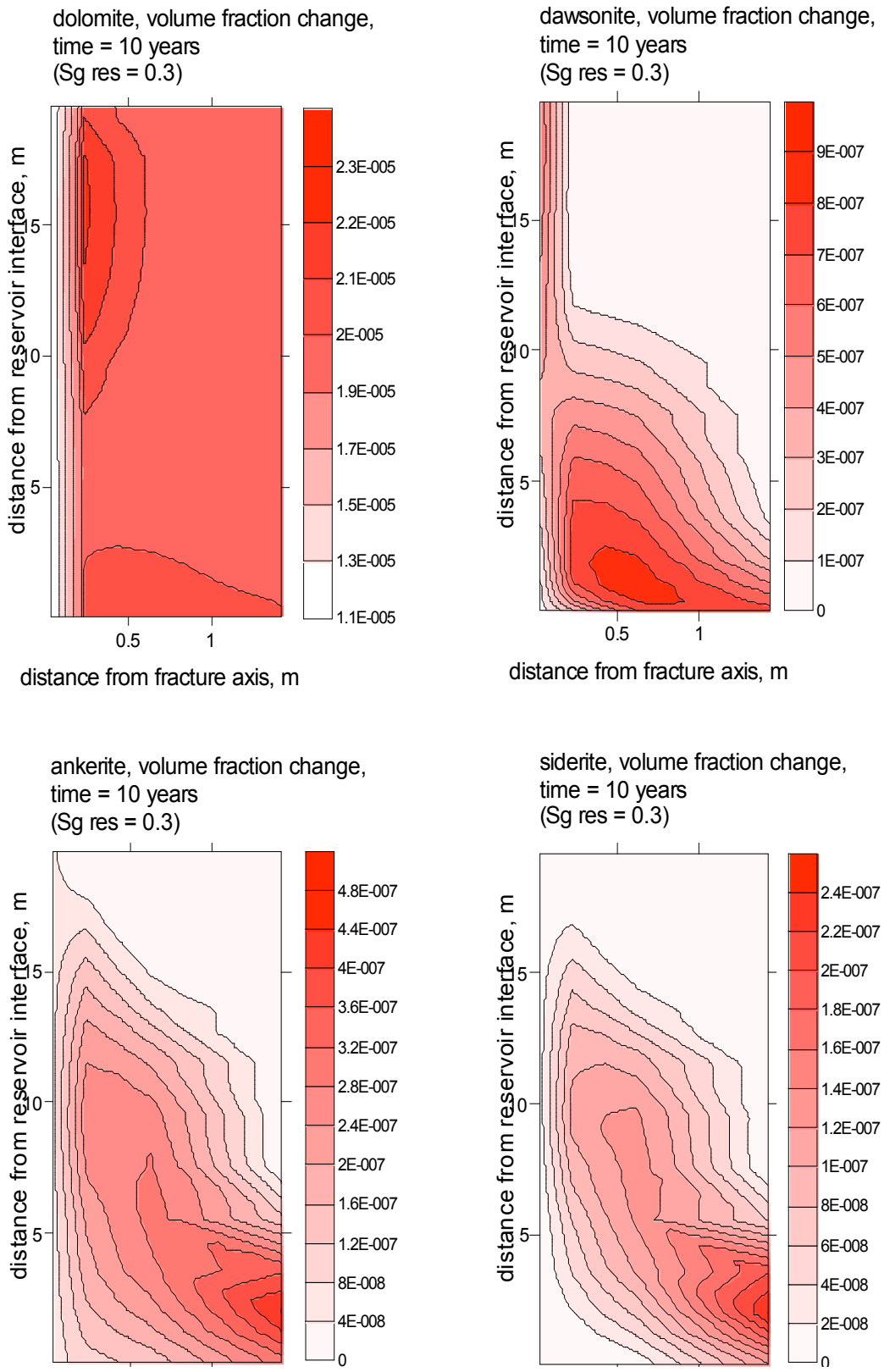


*Figure 67 – Contour plot showing the spatial volume fraction changes of dolomite, dawsonite, ankerite and siderite after 10 years simulation*

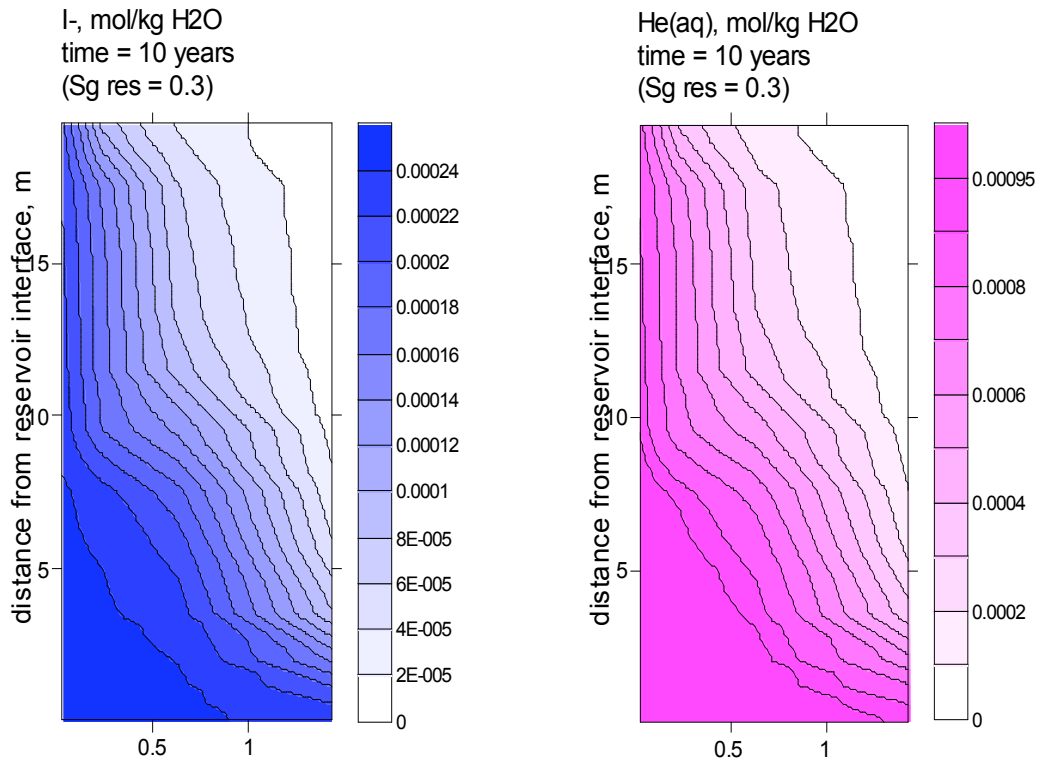


*Figure 68 – Contour plot showing the spatial concentration of inert tracers ($I^-$ and He,aq) after 10 years simulation*

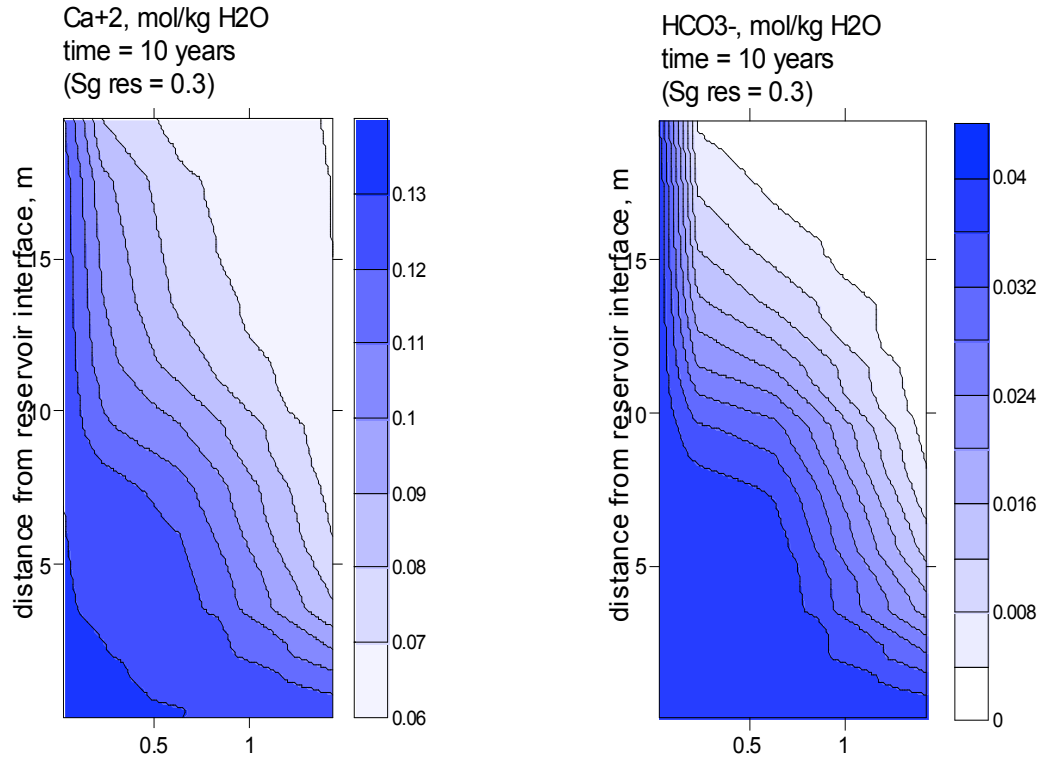


*Figure 69 – Contour plot showing the spatial concentration of $Ca^{+2}$ and $HCO_3^-$ after 10 years simulation*

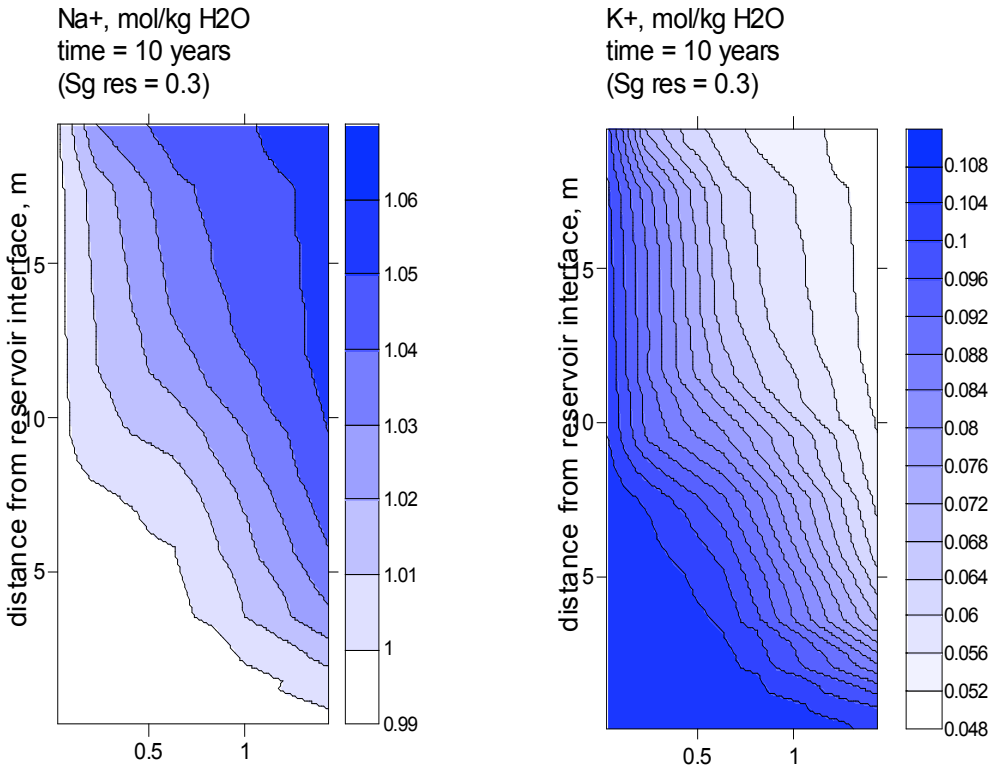


*Figure 70 – Contour plot showing the spatial concentration of $Na^{+}$ and $K^{+}$ after 10 years simulation*

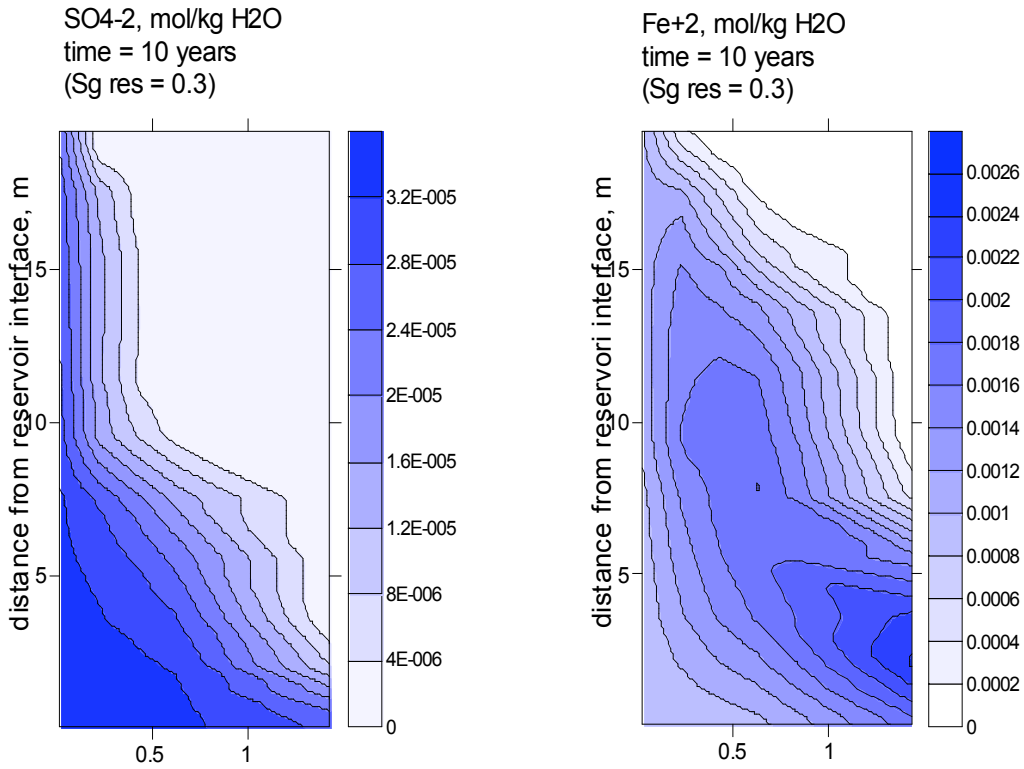


*Figure 71 – Contour plot showing the spatial concentration of $SO_4^{-2}$ and $Fe^{+2}$ after 10 years simulation*

### 7.3.2. Medium-term and maximum risk scenario

As in the case of 1D simulations, the maximum risk scenario for the fractured caprock model is obtained by maximizing the participation of gaseous $CO_2$ in water-rock interactions. This has been accomplished by increasing the initial reservoir gas saturation to Sg = 0.99. By setting appropriate initial pressure values in the different domains of the system (first step: global gravity equilibration, second step: application of a constant overpressure at the fracture bottom, +2 bar), the $CO_2$ initially stored in the reservoir is forced to first invade the fracture, and subsequently to enter the rock matrix.

Because larger simulation times were desired ($time_{MAX}$ = 500 years), a coarser grid has been utilized ($\Delta z_{MIN}$ = 5 cm) to reduce the computational work of the simulation. Another major change concerns the use of a constant pressure boundary at the rightmost boundary of the matrix domain. By setting the boundary pressure slightly below the value of the adjacent matrix column, fluids from the matrix are allowed to freely discharge away from the fracture. This model conceptualizes the behavior of a semi-infinite matrix layer which extends perpendicularly to fracture axis.

The value of boundary pressure is critical in controlling liquid flow when two-phase conditions develop in the matrix, due to the competing action of capillary forces associated with the gas front advancement. After sensitivity analysis, the results for the -0.1 bar case are presented, because the short term (first 50 years simulation) distribution of the darcian velocities (Figures 72 and 73) reveals the presence of an effective slow, uniform liquid discharge ($v_{D,LIQUID}$ lower than 1e-13 m/sec) all along the constant pressure boundary.

The dimensions of the porous matrix have been increased, and the maximum lateral extension of the caprock domain now reaches 12.58 m. The vertical extension of the domain is 20.55 m. More details on grid specifications and system geometry are given in Figure 74 and in Table 17.

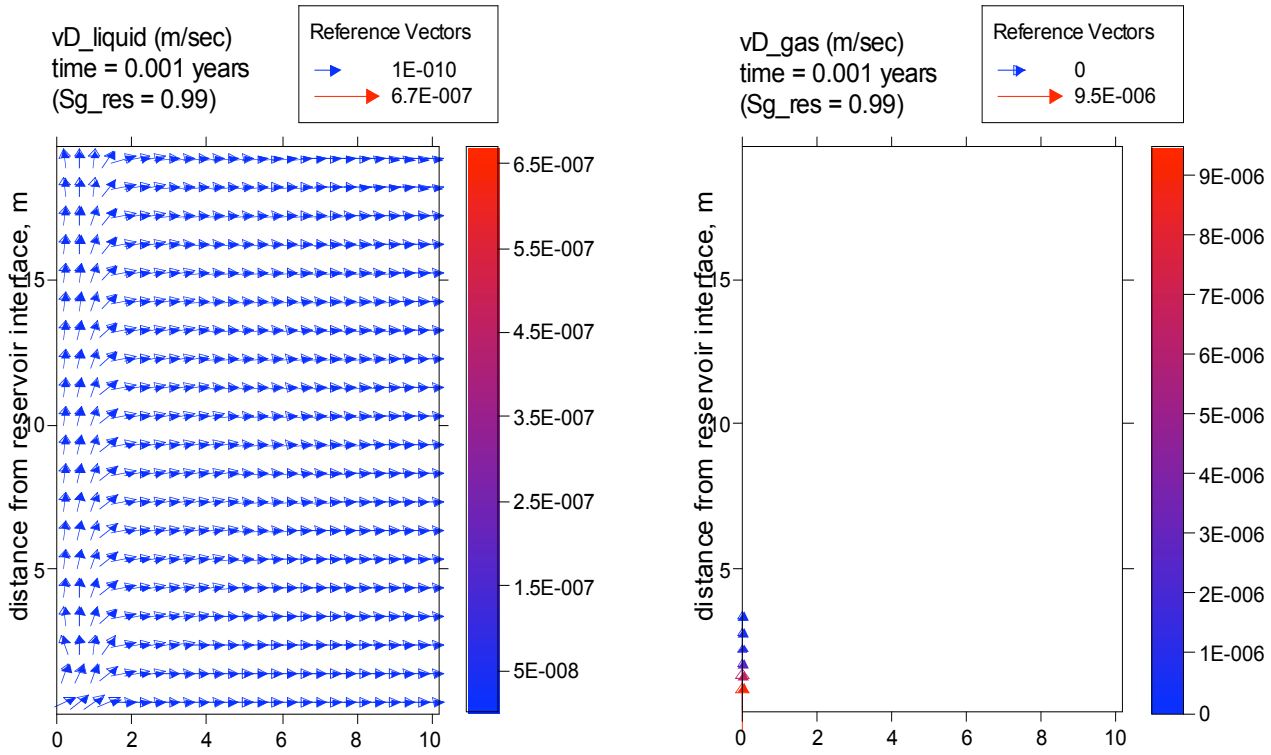


*Figure 72 – Contour plots showing liquid and gas darcian velocity fields (m/sec) after 0.001 years simulation (initial reservoir gas saturation, Sg = 0.99)*

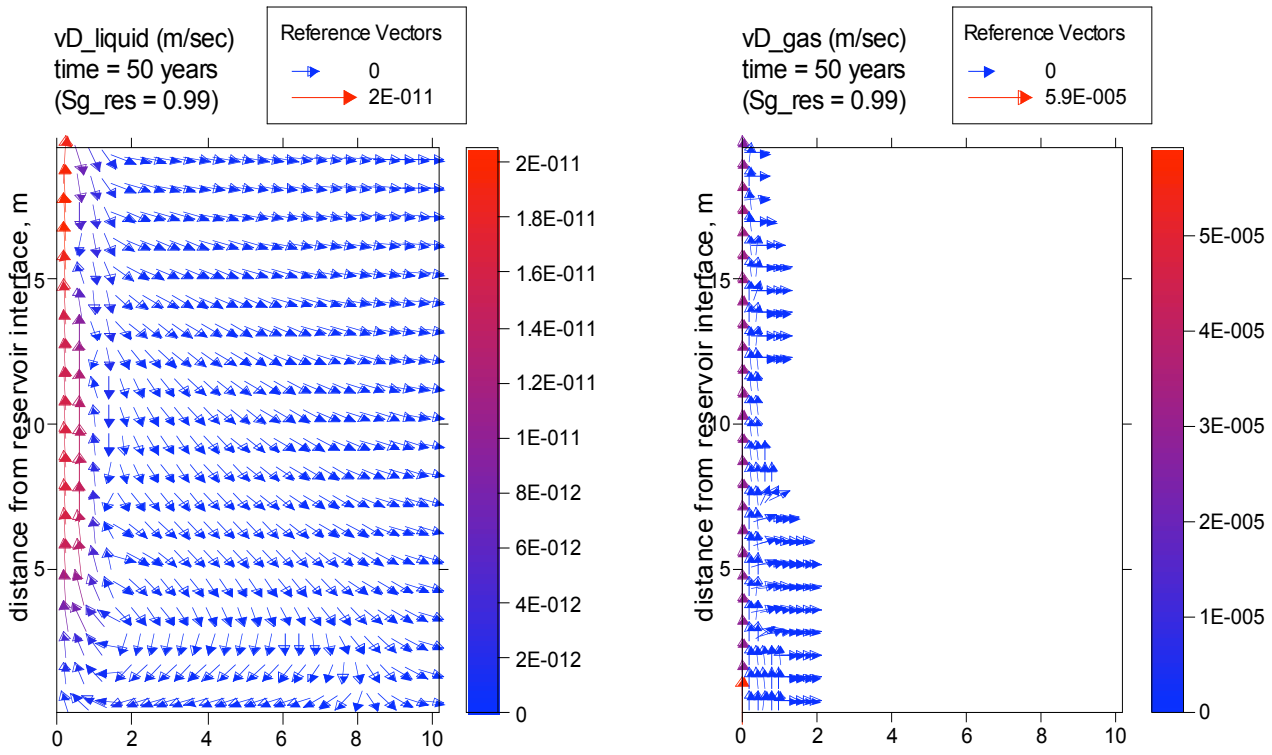


*Figure 73 – Contour plots showing liquid and gas darcian velocity fields (m/sec) after 50 years simulation (initial reservoir gas saturation, Sg = 0.99)*

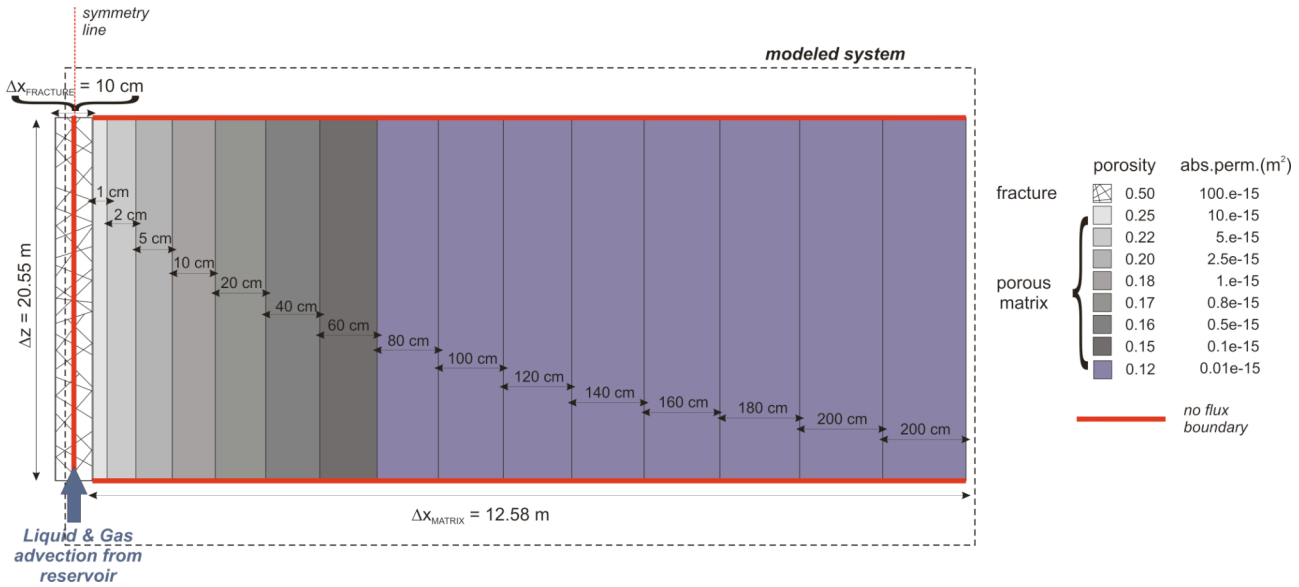


*Figure 74 – Vertical 2D section model for $CO_2$ leakage into a fractured caprock (500 years simulation). Details on porosity and permeability distribution are also given.*

*Table 17 – Grid specifications and other parameters used for 2D problem (500 years simulation)*

| Parameters | lateral spacing (m) | permeability ($m^2$) (isotropic) | porosity |
|---|---|---|---|
| Rock domain: caprock | | | |
| Fracture | 0.05 | 100.e-15 | 0.500 |
| Matrix A | 0.01 | 10.e-15 | 0.250 |
| Matrix B | 0.02 | 5.e-15 | 0.220 |
| Matrix C | 0.05 | 2.5e-15 | 0.200 |
| Matrix D | 0.10 | 1.e-15 | 0.180 |
| Matrix E | 0.20 | 0.8e-15 | 0.170 |
| Matrix F | 0.40 | 0.5e-15 | 0.160 |
| Matrix G | 0.60 | 0.1e-15 | 0.150 |
| Matrix H1 | 0.80 | 0.01e-15 | 0.120 |
| Matrix H2 | 1.00 | 0.01e-15 | 0.120 |
| Matrix H3 | 1.20 | 0.01e-15 | 0.120 |
| Matrix H4 | 1.40 | 0.01e-15 | 0.120 |
| Matrix H5 | 1.60 | 0.01e-15 | 0.120 |
| Matrix H6 | 1.80 | 0.01e-15 | 0.120 |
| Matrix H7 | 2.00 | 0.01e-15 | 0.120 |
| Matrix H8 | 2.00 | 0.01e-15 | 0.120 |

| Parameters | volume ($m^3$) | permeability ($m^2$) | porosity |
|---|---|---|---|
| Rock domain: reservoir | | | |
| Reservoir | 1.e+30 | 400.e-15 | 0.325 |

| Parameters | vertical spacing (m) (from top to the bottom) | number of layers |
|---|---|---|
| Rock domain: caprock | | |
| Layer 6 | 2.00 | 9 |
| Layer 5 | 1.00 | 1 |
| Layer 4 | 0.75 | 1 |
| Layer 3 | 0.50 | 1 |
| Layer 2 | 0.20 | 1 |
| Layer 1 | 0.10 | 1 |

The inspection of pressure and capillary pressure profiles of Figures 75 to 76, allows a better understanding of flow dynamics within the caprock, because the main driving forces controlling fluid displacement can be recast in terms of pressure gradients. The following observations can be made: the gas front propagates firstly in the fracture (with a maximum velocity of about 8e-5 m/sec after 500 years), and then into the matrix, following a direction perpendicular to fracture axis (up to about 1e-11 m/sec after 500 years); liquid dynamics is characterized by a preferential upward displacement along both the fracture domain and the adjacent matrix columns (with high porosity and permeability values). This has the ultimate effect to induce a sort of slow convection in the inner part of the matrix (Figure 77), and then some mixing between different waters. As deduced from these diagrams, mass transfer occurs in the matrix under control of the following concomitant mechanisms: gas advection, molecular diffusion in aqueous phase, and liquid advection.

A major effect of this dynamics is the advancement of the $CO_2$-rich gas front in the caprock. This process is traced by the presence, after 500 years simulation, of gas saturation values > 0 at about 1.75 m from fracture axis, near the bottom of the domain, and about 1.25 m in the middle and at the top of domain (Figure 78). At the same simulation time, pH pattern roughly follows the gas saturation pattern, only differing from it for a more uniform advancement of the pH-acid front along the direction perpendicular to fracture axis. pH contour lines are almost exactly aligned in a vertical direction, and minor deviations are shown for the lower values only, as e.g.for the pH = 5 isoactivity line which is at 0.8 and 1.2 m from fracture axis in the upper and lower part of the domain, respectively (Figure 78).

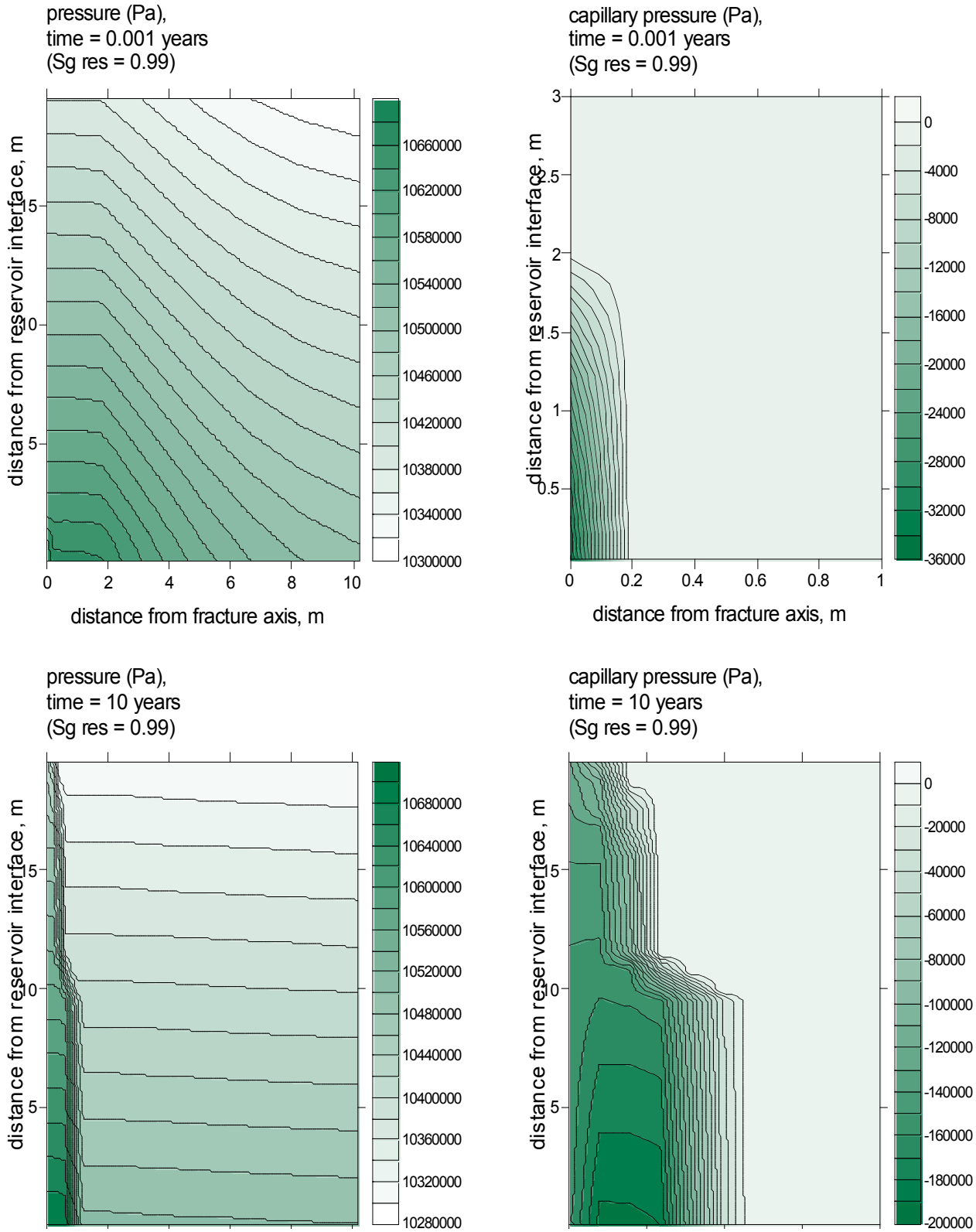


*Figure 75 – Contour plots showing capillary pressure and absolute pressure (in Pa) distribution after 0.001 and 10 years simulation (initial reservoir gas saturation, Sg = 0.99)*

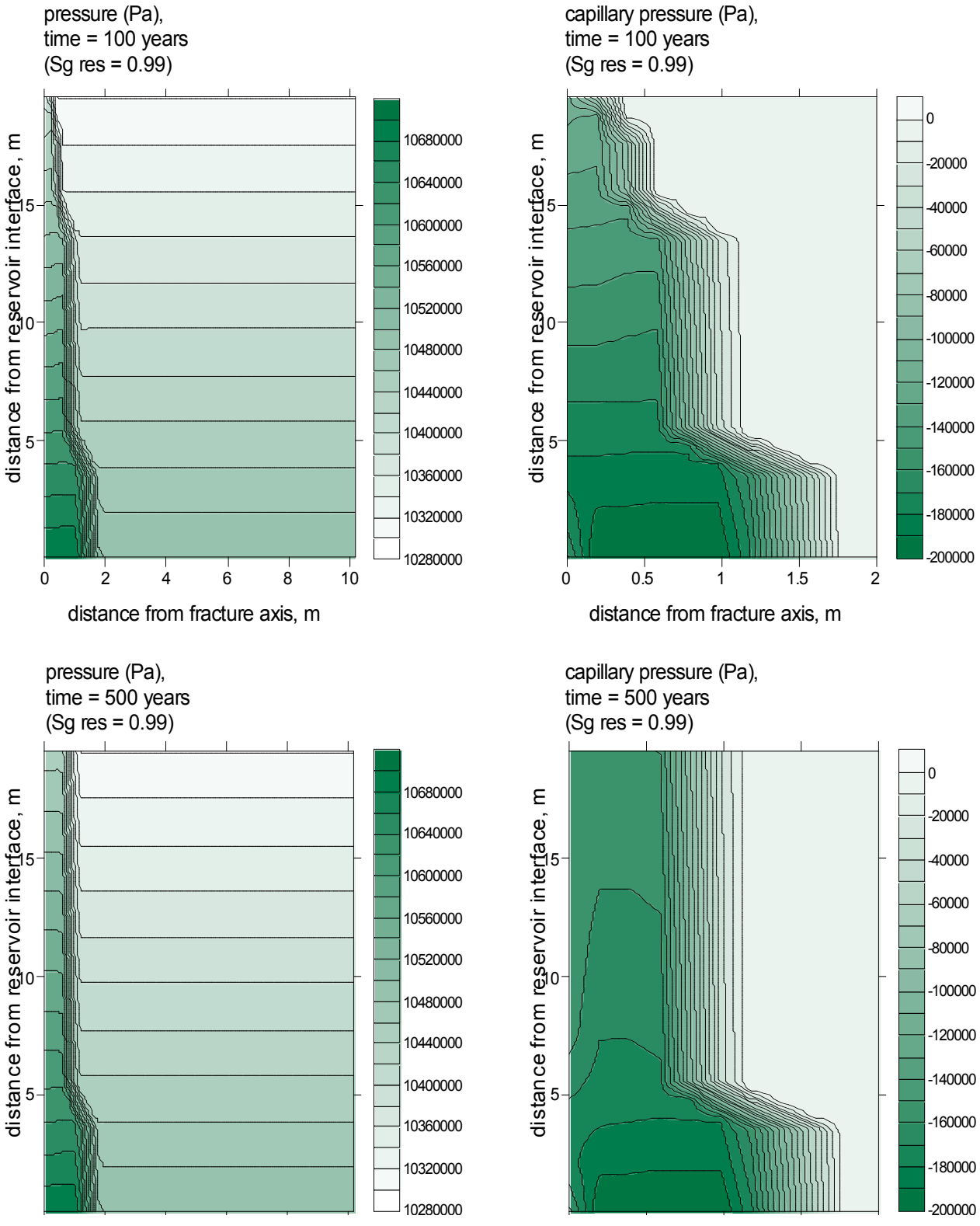


*Figure 76– Contour plots showing capillary pressure and absolute pressure (in Pa) distribution after 100 and 500 years simulation (initial reservoir gas saturation, Sg = 0.99)*

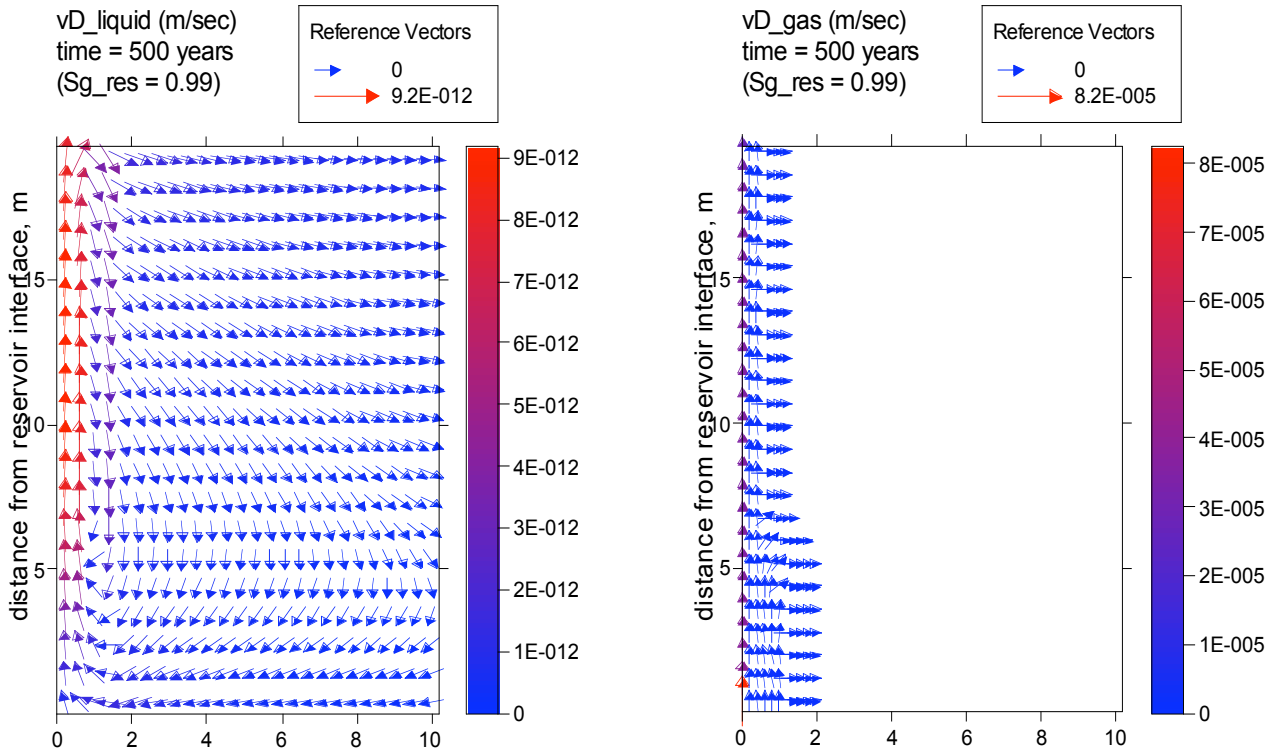


*Figure 77 – Contour plots showing liquid and gas darcian velocity fields (m/sec) after 500 years simulation (initial reservoir gas saturation, Sg = 0.99)*

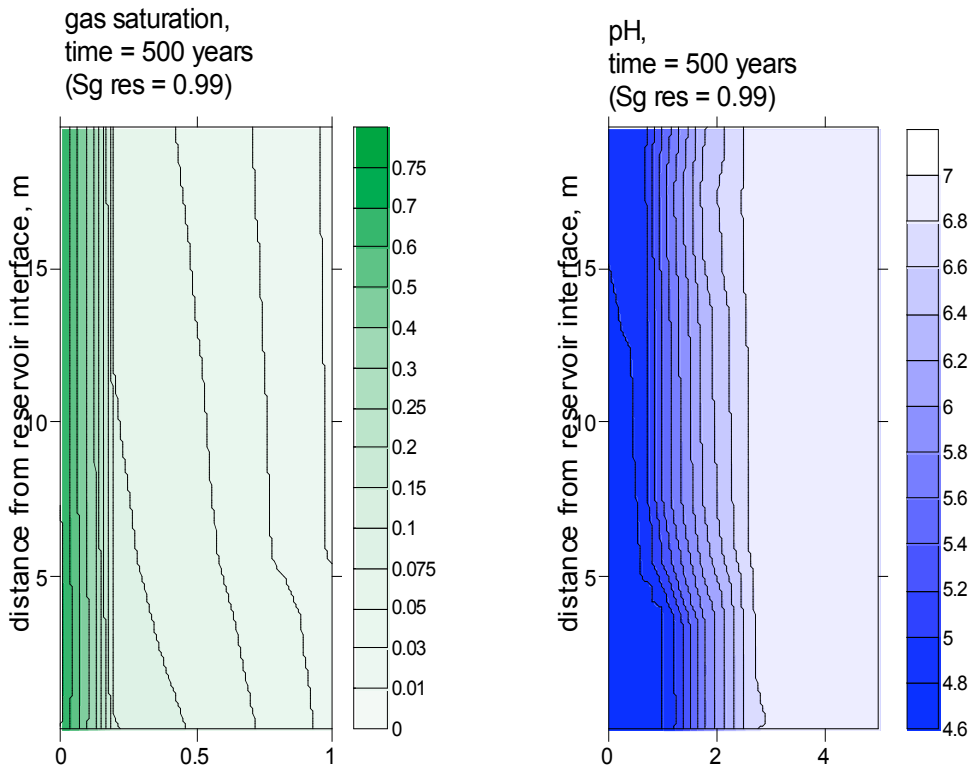


*Figure 78 – Contour plots showing gas saturation and pH spatial distribution after 500 years simulation (initial reservoir gas saturation, Sg = 0.99)*

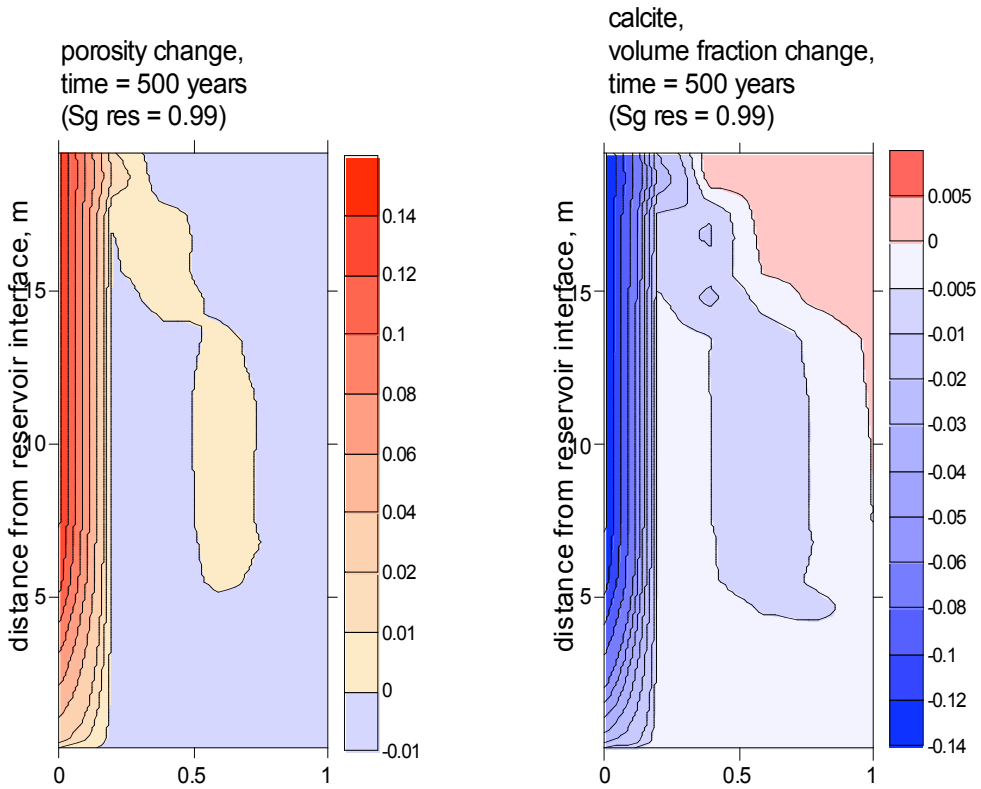


*Figure 79 – Contour plots showing porosity and calcite volume fraction change after 500 years simulation (initial reservoir gas saturation, Sg = 0.99)*

As in all the previous simulations, porosity and calcite variations inversely correlate all throughout the caprock domain (Figure 79), indicating that dissolution/precipitation mechanisms involving this mineral exert the dominant control on porosity enhancement/reduction. This is in agreement with the intrinsic fast kinetics of calcite.

A major difference with respect to previous simulations is represented by the large increase in porosity predicted for the fracture domain. This porosity enhancement reaches a maximum of about +0.14 (expressed as volume fraction normalized to total volume of porous medium), which means a maximum total porosity of about 0.64 in the fracture (the initial porosity was 0.50). Large variations also occur in the adjacent matrix columns, as shown by delta values of +0.10 and +0.06 at 0.05 and 0.1 m from the fracture axis, respectively.

This overall behavior reflects the fact that calcite dissolution due to $CO_2$-driven acidification is now very effective. This is because the steady increase in $Ca_{TOT}$ and $HCO_{3,TOT}$ concentrations, naturally induced by aqueous diffusion from the reservoir, has been significantly reduced in this simulation by lowering the initial liquid saturation in the reservoir, and increasing (with respect to the 1D models already discussed) initial porosity of the fracture domain.

The mineralogical transformations involving minerals other than calcite are quantitatively negligible also after 500 years of simulation (Figures 80 to 85). The most relevant changes correspond to muscovite dissolution (up to -0.02 porous medium volume fraction, at the top of the matrix, near fracture domain), and Na-smectite precipitation (up to +0.016 porous medium volume fraction, in the same part of matrix domain).

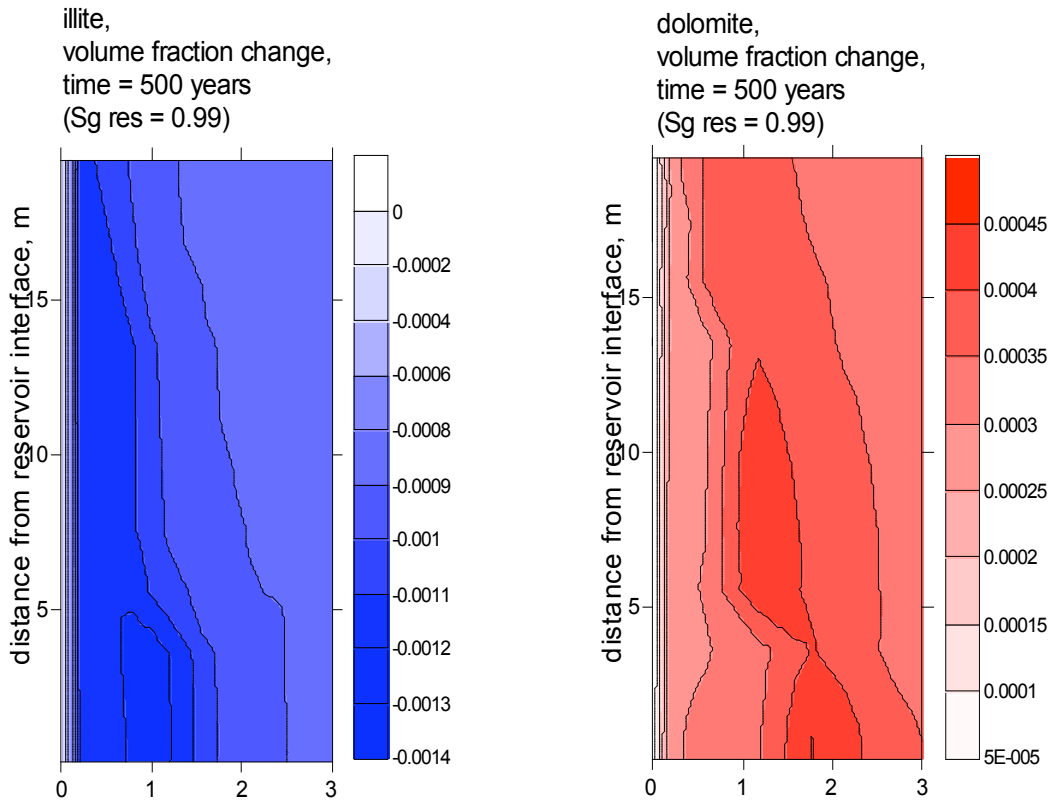


*Figure 80 – Contour plots showing illite and dolomite volume fraction change after 500 years simulation (initial reservoir gas saturation, Sg = 0.99)*

Overall trends (after 500 years simulation) for the remaining minerals are as follows:

1) chlorite and illite steadily dissolve, and the maximum decrease in volume fraction occurs along a vertical direction, in the matrix columns adjacent to fracture domain; maximum delta values are about -0.003 and -0.001 for chlorite and illite, respectively;

2) carbonate minerals like ankerite, dolomite and dawsonite tend to precipitate in the same zones where clay minerals like muscovite, chlorite and illite dissolve; dawsonite shows the maximum increase (about +0.015), followed by ankerite (up to about +0.003) and dolomite (up to about +0.0005);

3) kaolinite and quartz (not shown in the Figures) have the same complex pattern, characterized by precipitation in the zones where lowest pH conditions develop, i.e. near the fracture, and dissolution in the inner part of the matrix; delta values are very low and span the range +1.0e-4 to -5.0e-5, and +1.6e-6 to -1.0e-5 for kaolinite and quartz, respectively.

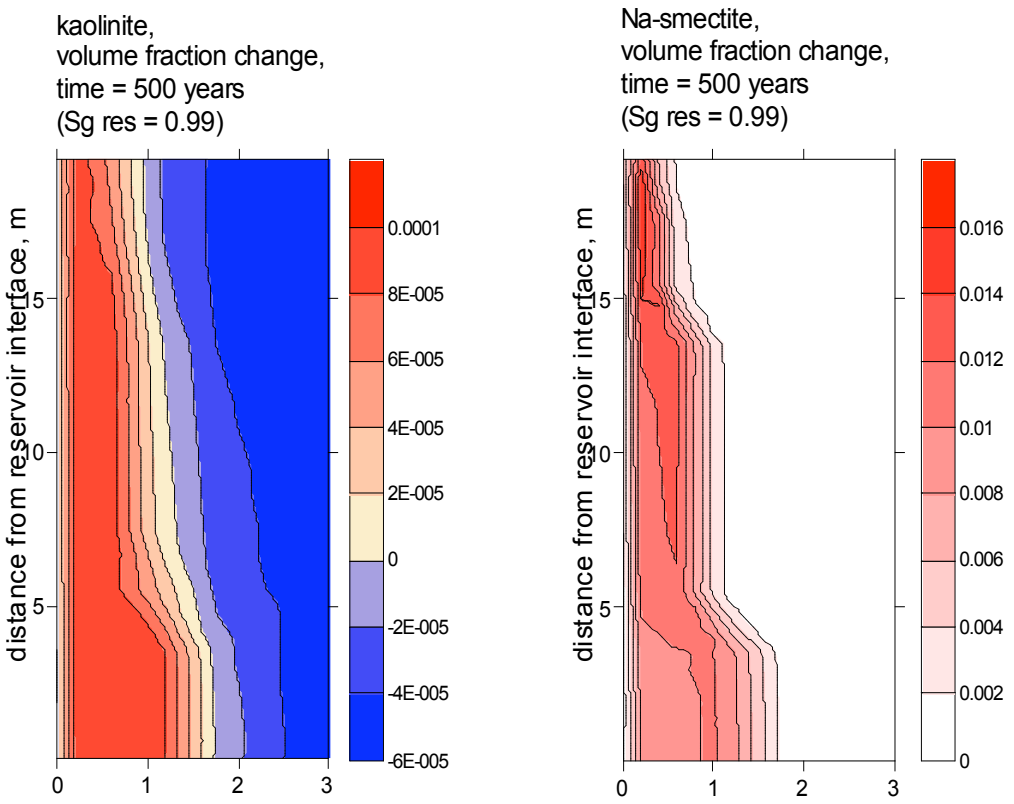


*Figure 81 – Contour plots showing kaolinite and Na-smectite volume fraction change after 500 years simulation (initial reservoir gas saturation, Sg = 0.99)*

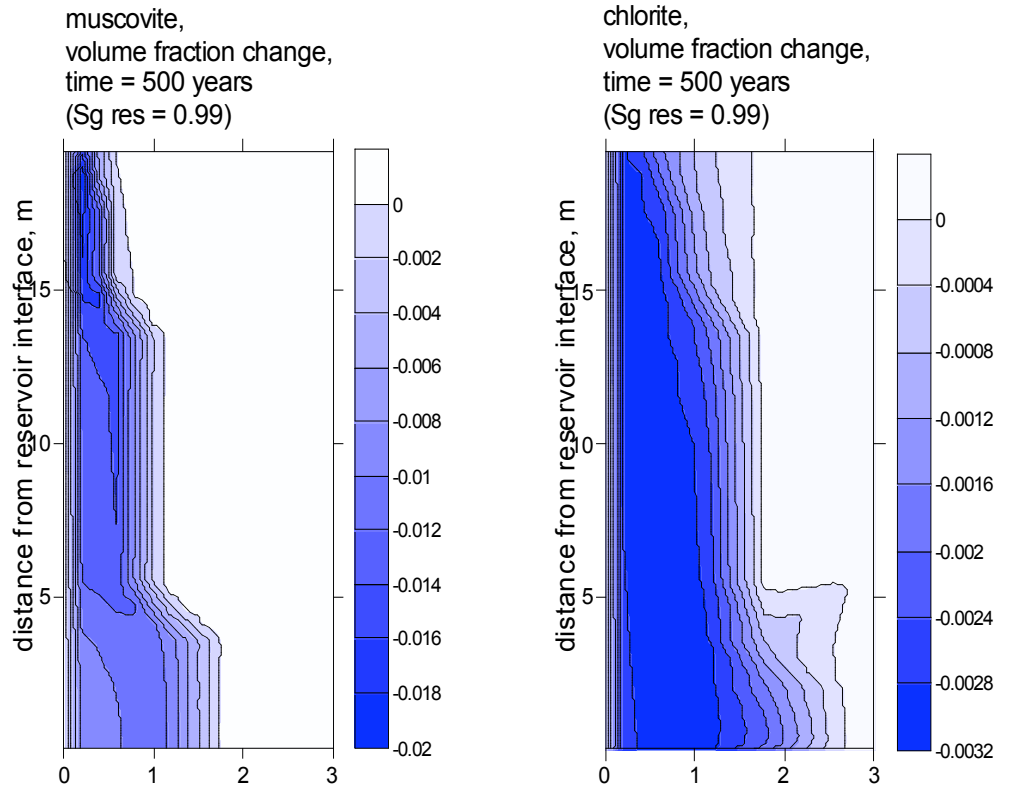


*Figure 82 – Contour plots showing muscovite and chlorite volume fraction change after 500 years simulation (initial reservoir gas saturation, Sg = 0.99)*

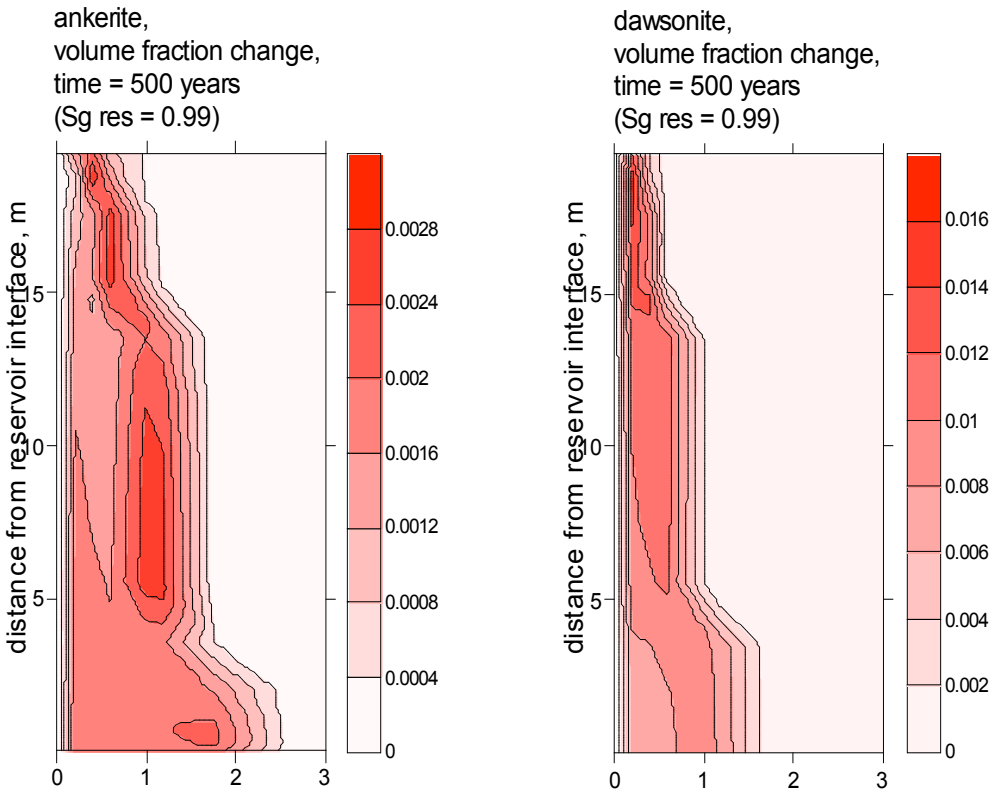


*Figure 83 – Contour plots showing ankerite and dawsonite volume fraction change after 500 years simulation (initial reservoir gas saturation, Sg = 0.99)*

Coupled with information on spatial distribution of aqueous components concentration, these data reveal that long term $CO_2$(g) advection through the fracture induces, other than a consistent lowering in pH, the following changes in the aqueous chemical composition of the caprock:

1) a large increase in $HCO_{3,TOT}$., due to gas dissolution;

2) an appreciable increase of $Fe_{TOT}$, $Mg_{TOT}$, $Al_{TOT}$ and $SiO_2(aq)_{TOT}$ components, due to Al-silicate dissolution (chlorite, illite and muscovite) and molecular diffusion induced by fluids migrating in the fracture;

3) a decrease of $Na_{TOT}$ concentration prevalently driven by molecular diffusion as a consequence of the fact that fluids in the fracture are Na-depleted with respect to fluids of the matrix domain.

The behavior of the fracture domain is critical for the evaluation of the sealing efficiency of the caprock. Inspection of Figure 86 reveals that significant changes in the mineralogical facies of the solid fraction have occurred after 500 years simulation.

Two major zones can be recognized at this time: the lower part of the column (up to about 5.55 m from reservoir interface) is characterized by the presence of variable concentrations of calcite (3.7 to 27.2% near the reservoir interface) and relatively lower porosities (between 50.8 to 62.8%); the upper part of the fracture domain (7 to 19.55 m from reservoir interface) is characterized by higher porosity (around 64.1%), lack of calcite, and higher concentrations of all other minerals.

Apart from massive calcite dissolution, major transformations in the upper part of the column involve Na-smectite (now representing 21.6 to 22.2% of the solid fraction), kaolinite (about 7.2%), dawsonite (less than 0.1%), siderite (less than 0.1%), dolomite (5.1%) and quartz (28.5 to 28.6%) precipitation, and muscovite (25.8 to 26.2%), chlorite (about 8.4%) and illite (about 2.8%) dissolution.

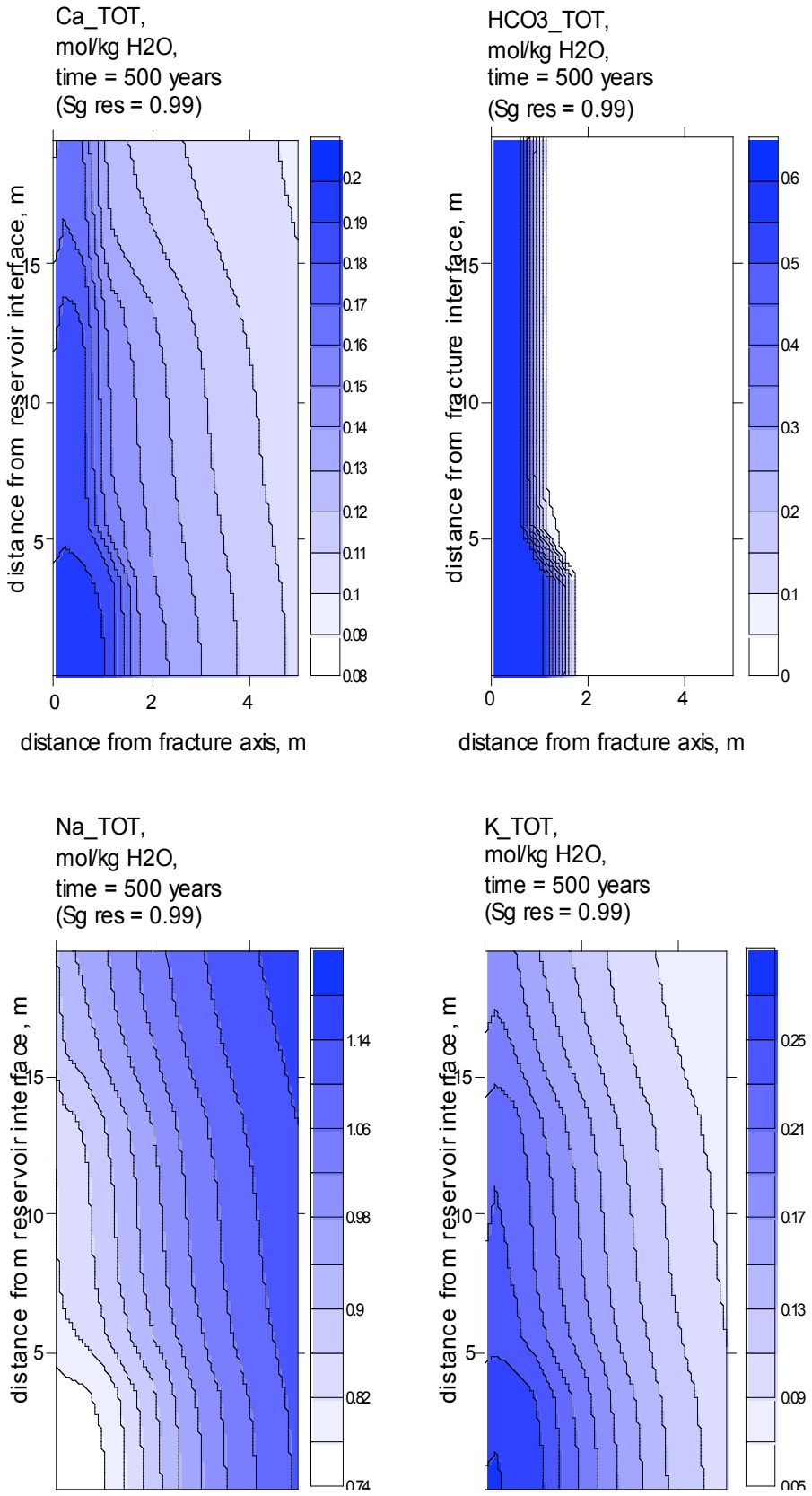


*Figure 84 – Contour plots showing $Ca_{TOT}$, $HCO_{3,TOT}$, $Na_{TOT}$ and $K_{TOT}$ spatial concentrations after 500 years simulation (initial reservoir gas saturation, Sg = 0.99)*

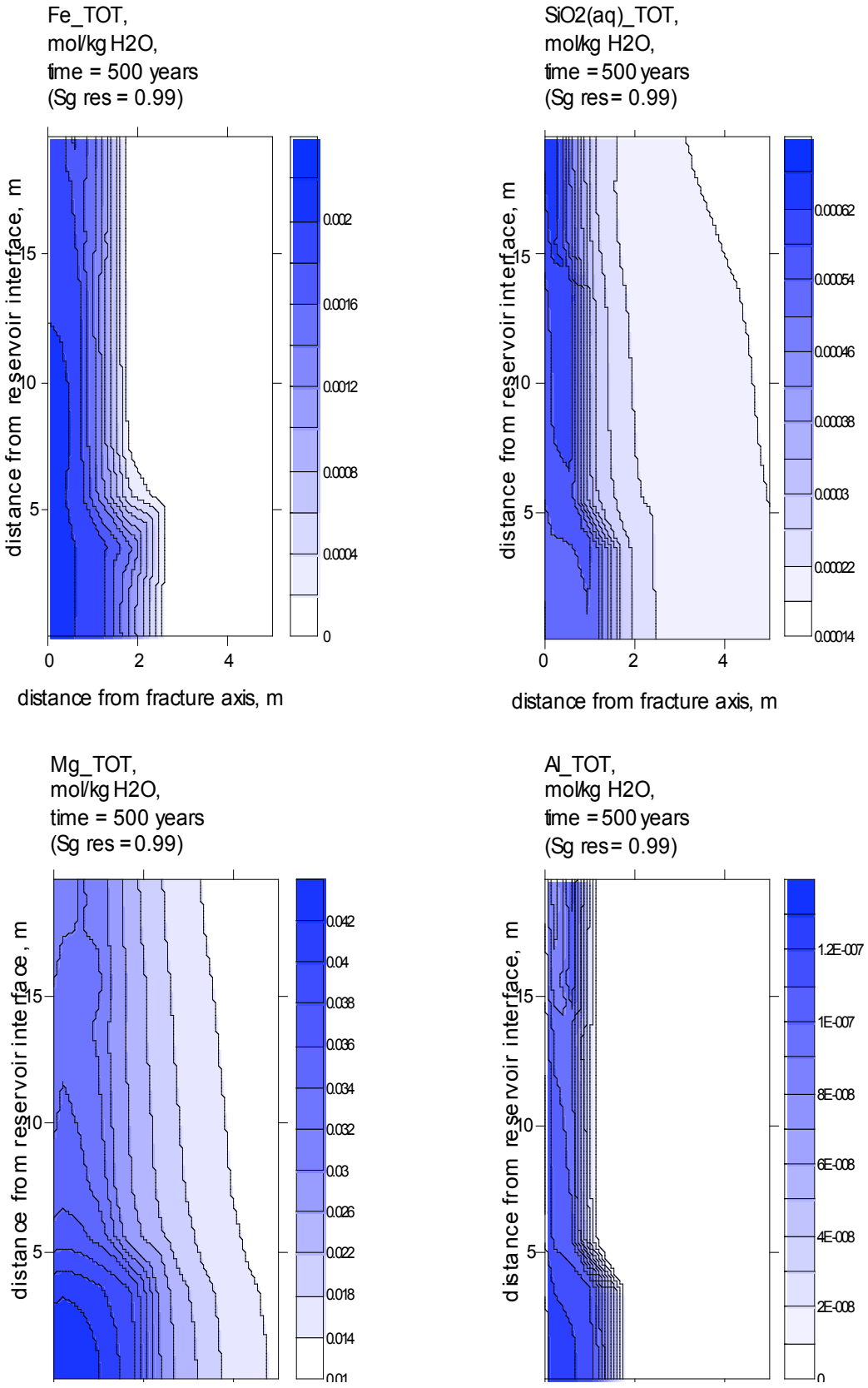


*Figure 85 – Contour plots showing $Fe_{TOT}$, $SiO_2(aq)_{TOT}$, $Mg_{TOT}$ and $Al_{TOT}$ spatial concentrations after 500 years simulation (initial reservoir gas saturation, Sg = 0.99)*

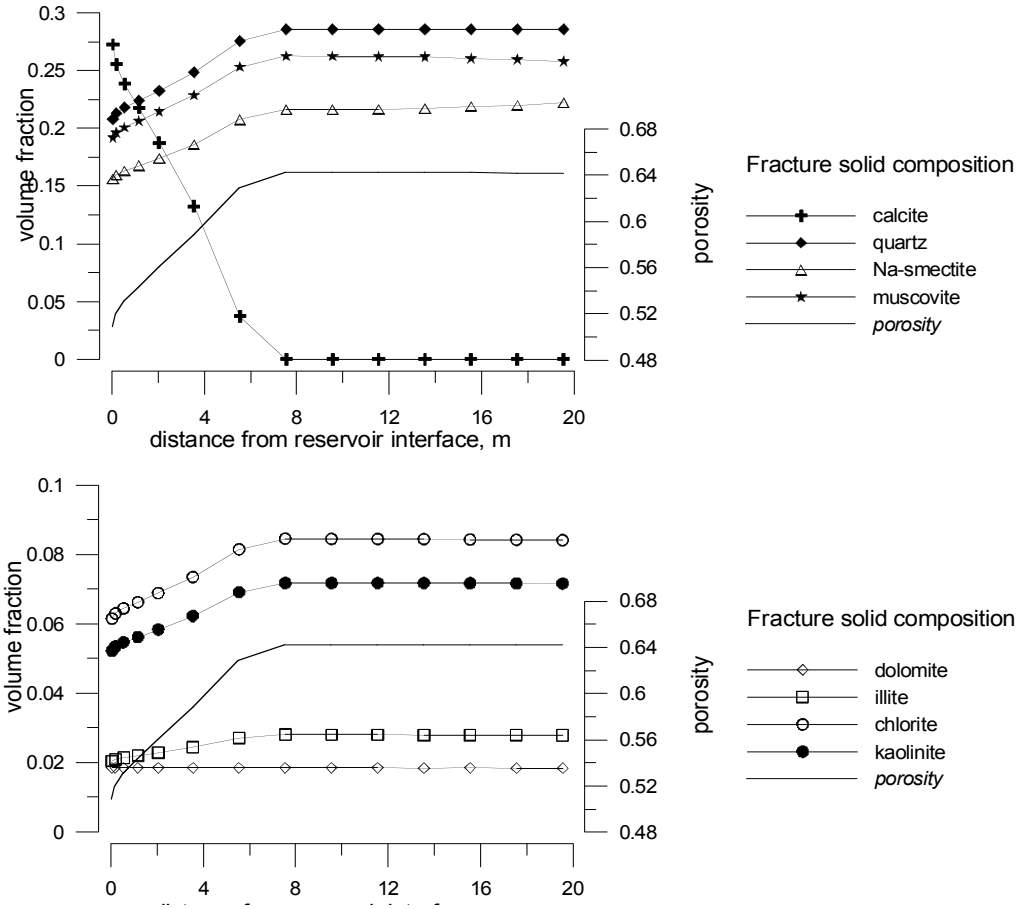


*Figure 86 – Mineralogical composition (expressed as solid volume fractions) of fracture domain after 500 years (initial reservoir gas saturation, Sg = 0.99)*

In Table 18 a summary of the average composition for the upper and lower part of the fracture is given, together with the initial reference value of the caprock.

*Table 18 – Average mineralogical composition (solid volume fraction) and porosity of upper and lower fracture domain compared with caprock initial values (data are after 500 years simulation).*

| | *porosity* | *cal* | *dol* | *qtz* | *ill* | *chl* | *kaol* | *Na-sme* | *musc* |
|---|---|---|---|---|---|---|---|---|---|
| *upper fracture* | 64.2% | 0.0% | 5.1% | 28.6% | 2.8% | 8.4% | 7.2% | 21.8% | 26.1% |
| *lower fracture* | 55.4% | 19.2% | 4.2% | 23.1% | 2.3% | 6.8% | 5.8% | 17.4% | 21.3% |
| *initial* | 50.0% | 28.5% | 3.7% | 20.5% | 2.0% | 6.2% | 5.1% | 15.1% | 19.0% |

*Abbreviations are as follows:*
*cal=calcite; dol=dolomite; qtz=quartz; ill=illite; chl=chlorite; kaol=kaolinite; Na-sme=Na-smectite; musc=muscovite*

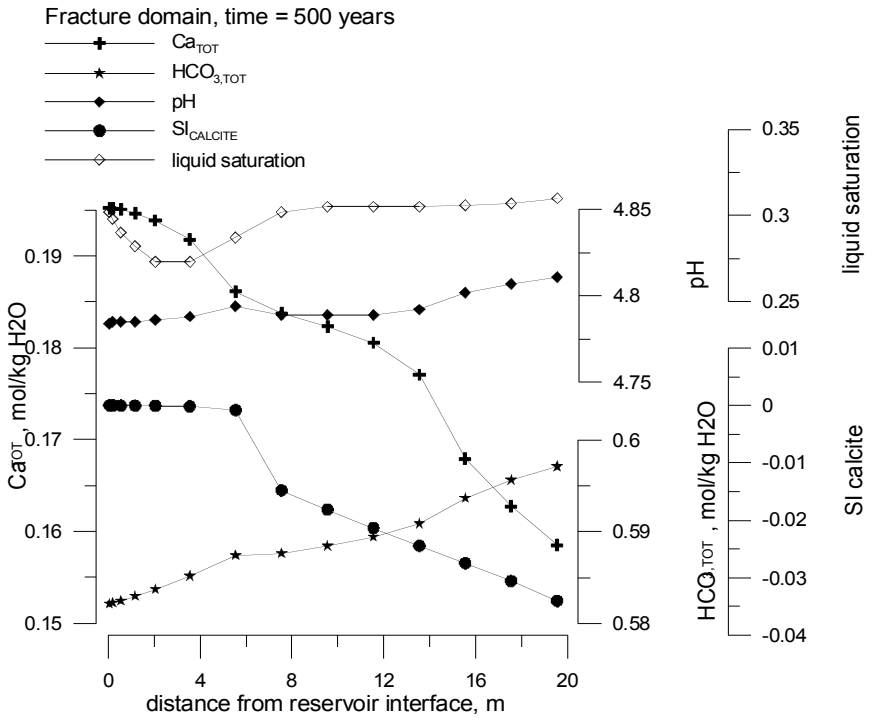


*Figure 87 – $Ca_{TOT}$, $HCO_{3,TOT}$, pH and calcite saturation index profiles along the fracture domain after 500 years (initial reservoir gas saturation, Sg = 0.99)*

Patterns shown in Figure 87 further confirm that liquid advection and aqueous molecular diffusion from the reservoir induce an increase in $Ca_{TOT}$ concentration and calcite saturation index within the fracture domain. This in turn, allows calcite to precipitate near the caprock-reservoir interface, when appropriate $HCO_{3,TOT}$ concentrations and pH values occur, as previously shown for 1D simulations. In this simulation, instead, $SI_{CALCITE}$ values appear stabilized around zero after 500 years simulation (SI = -0.00001), and almost no precipitation/dissolution occur at this time in the first element of the fracture (dissolution rate = 1.5e-11 mol/s). Far from the caprock-reservoir interface, $Ca_{TOT}$ concentration falls below some critical value allowing calcite to become undersaturated, and then to dissolve up to complete disappearance. pH variations are negligible and do not appreciably affect the equilibria in the carbonate subsystem. $HCO_{3,TOT}$ concentrations are higher and spatially more homogeneous than $Ca_{TOT}$ concentrations all along the fracture, suggesting that the spatial variations of $Ca_{TOT}$ concentration is the limiting factor governing the overall geochemical behavior of the domain. Water-rock interactions occur because non-zero liquid saturation values persist all throughout the fracture domain, in spite of the massive ingression of $CO_2$(g) from the reservoir.

When higher initial pressures are specified in the reservoir, fluids are allowed to flow faster through the fracture. As shown in Figure 88, all the patterns previously described are shifted along the fracture when an overpressure of 4, instead of 2 bar, is applied to reservoir. Under these conditions, chemical gradients between reservoir and caprock domains are smaller over a larger part of the fracture domain, as shown by the smoothed behavior of both $Ca_{TOT}$ and $HCO_{3,TOT}$ concentration profiles. Calcite is near saturation for the first 10 m of the fracture from reservoir interface, but in the upper part of the column the degree of undersaturation is larger than before (up to -0.042). This is due to the fact that pH is slightly more acid than before, in particular in the upper part of the fracture where values lower than 4.77 are now observed (instead of 4.8). Finally, the minimum value of liquid saturation (now equal to 0.21) is predicted at about 12 m from reservoir interface, instead of about 2 to 3 m ($S_L$ = 0.27).

The presence of a such “flow-controlled reactive regime” allows minerals kinetically and thermodynamically favored such as calcite and dolomite to precipitate more efficiently than before and, in the case of calcite, to start to dissolve at greater distances from reservoir interface. At the same time, the onset of chlorite, kaolinite

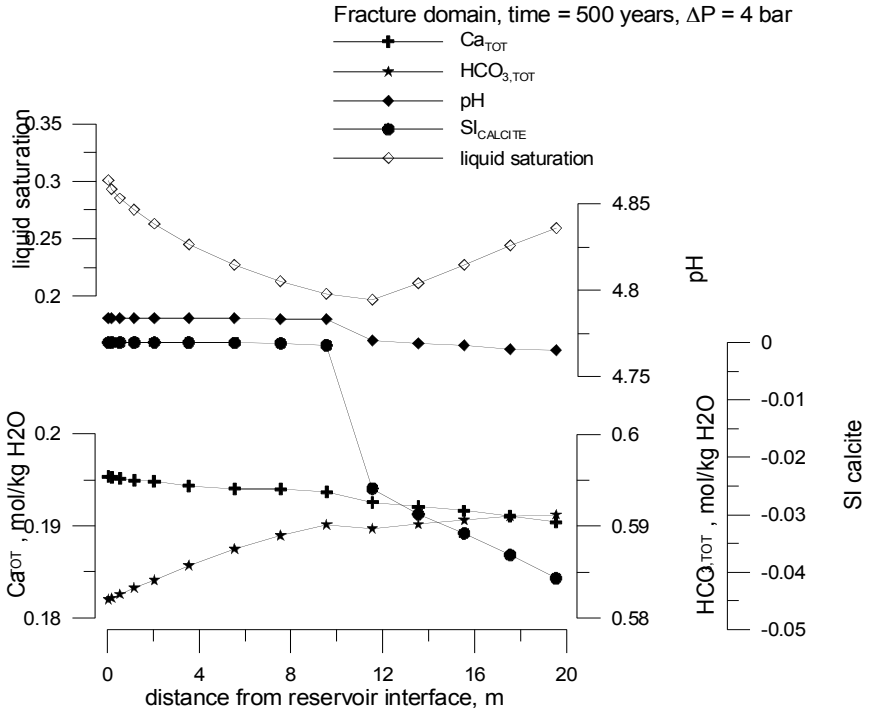


*Figure 88 – $Ca_{TOT}$, $HCO_{3,TOT}$, pH and calcite saturation index profiles along the fracture domain after 500 years (initial reservoir gas saturation, Sg = 0.99; reservoir overpressure = 4 bar)*

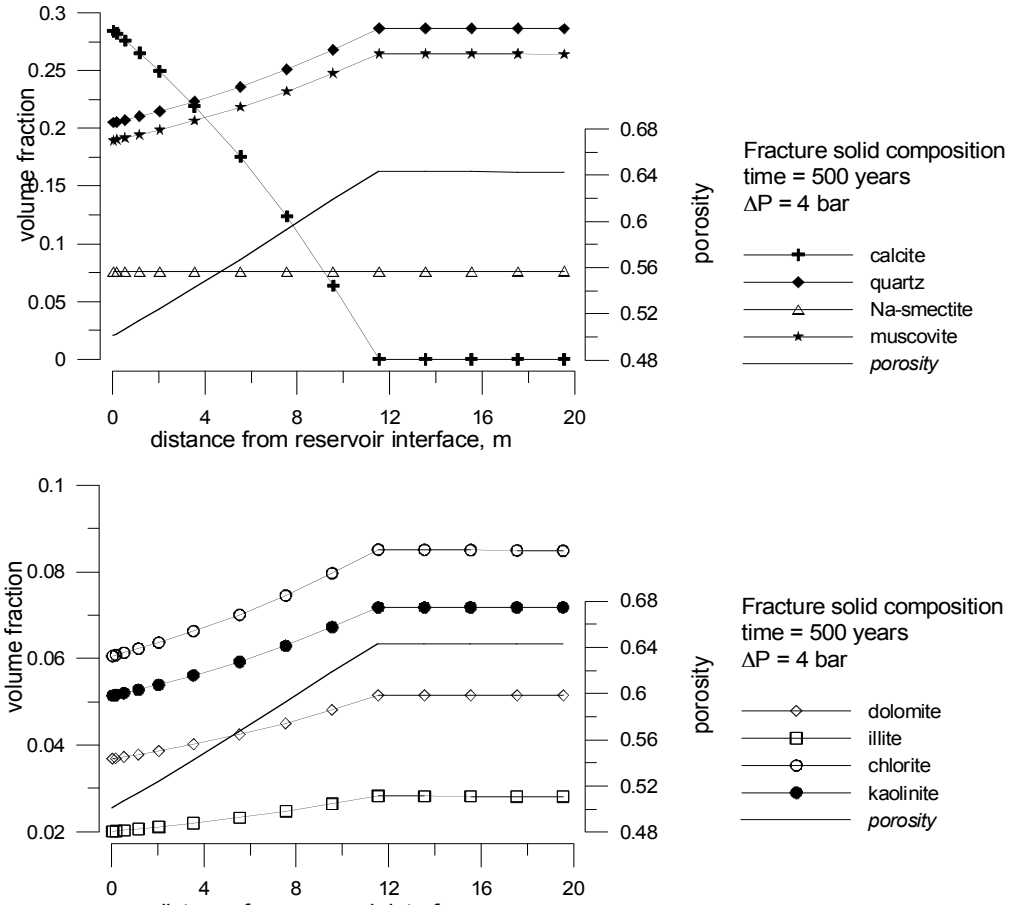


*Figure 89 – Mineralogical composition (expressed as solid volume fractions) of fracture domain after 500 years (initial reservoir gas saturation, Sg = 0.99; reservoir overpressure = 4 bar))*

and illite precipitation is retarded (now at about 12 m), whereas the volume fraction of Na-smectite does not increase appreciably, according to the intrinsically slow kinetics of all these minerals. Also the porosity profile is affected by the increased flow velocity: this effect is manifested in terms of spatial displacement of the maximum porosity value, which now occurs at about 12 m from reservoir interface, but not in terms of porosity enhancement, as the maximum porosity value remains near 0.64.

## 8. Conclusions

Models presented in this report are an idealization of the physical and chemical processes expected to occur in the caprock, as a consequence of $CO_2$ geological disposal in a depleted ENI gas field. Such models describe overall changes under specific assumed physical and chemical conditions which cannot be fully representative of the complexity of the system under study. Predictions of future scenarios cannot be considered “exact” at this stage, and their accuracy would be greatly improved by the availability of more detailed site-specific physical and chemical data.

Despite these limitations, numerical calculations shed light on general geochemical trends affecting mineralogy and sealing efficiency of the caprock in the presence of a $CO_2$-rich advancing fluid front.

Major conclusions are as follows.

1) Under the conditions investigated in this study, dissolution reactions may reduce the sealing efficiency of caprock formations when physical discontinuities occur, which would allow fluids to advect upwards into the

caprock. In contrast, molecular diffusion in the aqueous phase tends to induce reductions of porosity. In both cases, the overall geochemical behavior is controlled by dissolution/precipitation reactions involving calcite.

2) The overall geochemical behavior of the caprock domain is explained in terms of the following mechanisms. Liquid advection and aqueous molecular diffusion from the reservoir tend to increase $Ca_{TOT}$ and $HCO_{3,TOT}$ concentrations and calcite saturation index in the caprock. This induces calcite precipitation in the caprock when appropriate pH values occur, i.e., when the competing effect of pH lowering associated with the advancement of the $CO_2$-rich front is overwhelmed by increases in $Ca_{TOT}$ and $HCO_{3,TOT}$ concentrations. The main effect of gas advection is to increase $CO_2$ partial pressure $P_{CO2}$ and lower pH values, which will make calcite less thermodynamically stable in the caprock. The interplay between $[Ca^{+2}]$, $[HCO_3^-]$ and $[H^+]$ thus controls calcite dissolution/precipitation behavior in the caprock domain.

3) The presence of a $CO_2$-rich gas phase has a strong influence on hydrogeochemical evolution of the caprock. Under conditions of predominantly advective transport, such as expected for a fractured caprock (2D models), $CO_2$(g) penetrates through the caprock and induces some enhancement in porosity and permeability. When transport of chemicals primarily occurs by molecular diffusion in the liquid phase, as is expected for a sealed, unfractured caprock (1D models), $CO_2$-leakage becomes self-limiting, and pores become clogged after a very short time.

4) The dominant role played by calcite overwhelms the effects of other mineralogical changes involving precipitation/dissolution of Al-silicate minerals. Even if not significant in terms of overall mass transfer, other mineral transformations induced by the advancement of the $CO_2$-induced acidic front in the caprock include clay dissolution (illite, chlorite and muscovite) and precipitation reactions (Na-smectite). Other effects include the formation of new minerals such as dawsonite, siderite, and ankerite. These results are in agreement with recent theoretical findings (e.g. Palandri and Kharaka, 2005), which demonstrated that ferric iron in sediments may act as a trap for $CO_2$, provided that divalent metals such as Ca and/or Mg are present in the rock matrix.

## Acknowledgement

The authors appreciate reviews of the manuscript and the suggestion of improvements by Guoxiang Zhang (LBNL) and Giovanni Gianelli (IGG-CNR). This work was supported by the Director, Office of Science, Office of Basic Energy Sciences of the U.S. Department of Energy under Contract No. DE-AC02-05CH11231, and by the Consiglio Nazionale delle Ricerche, Italy, under the SnamProgetti SpA contract No. 3000005218, in the framework of the ENI SpA “GreenHouse Gases” R&D project. Support by Stogit, EniTecnologie and ENI E&P Division is warmly acknowledged.

## References

Bachu, S., W.D. Gunter and E.H. Perkins. Aquifer disposal of $CO_2$ . Hydrodynamic and mineral trapping, *Energy Convers. Manag.,* Vol. 35, pp. 269–279, 1994.

Gaus, I., M. Azaroual and I. Czernichowski-Lauriol. Reactive Transport Modelling of the Impact of $CO_2$ Injection on the Clayey Cap Rock at Sleipner (North Sea), *Chemical Geology,* Vol. 217, pp. 319–337, 2005.

Gunter, W.D., E.H. Perkins, and I. Hutcheon. Aquifer disposal of acid gases: modelling of water-rock reactions for trapping of acid wastes, *Applied Geochemistry,* Vol. 15, pp. 1085–1095, 2000.

Helgeson, H.C., D.H. Kirkham, and D.C. Flowers. Theoretical prediction of the thermodynamic behavior of aqueous electrolytes at high pressures and temperatures: IV Calculation of activity coefficients, osmotic coefficients, and apparent molal and standard and relative partial molal properties to 600 C and 5 kb, *American Journal of Science,* Vol. 281, pp. 1249–1516, 1981.

Hitchon, B. Aquifer disposal of Carbon Dioxide. Hydrodynamic and Mineral Trapping – Proof of concept. In Geoscience Publishing Ltd., Sherwood Park, Alberta, Canada, 1996.

Knauss, K.G., J.W. Johnson and C.I. Steefel. Evaluation of the impact of $CO_2$, co-contaminant gas, aqueous fluid and reservoir rock interactions on the geologic sequestration of $CO_2$, *Chemical Geology,* Vol. 217, pp. 339–350, 2005.

Lasaga, A.C.. Chemical kinetics of water-rock interactions, *Journal of Geophysical Research,* Vol. 89, pp. 4009–4025, 1984.

Millington, R.J. and J.P. Quirk. Permeability of Porous Solids, *Trans. Faraday Soc.,* Vol. 57, pp. 1200–1207, 1961.

Narasimhan, T.N. and P.A. Whiterspoon. An integrated Finite Difference Method for Analyzing Fluid Flow in Deformable Porous Media, *Water Resources Research,* Vol. 12, No. 1, pp. 57–64, 1976.

Palandri, J.L. and Y.K. Kharaka. A compilation of rate parameters of water-mineral interaction kinetics for application to geochemical modeling, *US Geological Survey Open File Report 2004-1068,* 64 pp., 2004.

Palandri, J.L. and Y.K. Kharaka. Ferric Iron-bearing Sediments as a Mineral Trap for $CO_2$ Sequestration: Iron Reduction Using Sulfur-bearing Waste Gas, *Chemical Geology,* Vol. 217, No. 3-4, pp. 351–364, 2005.

Pruess, K.. TOUGH2: A general-purpose numerical simulator for multiphase fluid and heat flow, Lawrence Berkeley National Laboratory Report LBL-29400, Berkeley, California, 1991.

Pruess, K., C. Oldenburg and G. Moridis. TOUGH2 User's guide, Version 2.0, Lawrence Berkeley National Laboratory Report LBNL-43134, Berkeley, California, 1999.

Raffensperger, J.P. Numerical simulation of sedimentary basin-scale hydrochemical processes, In Advances in Porous Media, Corapcioglu, Y.C., (ed), Amsterdam, The Netherlands, Elsevier Science, 440 pp., 1996.

Spycher, N. and M.H. Reed. Fugacity coefficients of $H_2$, $CO_2$, $CH_4$, $H_2O$ and of $H_2O$-$CO_2$-$CH_4$ mixtures: A virial equation treatment for moderate pressures and temperatures applicable to calculations of hydrothermal boiling, *Geochimica et Cosmochimica Acta,* Vol. 52, pp. 739–749, 1988.

Tanger, J.C. and H.C. Helgeson. Calculation of the thermodynamic and transport properties of aqueous species at high pressure and temperatures: Revised equations of state for the standard partial molal properties of ions and electrolytes, *American Journal of Science,* Vol. 288, pp. 19–98, 1988.

Van Genuchten, M.T. A closed-form equation for predicting the hydraulic conductivity of unsaturated soils, *Soil Sci. Soc. Am. J.*, Vol.44, pp. 892-898, 1980.

Weir, G.J., S.P. White, and W.M. Kissling. Reservoir storage and containment of greenhouse gases, *Transp. Porous Media,* Vol. 23, pp. 37–60, 1996a.

Weir, G.J., S.P. White, and W.M. Kissling. Reservoir storage and containment of greenhouse gases. II. Vapour-entry pressures, *Transp. Porous Media,* Vol. 23, pp. 61–82, 1996b.

White, S.P., R.G. Allis, J. Moore, T. Chidsey, C. Morgan, W. Gwynn and M. Adams. Simulation of reactive transport of injected $CO_2$ on the Colorado Plateau, Utah, USA, *Chemical Geology,* Vol. 217, pp. 387–405, 2005.

Wolery, T.J. EQ3/6: Software package for geochemical modeling of aqueous systems: Package overview and installation guide (version 8.0), Lawrence Livermore National Laboratory Report UCRL-MA-10662 PT I, Livermore, California, 1992.

Xu, T., E. Sonnenthal, N. Spycher and K. Pruess. TOUGHREACT User's Guide: A Simulation Program for Non-isothermal Multiphase Reactive Geochemical Transport in Variably Saturated Geologic Media, Lawrence Berkeley National Laboratory Report LBNL-55460, Berkeley, California, 2004a.

Xu, T., Y. Ontoy, P. Molling, N. Spycher, M. Parini and K. Pruess. Reactive Transport Modeling of Injection Well Scaling and Acidizing at Tiwi Field, Philippines, *Geothermics,* Vol. 33, No. 4, pp. 477 - 491, 2004b.

Xu, T., J.A. Apps and K. Pruess. Numerical simulation of $CO_2$ disposal by mineral trapping in deep aquifers, *Applied Geochemistry,* Vol. 19, pp. 917–936, 2004.

Xu, T., J.A. Apps and K. Pruess. Mineral Sequestration of Carbon Dioxide in a Sandstone-Shale System, *Chemical Geology,* Vol. 217, pp. 295–318, 2005. (LBNL-52566)

Xu, T., and K. Pruess. Coupled modeling of non-isothermal multiphase flow, solute transport and reactive chemistry in porous and fractured media: 1. Model development and validation, Lawrence Berkeley National Laboratory Report LBNL-42050, Berkeley, California, 1998.

Xu, T., and K. Pruess. Modeling multiphase flow and reactive geochemical in variably saturated fractured rocks: 1. Methodology, *American Journal of Science,* Vol. 301, pp. 16–33, 2001.

Yeh, G.T. and V.S. Tripathi. A model for simulating transport of reactive multispecies components: model development and demonstration, *Water Resources Research,* Vol. 27, pp. 3075–3094, 1991.